

***Nd:YAG Laser Welding of Ti-6Al-4V Alloy***

Abu Syed Humaun Kabir

A Thesis

In

The Department

of

Mechanical and Industrial Engineering

Presented in Partial Fulfilment of the Requirements

for the Degree of Master of Applied Science (Mechanical Engineering) at

Concordia University

Montreal, Quebec, Canada

January, 2011

© Abu Syed Humaun Kabir, 2011

**CONCORDIA UNIVERSITY**  
**SCHOOL OF GRADUATE STUDIES**

This is to certify that the Thesis prepared,

By: **Abu Syed Humaun Kabir**

Entitled: **“Nd:YAG laser Welding of Ti-6Al-4V Alloy”**

and submitted in partial fulfillment of the requirements for the Degree of  
**Master of Applied Science (Mechanical Engineering)**

complies with the regulations of this University and meets the accepted standards with respect to originality and quality.

Signed by the Final Examining Committee:

_____	Chair
Dr. A. Akgunduz	
_____	Examiner
Dr. R. Wuthrich	
_____	Examiner
Dr. R. Chromik	External
Materials Engineering, McGill University	
_____	Co-Supervisor
Dr. M. Medraj	
_____	Co-Supervisor
Dr. X. Cao	

Approved by:

\_\_\_\_\_  
Dr. A.K.W. Ahmed, MASc Program Director  
Department of Mechanical and Industrial Engineering

\_\_\_\_\_  
Dean Robin Drew  
Faculty of Engineering & Computer Science

Date: \_\_\_\_\_

# ABSTRACT

Nd:YAG Laser Welding of Ti-6Al-4V Alloy

Abu Syed Humaun Kabir

Butt joints of Ti-6Al-4V alloy sheets with two thicknesses (3.175 and 5.08 mm) are laser welded using a high power continuous wave Nd:YAG laser welding machine with or without the use of filler wires. Laser processing parameters investigated include laser power (2 – 4 kW), welding speed (0.75 – 7.5 m/min), joint gap (0 – 0.6 mm) and defocusing distance (-1 mm and -2 mm). Two post-weld heat treatments (i.e. stress relief annealing, solution treatment and aging) are investigated and compared with the as-welded condition. Although some welding defects such as underfill and porosity have been observed, high quality welds can be obtained using a high power Nd:YAG laser. Underfill defect is found to increase but the porosity area decreases with increasing welding speed. The use of the filler wire decreases the underfill defect. However, the porosity area increases with increasing joint gap. The hardness is maximum in the fusion zone (FZ) followed by a sharp decrease in the heat affected zone (HAZ) to the base metal (BM). The low temperature annealing process increases the hardness of the fusion zone but the combination of the high temperature solution treatment followed by aging decreases the fusion zone hardness almost to the base metal values. Tensile testing shows that the joint efficiency varies between 95 and 105 %. The porosity and underfill are the two main defects for failure in the FZ and HAZ, respectively. The local mechanical properties determined by digital image correlation (DIC) technique show that the elastic modulus and yield stress are maximum in the FZ and minimum in the HAZ. The lowest plastic strain at fracture is obtained in the FZ.

# ACKNOWLEDGEMENT

I take this opportunity to express my profound gratitude to my advisor, Professor Mamoun Medraj. His warm encouragement, suggestions, and feedbacks to what I got during the group and individual meetings have been the source of motivation during my whole period of study and research. I would like to express my appreciation and indebtedness to my co-supervisor, Dr. Xinjin Cao of National Research Council of Canada. It is through his constant and direct support and guidance, great enthusiasm and high standard of research that this work can finally be accomplished.

I am thankful to many student colleagues for providing an inspiring and pleasurable environment. I would also like to thank Dr. Javad Gholipour, Mr. Xavier Pelletier and Mr. Daniel Chiriac at AMTC-NRC and Mr. Robert Oliver at Concordia University for their support.

Most importantly, my deepest gratitude goes to my family especially to my wife Farhana, for helping me get through difficult times and all the emotional support and caring. She was always by my side throughout the whole time. Thanks to her very much. Thanks to my parents for bearing my absence for the years while I was in Canada.

Last but not least, thanks go to almighty God for giving me the patience and energy for this work. May your name be exalted, honoured, and glorified.

# TABLE OF CONTENTS

<b>LIST OF FIGURES</b> .....	viii
<b>LIST OF TABLES</b> .....	xi
<b>NOMENCLATURE</b> .....	xii
<b>Chapter 1</b> .....	1
1.1 Introduction .....	1
1.2 Objective .....	3
<b>Chapter 2/ Literature Review</b> .....	4
2.1 Titanium and Its Alloys .....	4
2.1.1 Classification of Ti-alloys .....	5
2.2 Ti-6Al-4V .....	6
2.2.1 Phase Transformation of Ti-6Al-4V .....	7
2.3 Laser .....	9
2.4 Laser Welding .....	10
2.4.1 Nd:YAG Laser .....	10
2.4.2 Laser Welding Mechanism .....	11
2.4.3 Laser Welding vs. Arc Welding .....	13
2.4.4 Laser Welding vs. Electron Beam Welding .....	13
2.4.5 CO <sub>2</sub> vs. Nd:YAG .....	14
2.5 Laser Weldability of Ti-6Al-4V .....	15
2.5.1 Microstructure .....	16
2.6 Laser Welding Parameters .....	16
2.6.1 Laser Power and Welding Speed .....	16
2.6.2 Focal Spot Size .....	17
2.6.3 Defocusing Distances .....	18
2.6.4 Shielding Gases .....	19
2.7 Joint Gap and Filler Materials .....	21
2.8 Welding Defects .....	22
2.8.1 Underfill .....	22
2.8.2 Porosity .....	23
2.8.3 Centerline Grain Boundary .....	26
2.8.4 Sag .....	26
2.8.5 Spatter .....	27
2.8.6 Solidification Cracking .....	27
2.9 Post-Weld Heat Treatment .....	27
2.10 Mechanical Properties .....	28
2.10.1 Hardness .....	28
2.10.2 Tensile Properties .....	29
2.10.3 Digital Image Correlation .....	30
<b>Chapter 3 / Experimental Procedures</b> .....	33

3.1 Material and Equipment .....	33
3.2 Key Experiments .....	35
3.3 Weld Geometry .....	36
<b>Chapter 4 / Effect of Laser Power and Welding Speed .....</b>	<b>38</b>
4.1 Weld Geometry .....	38
4.2 Microstructure .....	44
4.3 Defects .....	50
4.3.1 Underfill .....	50
4.3.2 Porosity .....	51
4.3.3 Overlap .....	53
4.3.4 Other Defects .....	54
4.4 Micro-Indentation Hardness .....	54
4.5 Global Tensile Properties .....	56
4.6 Local Tensile Properties .....	58
4.7 Fractography .....	66
4.8 Operating Window .....	66
<b>Chapter 5/ Effect of Welding Speed and Defocusing Distance .....</b>	<b>67</b>
5.1 Weld Geometry .....	67
5.2 Microstructures .....	71
5.3 Defects .....	72
5.3.1 Underfill .....	72
5.3.2 Porosity .....	74
5.4 Micro-Indentation Hardness .....	75
5.5 Global Tensile Properties .....	77
5.6 Local Tensile Property .....	83
5.7 Fractography .....	85
5.8 Operating Window .....	85
<b>Chapter 6/ Effect of Joint Gap .....</b>	<b>86</b>
6.1 Weld Geometry .....	86
6.2 Microstructure .....	89
6.3 Defects .....	91
6.3.1 Underfill .....	91
6.3.2 Porosity .....	92
6.4 Micro-Indentation Hardness .....	93
6.5 Global Tensile Properties .....	95
6.6. Local Tensile Properties .....	96
6.7 Fractography .....	101
<b>Chapter 7/ Effect of Post-Weld Heat Treatment .....</b>	<b>102</b>

7.1 Microstructure .....	103
7.2 Micro-Indentation Hardness .....	107
7.3 Global Tensile Properties .....	109
7.4 Local Tensile Properties .....	111
7.5 Fractography .....	118
<b>Chapter 8/ Summary and Concluding Remarks .....</b>	<b>120</b>
8.1 Effect of Laser Power and Welding Speed on the Weldability of 3.175 mm Sheets .....	120
8.2 Effect of Welding Speed and Defocusing Distance on the Weldability of 5.08 mm Sheets .....	121
8.3 Effect of Joint Gap on the Weldability of 3.175 and 5.08 mm Sheets.....	122
8.4 Effect of Post-Weld Heat Treatment on the Weldability of 3.175 and 5.08 mm Sheets .....	123
8.5 Recommendations for Future Work .....	124
<b>References .....</b>	<b>125</b>

# LIST OF FIGURES

## Literature Review

Figure 2.1	HCP and BCC structures of pure titanium	4
Figure 2.2	Pseudobinary phase diagram of titanium	5
Figure 2.3	Typical microstructures for Ti-6Al-4V at different cooling rates	8
Figure 2.4	Schematic of an Nd:YAG laser	11
Figure 2.5	Two different modes of welding (a) conduction (b) keyhole	12
Figure 2.6	Effect of welding speed and laser power on penetration depth for Ti-6Al-4V	17
Figure 2.7	Different defocusing positions in laser welding	19
Figure 2.8	Solubility curve for hydrogen in titanium as a function of temperature at one atmosphere external pressure	24
Figure 2.9	Schematic of a 3-D DIC system	31

## Experimental Procedures

Figure 3.1	Weld geometry of a typical butt joint	37
------------	---------------------------------------	----

### Effect of Laser Power and Welding Speed

Figure 4.1	Effect of heat input on transverse sections	40
Figure 4.2	Effect of laser power and welding speed on FZ and HAZ dimensions	42
Figure 4.3	Effect of laser power and welding speed on weld reinforcement dimensions	43
Figure 4.4	A typical base material microstructure of Ti-6Al-4V alloy in mill-annealed condition	45
Figure 4.5	Typical FZ microstructures at 3 kW and 1.69 m/min	46
Figure 4.6	Effect of laser power and welding speed on FZ microstructures	48
Figure 4.7	Microstructures of heat affected zone at 3 kW and 1.13 m/min	49
Figure 4.8	Effect of laser power and welding speed on underfill	51
Figure 4.9	Typical porosities observed in the welded joints	52
Figure 4.10	Effect of welding speed on porosity area and percentage of porosity	52
Figure 4.11	Some examples of overlap in welded joints at 4 kW laser power	53
Figure 4.12	Typical hardness distribution profile (3 kW and 1.69 m/min)	55
Figure 4.13	Effect of welding speed on average FZ hardness for 3 laser powers	56
Figure 4.14	Effect of welding speed on global tensile properties at 2 kW and 3 kW laser powers	57
Figure 4.15	Digital images of the last moment just before failure	60
Figure 4.16	Variation of elastic modulus and yield stress of Ti-6Al-4V alloy with quenching temperature	61
Figure 4.17	Local tensile properties for sample T 117 (2 kW, 1.13 m/min) and	62

	T 114 (3 kW, 1.13 m/min)	
Figure 4.18	True thicknesses of the sample ( 3 kW, 1.13 m/min) at different positions	63
Figure 4.19	Determination of local properties of HAZ	64
Figure 4.20	Local tensile properties for 2.0 kW and 3.0 kW laser powers	65
Figure 4.21	SEM fracture surface of the samples (a) 2 kW, 1.13 m/min, (b) 3 kW, 1.13 m/min	66
Figure 4.22	Operating window for the laser welding of 3.175 mm Ti-6Al-4V alloy	66

### **Effect of Welding Speed and Defocusing Distance**

Figure 5.1	Effect of welding speed and defocusing distance on transverse sections	68
Figure 5.2	Effect of welding speed and defocusing distance on FZ and HAZ dimensions.	69
Figure 5.3	Effect of welding speed and defocusing distance on weld reinforcement	70
Figure 5.4	Typical microstructures of (a) BM (b) FZ (c) Middle HAZ	72
Figure 5.5	Effect of welding speed and defocusing distances on underfill	73
Figure 5.6	Some examples of typical porosities	74
Figure 5.7	Effect of welding speed on porosity area and percentage of porosity at 2 defocusing distances	75
Figure 5.8	A typical hardness distribution profile (4 kW, 1.5 m/min, -1 mm)	76
Figure 5.9	Effect of welding speed on FZ average hardness	77
Figure 5.10	Effect of welding speed on global tensile properties for 2 defocusing distances	78
Figure 5.11	Digital images of the last moment just before failure	80
Figure 5.12	Comparison of the digital image and transverse section of the sample welded at 0.75 m/min, Defocusing = -1 mm	81
Figure 5.13	Local tensile properties of Defocusing = -1 mm, 1.0 m/min and Defocusing = -2 mm, 1.0 m/min	82
Figure 5.14	Local tensile properties for Defocusing = -1 mm and Defocusing = -2 mm	84
Figure 5.15	SEM fracture surfaces (a) Defocusing -1 mm, 1.0 m/min (b) Defocusing -2 mm, 0.75 m/min	85
Figure 5.16	Operating window for the 5.08 mm thickness	85

### **Effect of Joint Gap**

Figure 6.1	Effect of joint gap on transverse sections for both thicknesses	87
Figure 6.2	Effect of joint gap on FZ and HAZ dimensions for the both thicknesses	88
Figure 6.3	Effect of joint gap on weld reinforcements	89
Figure 6.4	Typical microstructures for the base metal of joint gap 0.4 mm (a) 3.175 mm and (b) 5.08 mm	90

Figure 6.5	Typical microstructures for the fusion zone of joint gap 0.4 mm (a) 3.175 mm and (b) 5.08 mm	90
Figure 6.6	Typical microstructures for the heat affected zone of joint gap 0.4 mm (a) 3.175 mm and (b) 5.08 mm	90
Figure 6.7	Effect of joint gap on underfill defect	91
Figure 6.8	Examples of porosity present in joints with various joint gaps for both thicknesses	92
Figure 6.9	Effect of joint gap on porosity area and area percentage	93
Figure 6.10	Typical micro-indentation hardness profile at 0.4 mm joint gap welded at 3 kW laser power and at a welding speed of 1.69 m/min	94
Figure 6.11	Effect of joint gap on FZ average hardness	94
Figure 6.12	Effect of joint gap on global tensile properties	95
Figure 6.13	Digital images of the last moment just before failure	98
Figure 6.14	Local tensile properties of 3.175 mm thickness (0.4 mm joint gap) and 5.08 mm thickness, (0.4 mm joint gap)	99
Figure 6.15	Local tensile properties of 3.175 mm and 5.08 mm thick samples	100
Figure 6.16	SEM fracture surface of (a) 3.175 mm, 0.3-mm joint gap (b) 5.08 mm, 0.2 mm joint gap	101

### **Effect of Post-Weld Heat Treatment**

Figure 7.1	Transverse sections in three different post-weld conditions	103
Figure 7.2	BM microstructure at as-welded, annealing and STA conditions for the two thicknesses	104
Figure 7.3	FZ microstructure at as-welded, annealing and STA conditions for the two thicknesses	105
Figure 7.4	Middle HAZ microstructures in as-welded, annealing and STA conditions for the two thicknesses	106
Figure 7.5	Three different hardness distributions for three post-weld conditions for the two thicknesses	108
Figure 7.6	Average hardness of three different zones in three post-weld conditions for (a) 3.175 mm and (b) 5.08 mm thick samples	109
Figure 7.7	Global tensile properties for three PWHT conditions of the two thicknesses	111
Figure 7.8	Digital images of the last stages before fracture of different PWHT for two thicknesses	112
Figure 7.9	Local elastic modulus of 3 PWHT conditions for the two thicknesses	114
Figure 7.10	Local yield stress of 3 PWHT conditions for the two thicknesses	115
Figure 7.11	Localized plastic strain at fracture of 3 PWHT conditions for the two thicknesses	116
Figure 7.12	Local tensile properties for the two thicknesses	117
Figure 7.13	SEM fracture surfaces of the two thicknesses	119

# LIST OF TABLES

## Literature Review

Table 2.1	Comparison of three different welding methods for Ti-6Al-4V	14
-----------	---	----

### Effect of Laser Power and Welding Speed

Table 4.1	Key experiments / effect of laser power and welding speed	38
-----------	---	----

### Effect of Welding Speed and Defocusing Distance

Table 5.1	Key experiments / effect of welding speed and defocusing distance	67
-----------	---	----

Table 5.2	Failure locations and joint efficiencies of all the samples of this part of study	79
-----------	---	----

### Effect of Joint Gap

Table 6.1	Key experiment / effect of joint gap	86
-----------	--------------------------------------	----

Table 6.2	Failure locations of all the samples of this part of study	96
-----------	--	----

### Effect of Post-Weld Heat Treatment

Table 7.1	Key experiments / effect of post-weld heat treatment	102
-----------	--	-----

Table 7.2	Failure locations and average joint efficiency of all the samples of this part of study	110
-----------	---	-----

## NOMENCLATURE

BM	Base Metal	HAZ	Heat Affected Zone
FZ	Fusion Zone	$M_f$	Final Temperature for Martensite Transformation
LBW	Laser Beam Welding	EBW	Electron Beam Welding
TIG	Tungsten Inert Gas	PWHT	Post Weld Heat Treatment
STAed	Solution Treated + Aged	$P_v$	Vaporization Pressure (Pa)
$P_I$	Radiation Pressure (Pa)	$P_\alpha$	Surface Tension (N/m)
$P_g$	Hydrostatic Pressure (Pa)	$P_h$	Hydrodynamic Pressure (Pa)
d	Focal spot Diameter (mm)	$\theta$	Beam Convergence Angle (radians)
F	Focal Length (mm)	eV	Electron Volt
S	Solubility of Hydrogen in Liquid Titanium (mL/100 g)	$T_L$	Liquidus Temperature (K)
$P_{H_2}$	Equilibrium Pressure of Hydrogen Above the Surface of Liquid Titanium (mm Hg).	DIC	Digital Image Correlation
LOP	Lack of Penetration	NR	Narrow Root
LP	Laser Power (kW)	HI	Heat Input (J/mm)
AWS	American Welding Society	HV 500 gf	Vickers Hardness Measured Using 500 g Force and 15 sec Dwell Time
SEM	Scanning Electron Microscope	Porosity %	Porosity Area Percentage to Fusion Zone Area
E	Elastic Modulus (GPa)	YS	Yield Stress (MPa)
UTS	Ultimate Tensile Stress (MPa)	% El	Percentage of Elongation

# Chapter 1

---

## 1.1 Introduction

Titanium was simultaneously discovered in England and Germany in 1790 [1]. As the ninth most plentiful element and the fourth most abundant structural metal in the earth crust exceeded only by aluminum, iron and magnesium, titanium started to be used commercially as structural material only in the 1950's [1, 2]. However, the high strength to weight ratio [3] and outstanding corrosion resistance [3, 4] of titanium and its alloys have led to a wide and diverse range of successful applications which demand high levels of reliable performance in aerospace [3, 4], automotive [3], chemical plant [4], power generation [3], oil and gas extraction, sports [5] as well as surgery and medicine [3].

Ti alloys have tensile strength equivalent to that of most of the alloy steels but the density of titanium is 56% of steel's and its corrosion resistance is much superior to steel and is comparable with platinum [1, 2, 6]. Titanium has better chemical compatibility with composite materials than aluminum which is very susceptible to galvanic corrosion with carbon fibre composites [2]. Another major advantage of Ti alloys is their higher operating temperatures than most of the steels, aluminum and even some nickel base alloys [7].

Although pure titanium is used in industries but its alloys, which exceed the non-alloyed titanium by mechanical and high-temperature strength, are used in larger amount. The temperature range for the applications of titanium alloys is from the deep-freezing temperatures (cryogenic alloys) up to 500–600°C (high-temperature alloys) [8].

Another advantage of titanium is that it is a polymorphic metal similar to iron and has a phase transformation at 882°C. Below this temperature, the hexagonal close-packed lattice ( $\alpha$ -Ti) is stable. Above 882°C, Ti has the body-centered cubic lattice ( $\beta$ -Ti). This transformation is very important since it offers the prospect of the alloys with  $\alpha$ ,  $\beta$ , or mixed  $\alpha/\beta$  microstructures and hence titanium alloys can have a wide range of properties [8, 9].

The increased application of titanium alloys needs a proper joining technology. In fusion welding processes, titanium shows some excellent characteristics such as good fluidity of the molten metal, low thermal conductivity, low density and high surface tension [10]. However, titanium alloys are difficult to weld because titanium is very reactive with atmospheric gases at higher temperature, especially in liquid state [11]. Porosity is usually generated during the welding, which reduces the mechanical properties of the welds. High heat input increases the grain size in the fusion zone and thus significantly reduces the ductility [11, 12].

A number of welding processes have been applied to weld Ti alloys such as arc, friction stir, and electron beam welding, but laser welding is the most promising since it provides high energy density, high welding speed, low heat input, narrow heat affected zone [3], high productivity, high weld quality, low distortion, high aspect ratio (weld penetration/bead width), manufacturing flexibility, fine grain size [12], and ease of automation [4]. Laser beam provides the line heating source through the thickness rather than the point heating source in conventional welding processes [13]. In addition, laser welding has the ability to weld with or without the use of a filler wire [6] and does not need the vacuum chamber like electron beam welding [14]. To date, the laser welding of

Ti-6Al-4V alloy has mainly concentrated on using CO<sub>2</sub> and lower power Nd:YAG lasers. However, very little literature is available on the weldability of Ti-6Al-4V alloy using high power Nd:YAG or fiber lasers.

## **1.2 Objective**

The aim of this project is to investigate the Nd:YAG laser weldability of Ti-6Al-4V alloy with and without the use of a filler wire. The Nd:YAG laser weldability of Ti-6Al-4V alloy will be studied by analyzing the effect of laser welding parameters on the weld geometry, microstructure, defects and mechanical properties.

# Chapter 2/ Literature Review

---

## 2.1 Titanium and Its Alloys

The crystal structure of pure titanium at room temperature is hexagonal close packed (HCP). This phase is designated as “ $\alpha$ ”. Figure 2.1 illustrates the  $\alpha$  unit cell. The sides of the hexagonal base,  $a$ , measure 2.95 Å, while the height,  $c$ , is 4.68 Å. The crystalline structure of Ti is dependent on temperature. 882°C is called the  $\beta$ -transus temperature for commercially pure titanium because the phase transformation appears at this temperature. The BCC structure has lattice constants  $a = b = c = 3.32$  Å and the  $\beta$ -unit cell is illustrated in Figure 2.1 [1, 2, 15, 16].

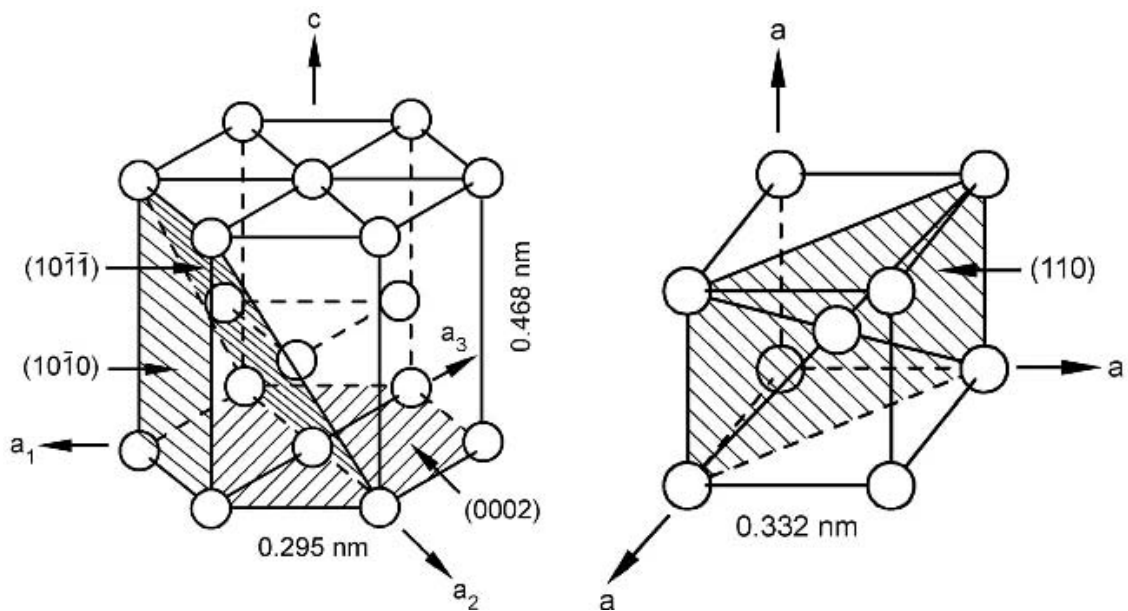


Figure 2.1- HCP and BCC structures of pure titanium [1].

### 2.1.1 Classification of Ti-alloys

Titanium alloys are classified into three major groups according to the corresponding weight percentages of the alloying elements [1, 15, 16]. The selection of alloying elements for titanium depends on the desired properties in the final alloy. Figure 2.2 shows the pseudobinary phase diagram of titanium with the position of Ti-6Al-4V.  $M_S$  is the martensite formation starting temperature.

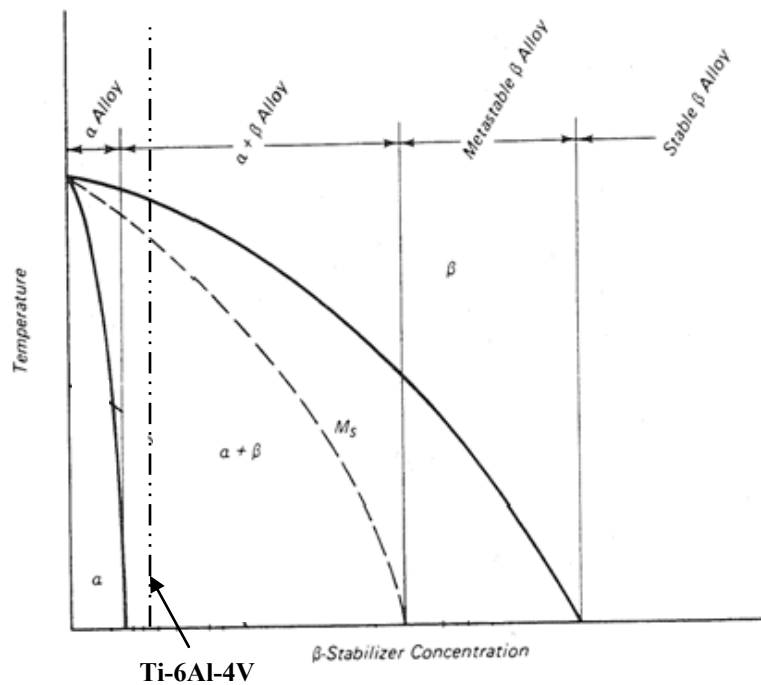


Figure 2.2- Pseudobinary phase diagram of titanium [15]

#### *$\alpha$ Alloys and Near $\alpha$ Alloys*

The alloys with a high volume fraction of  $\alpha$ -phase are termed  $\alpha$ -alloys, such as the binary Ti-Al or the ternary Ti-5Al-2Sn. An  $\alpha$ -alloy exhibits a microstructure consisting of nearly 100%  $\alpha$ -titanium. The elements C, O, N, Al, Ga, and Ge, are commonly used as  $\alpha$ -stabilizer. Al is the most common  $\alpha$ -stabilizer used so far but the amount is limited to 6% because more Al causes the precipitation of brittle intermetallic compound  $Ti_3Al$  [2]. The

$\alpha$ -alloys are mainly used in the chemical and process engineering industry because of their excellent corrosion resistance and deformability [2].

### *$\beta$ -Alloys and Metastable $\beta$ -Alloys*

The  $\beta$ -phase is stable at room temperature with appropriate alloying elements called  $\beta$ -stabilizers which lower the  $\beta$ -transus temperature such as Nb, Ta, Mo, V, and Cr [15, 16]. Alloys that have a high volume fraction of  $\beta$ -phase are  $\beta$  alloys. Examples of  $\beta$ -alloys are the binary alloys Ti-Mo and Ti-Nb, or the quaternaries Ti-13V-11Cr-3Al and Ti-11.5Mo-6Zr-4.5Sn. The elements V, Mo, and Nb are commonly chosen as  $\beta$ -stabilizers because they lower the  $\beta$ -transus temperature and do not readily promote the formation of metastable phases in titanium alloys [15].

### *$\alpha + \beta$ Alloys*

Alloys that have a balanced composition of both  $\alpha$  and  $\beta$ -phases are called  $\alpha + \beta$  alloys. The addition of  $\alpha$ -stabilizing elements in combination with  $\beta$ -stabilizers produce a shared volume fraction of both phases at room temperature and give the widest section in the phase diagram [2, 15]. The Ti-6Al-4V used in this work is a typical  $\alpha + \beta$  alloy and thus will be discussed in the following sections.

## **2.2 Ti-6Al-4V**

Ti-6Al-4V is an  $\alpha + \beta$  alloy that contains 6 wt% Al, and 4 wt% V. Aluminum stabilizes the HCP  $\alpha$ -phase while vanadium stabilizes the BCC  $\beta$ -phase at lower temperatures, and therefore Ti-6Al-4V exhibits a balance of both phases at room temperature [15]. Ti-6Al-4V is one of the very first titanium alloys developed and is by far the most popular

titanium alloys. Now, more than 50% of all titanium alloys used are of this composition [2]. Aerospace industry is the biggest consumer (more than 80 %) of Ti-6Al-4V [17]. It has an excellent combination of strength and toughness along with excellent corrosion resistance. Ti-6Al-4V can be used in applications where the working temperature is less than 300°C [1, 18].

### **2.2.1 Phase Transformation of Ti-6Al-4V**

The equilibrium microstructure of this alloy at room temperature consists mainly of the  $\alpha$ -phase with some retained  $\beta$ -phase. The  $\beta$ -transus defines the temperature above which the equilibrium microstructure will consist only of  $\beta$ -phase and is approximately 995°C for Ti-6Al-4V [1, 2, 15]. Different phase morphologies can form, depending on the temperature history of the alloy. Figure 2.3 shows different microstructures that can be formed in this alloy, depending on the cooling rate.

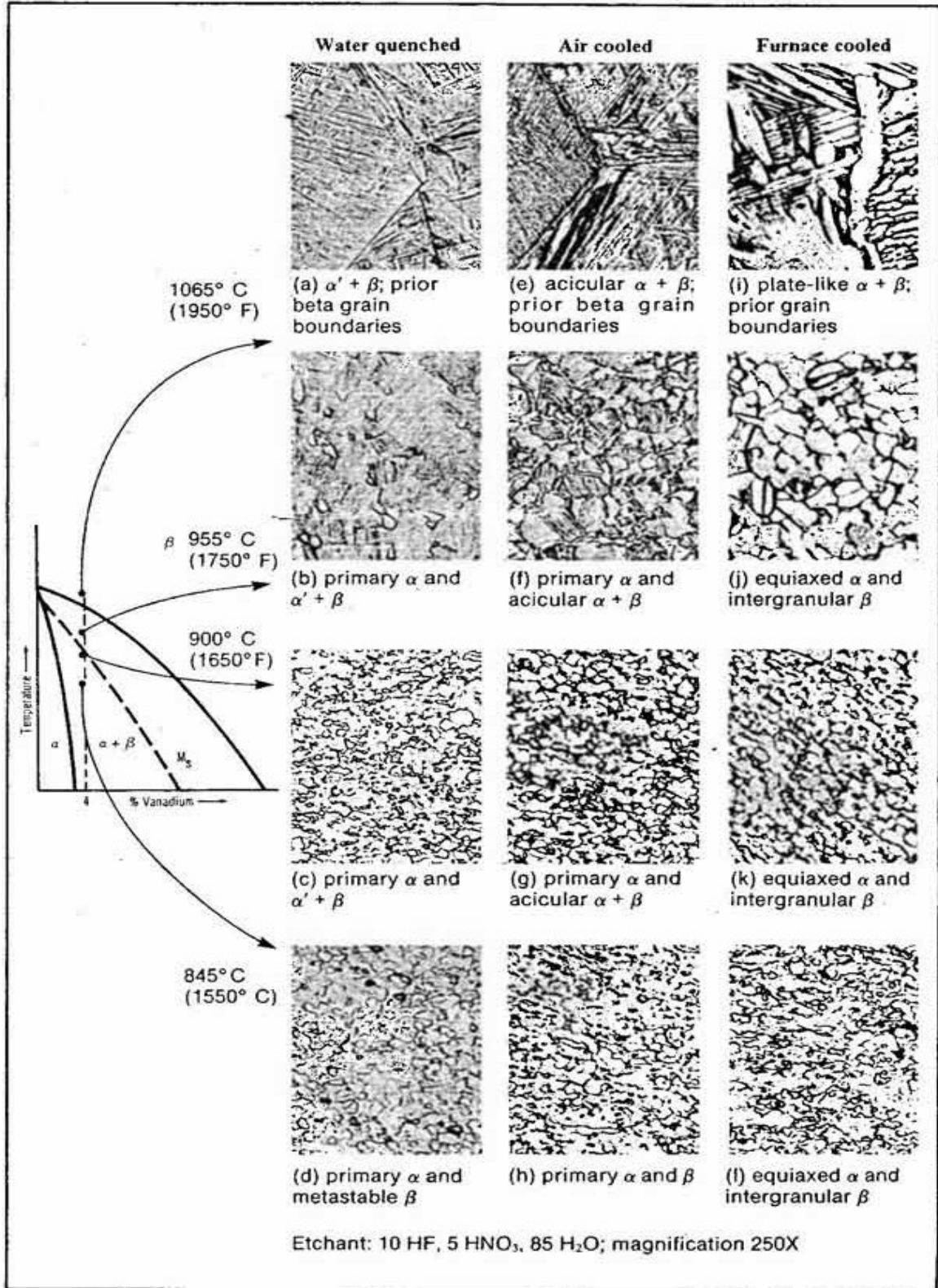


Figure 2.3: Typical microstructures for Ti-6Al-4V at different cooling rates [15]

At very slow cooling rate cooled from above the  $\beta$ -transus temperature, the  $\beta$ -phase mainly transforms into a globular  $\alpha$ -phase. Increasing the cooling rate enhances the  $\alpha$  nucleation rate in the  $\beta$  grain boundaries. The length and width of these  $\alpha$  platelets depend on the cooling rate. An increase in cooling rate increases the nucleation rate but decreases the growth rate, reducing the length and width of the platelets. If quenched, the  $\beta$  grain will fully or partially transform into a martensitic  $\alpha$ , denoted as  $\alpha'$  [19]. Ahmed and Rack [20] reported that the minimum cooling rate necessary for full martensite structure is 410°C/s for Ti-6Al-4V. A trace amount of  $\beta$  is always present in the martensite. The reason for the presence of  $\beta$ -phase is vanadium as a  $\beta$  stabilizer and 4% V is sufficient enough to drop the temperature for the end of martensitic transformation ( $M_f$ ) below room temperature [15, 21].

## 2.3 Laser

The word *laser* stands for "Light Amplification by Stimulated Emission of Radiation" [22]. Similar to the flashlight, the laser also converts electric energy to the light but the laser beam is narrower than a flashlight beam and the laser beam contains only one pure color instead of many different colors in flashlight beam. Unlike the waves from a flashlight, light waves in a laser beam are aligned with each other [23]. Laser transports very low (~mW) to exceptionally high (1–100 kW) focused power with a very small spot size and can be focused onto any kind of substrate through any medium [24].

## **2.4 Laser Welding**

Laser welding is a process that melts and joins materials by heating them with a laser beam. Out of all the welding techniques which exist today, laser welding is one of the most promising material joining methods because it provides high productivity [6], high weld quality [4], high welding speed, high weld aspect ratio, low heat input [6], low distortion [6], manufacturing flexibility [6], and ease of automation [4, 25].

### **2.4.1 Nd:YAG Laser**

One of the two main workhorses of laser metal processing is the Nd:YAG laser, now fiber laser (the other one is the CO<sub>2</sub>), operating in the near infrared just outside the visible wavelength region, invisible to the human eye [26]. The Nd:YAG laser is commercially available for over 35 years [27]. The source of energy of an Nd:YAG (Neodymium doped Yttrium-Aluminum Garnet) laser is a crystal of Y<sub>3</sub>Al<sub>5</sub>O<sub>12</sub> doped with Nd<sup>3+</sup>. Very small (not more than 1.1 %) amount of Nd<sup>3+</sup> is added to the YAG crystal. As shown in Figure 2.4, laser is produced by exciting the YAG crystal optically by krypton or xenon lamp as an input power [27].

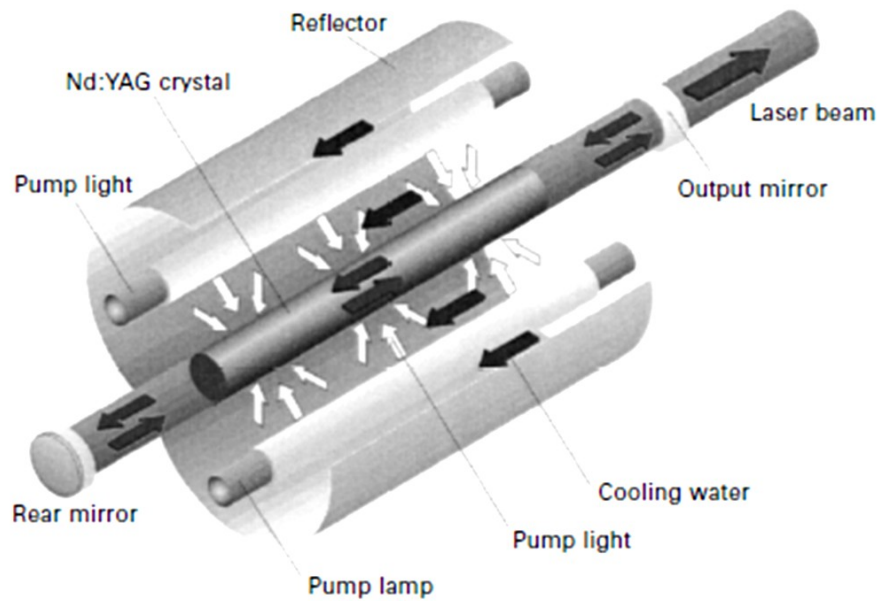


**Figure 2.4: Schematic of an Nd:YAG laser [27]**

### **2.4.2 Laser Welding Mechanism**

Laser welding is performed in either conduction mode or keyhole mode [22]. In conduction mode welding, the beam of a continuous laser is absorbed by the surface of the material and the material below the surface is heated by thermal conduction, producing a semi-circular cross-section. This type of welding is usually done to materials up to 2 mm thick. When the laser power exceeds 1 kW and power density exceeds  $10^6$  W/cm<sup>2</sup>, deep penetration welding can be achieved [28, 29]. At this intensity level, the rapid removal of the metal by vaporization from the surface leads to the formation of a small and narrow keyhole by multiple internal reflection of the beam [30, 31]. The diameter of the keyhole is approximately the same as that of the laser beam. The vapor cavity or the keyhole is surrounded by molten metal. The keyhole forms between 0.6 - 0.8 millisecond after the interaction between Ti-6Al-4V and pulsed Nd:YAG laser [30].

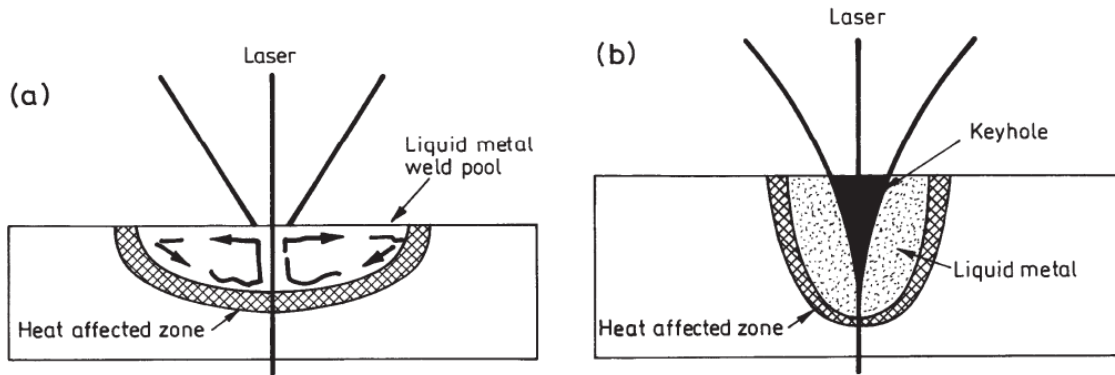


**Figure 2.5: Two different modes of welding (a) conduction and (b) keyhole [22]**

As the beam moves forward, the materials are progressively melted at the leading edge of the molten pool and flows around the keyhole to the back of the pool where it solidifies [32].

The stability of the keyhole depends on the balance between the keyhole and the molten metal around it. This balance can be expressed by the following equation [33, 34]:

$$P_v + P_l = P_\alpha + P_g + P_h \quad (2.1)$$

Where:

$P_v$  = Vaporization pressure

$P_l$  = Radiation pressure

$P_\alpha$  = Surface tension

$P_g$  = Hydrostatic pressure

$P_h$  = Hydrodynamic pressure

As the values of  $P_l$ ,  $P_g$  and  $P_h$  are small, the equation can be simplified as:

$$P_v = P_\alpha \quad (2.2)$$

This means that the stability of the keyhole mainly depends on the balance between the vapor pressure and the surface tension. The vapor pressure tends to open the keyhole whereas the surface tension tends to close it [34, 35].

### **2.4.3 Laser Welding vs. Arc Welding**

Laser welding has shown many advantages over traditional arc welding or tungsten inert gas (TIG) welding in numerous applications based on the very precise and powerful heat source of laser light. For laser keyhole welding, penetration is deeper and welding speed is higher than arc welding. According to a study [36] on phase transformations in weldments, solidification rate of  $10^2$  to  $10^3$  °C/s encountered in conventional arc welding processes, are much lower compared to high-energy density laser processes which reach  $10^5$  to  $10^6$  °C/s as a result of low heat input experienced at high travel speeds.

Residual stress in titanium welds is an important factor because it greatly influences the performance of the aerospace component by reducing fatigue properties. Thus, the use of high-energy-density welding processes such as laser welding to produce full-penetration in a single pass is more desirable than multi-pass conventional arc welding to minimize residual stress and distortion [37]. Laser welding produces much smaller heat affected zone (HAZ) and fusion zone (FZ) than arc welding as the laser is concentrated on a very small area [4, 38].

### **2.4.4 Laser Welding vs. Electron Beam Welding**

As the laser beam can be readily transmitted through air, the laser beam welding (LBW) process offers significant practical advantages over conventional electron beam welding

(EBW), which requires a high vacuum environment. Therefore, the workpiece size is limited in EBW with the size of the vacuum chamber [38, 39]. However, the LBW process is more limited than EBW in case of joining thick titanium plates as the EBW is more powerful [40, 41]. As expected, considering similarities in the heating sources, the metallurgical and mechanical properties of the laser-beam and electron-beam welds are quite similar [4, 37]. The following table [24] shows a comparison between the three popular joining methods for Ti-6Al-4V.

**Table 2.1- Comparison of three different welding methods for Ti-6Al-4V [24]**

Quality	LBW	EB	TIG
Welding rate	√	√	×
Low heat input	√	√	×
Narrow HAZ	√	√	×
Weld bead appearance	√	√	×
Sample fixturing	√	×	×
Welding in air	√	×	√
Weld magnetic materials	√	×	√
Weld reflective materials	×	√	√
Weld heat sensitive materials	√	√	×
Environment, noise and fume	√	√	×

√ point of merit; × point of demerit

### 2.4.5 CO<sub>2</sub> vs. Nd:YAG

Two main types of lasers, CO<sub>2</sub> and Nd:YAG (now fibre laser), react very differently on different materials because of the different wavelengths of the laser beams. The wavelength of an Nd:YAG laser (1.064 microns) is exactly ten times smaller than the CO<sub>2</sub> laser wavelength of 10.64 microns, which makes it ideally suited for absorption in most metals [24, 26]. Recently, Nd:YAG laser has entered the fields dominated by CO<sub>2</sub> laser for its improvement in beam quality and glass fiber delivery system [42]. Due to the

shorter wavelength than CO<sub>2</sub> laser, Nd:YAG produces more stable weld pool with higher welding efficiency [42]. Good quality welds can be produced with lower Nd:YAG laser power than CO<sub>2</sub> laser [42]. Nd:YAG laser light can be transmitted through fibre optic cable instead of mirror delivery system for CO<sub>2</sub> laser. So, it is possible to weld up to a distance of 200m far from the laser source and also it can be delivered to a number of workstations from one source [25].

## **2.5 Laser Weldability of Ti-6Al-4V**

The weldability of an alloy can be defined as the ability to produce a good quality weld joint using specific laser processing parameters. Alloy compositions, welding procedures, and subsequent heat treatments are very much important in determining the final properties of the welded joints [6]. Ti-6Al-4V has been reported as the best weldable among all the  $\alpha$ - $\beta$  alloys [37]. Ti-6Al-4V is prone to change its strength, ductility, and toughness characteristics because of the thermal cycle to which it is exposed to during welding [37]. Proper joining process can make the joint ductile and corrosion resistant like the base metal but improper joining process may lead to the embrittlement and less corrosion resistance [6].

The main difficulties in welding titanium alloys occur due to its high reactivity with atmospheric gases at high temperatures, especially in liquid state which causes weld embrittlement [3] and rapid grain growth [6]. Because of the high welding speed and fast thermal cycle of the laser-beam welding, the material gets a short period of exposure at elevated temperatures, leading to a narrow fusion zone and heat-affected zone, suppressing grain growth [6, 12].

### **2.5.1 Microstructure**

The welds are usually divided into three easily distinguishable regions, FZ, HAZ and, base metal (BM). The FZ is the main region of the weld joint where melting takes place during welding. Adjacent to the FZ is the heat affected zone, which separates the FZ from the base metal. HAZ for Ti alloys can be divided into two subregions according to the temperature experienced during welding. These are near HAZ and far HAZ. The near HAZ is closer to the FZ and exposed to a temperature less than the liquidus but higher than  $\beta$ -transus. On the other hand, the far HAZ close to the base metal is exposed to a temperature less than the  $\beta$ -transus but higher than the temperature required to change the microstructure which depends on transformation kinetics [10].

## **2.6 Laser Welding Parameters**

### **2.6.1 Laser Power and Welding Speed**

The laser power and welding speed are the parameters most often adjusted when defining optimum welding conditions [24]. The total energy per unit length is determined by the laser power and welding speed [43]. When the welding speed is too high, the weld is characterized by a lack of penetration, while at low welding speed the weld exhibits excessive drop out, and excessive porosity [27].

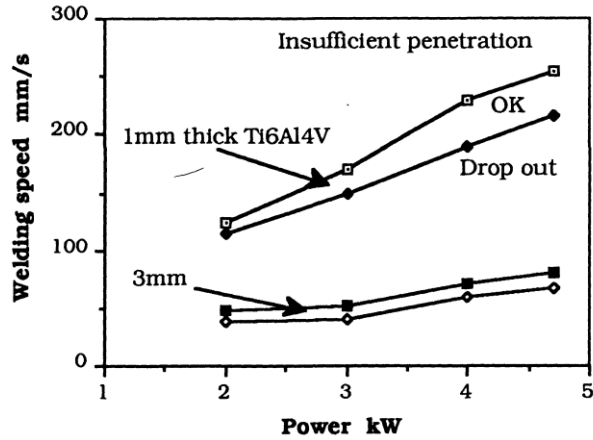


**Figure 2.6: Effect of welding speed and laser power on penetration depth for Ti-6Al-4V [24]**

Figure 2.6 shows the effect of laser power and welding speed for 1mm and 3mm thick Ti-6Al-4V sheets using a CO<sub>2</sub> laser. For a given thickness, the maximum processing speed increases with increasing power. Furthermore, it can be observed that the operating window has been enlarged at higher laser powers. It is also important to note that a high-power density at the workpiece is crucial to achieve and maintain the keyhole mode of welding [24]. Too high a power density, however, can result in spatter, undercut, underfill and dropout [24].

### 2.6.2 Focal Spot Size

The focal spot size is defined as the beam diameter at the focal point [43]. It determines the fineness of the features that can be welded and also the intensity, or power per unit area, at the focal point. Focal spot size is an important factor as the laser material interactions are determined by the power density at the focal point [27]. For a given laser power, the smallest focal spot gives the maximum power density. But the high power density is not always desirable for welding because it may cause extensive evaporation of metals, resulting in the underfill defect. For a small focal spot, the welding geometry will

be very narrow which is sensitive to the alignment accuracy of the joint [43]. For Nd:YAG laser, the focal spot size can be determined by the following equation [43]:

$$d = 2 \times \theta \times F \quad (2.3)$$

Where:

$d$  = Focal spot diameter (mm)

$\theta$  = Beam convergence angle (radians)

$F$  = Focal length (mm)

### 2.6.3 Defocusing Distance

Although the laser energy density is the maximum at the focal point, it decreases along either of the beam axis directions away from the focal point. Defocusing distance is defined by the distance of the focal spot position from the workpiece's top surface. Figure 2.7 shows the different defocusing distances in laser welding. When the focal spot position is above the top surface of the workpiece, it is called positive defocusing (Figure 2.7a). On the other hand, when the focal spot position is below the surface of the work piece, it is called negative defocusing (Figure 2.7c&d). When the focal spot is on the top surface of the workpiece, it is called zero defocusing distance (Figure 2.7b) [43].

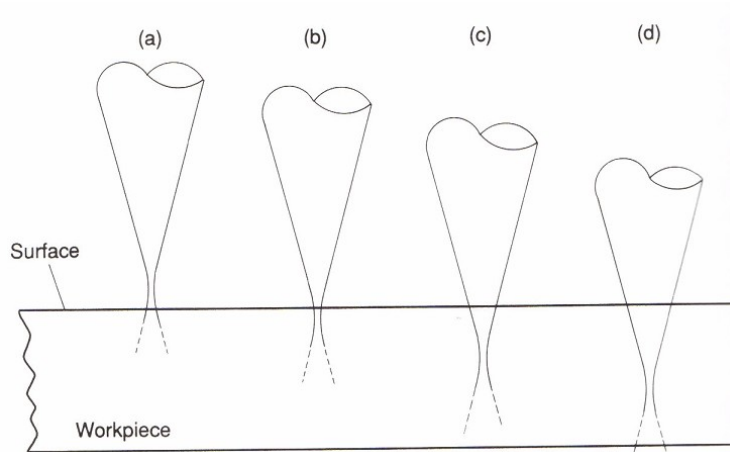


**Figure 2.7- Different defocusing positions in laser welding [43]**

The focal spot should be positioned in such a place that gives the maximum penetration depth. It has been investigated that the focal position below the surface increases the penetration depth for Al alloys due to the enhancement in multiple internal reflections [34, 43].

#### **2.6.4 Shielding Gases**

Titanium is very reactive at high temperature especially in the molten state because it reacts with most atmospheric gases such as oxygen, nitrogen and hydrogen [11]. Hence, special precaution is needed during laser welding of titanium alloys. To protect the molten and heated metal from the atmospheric gases, it is a very common and effective practice to shield the pool and the regions heated above 350 °C with inert gases [34, 43].

The vaporized metal that escapes from the keyhole is easily ionised by the laser heat. Plasma generated by the metal vapours is thus formed at the point of interaction between the beam and the metal. Gaseous plasma can absorb a considerable portion of the beam's energy and reduce the efficiency of the process. Thus plasma is undesirable in laser

welding [44]. The formation of plasma can be limited through using a suitable shielding gas [42].

The shielding gas performs three major roles. First, it protects the weld keyhole and the molten metal from oxidation and thus reduces the formation of oxide inclusions. The second is to suppress plasma formation in the vapour. And finally, it minimizes the effect of plasma by forcing it out from the joint [34, 43]. Shielding gases not only protect the weld pool but also the optics from the metal slag [42].

Helium (He) is lighter than air and is the best shielding gas for laser welding because of its high ionization potential (24.5 eV), high heat conductivity and preserves the transparency of the plasma. On the other hand, argon (Ar) is heavier than air and has lower ionization potential (15.7 eV) than helium [45]. High density gases can give better protection than low density gases as they easily disperse in the welding environment [46].

The gases with higher ionization potential have lower atomic numbers, and hence lighter in weight. The lighter gases are less effective in displacing air from pool area in a short time available at high speed welding. Heavier gases have better performance in this case. Hence a mixture of heavier and lighter gases will be a good combination for a shielding gas [37]. A mixture of He and Ar is used to shield Ti-6Al-4V laser weldment by many researchers [12, 47-49].

The gas flow rate is also an important parameter. At a very low flow rate, the plasma becomes highly absorbent and the interaction of the laser beam with the materials decreases. At a high flow rate the molten pool is blown out of the joints, resulting in a

poor quality weldment [50]. So it is very important to select an appropriate flow rate to have the maximum laser efficiency and good quality joints.

## **2. 7 Joint Gap and Filler Materials**

For laser welding, the beam size is very small. That is why strict fit-up tolerances are compulsory to obtain a good quality weld in the case of autogenous welding [32]. The use of filler materials can reduce this restriction [32, 51] and can also compensate for metal loss due to vaporization, weld drop-through and porosity [42].

Filler-metal composition is usually matched to the grade of titanium being welded [15]. Sometimes, filler metal with yield strength lower than that of the base metal is used to weld unalloyed titanium to improve ductility [37]. For example, the use of unalloyed filler metal can improve joint ductility of Ti-6Al-4V by lowering the beta content of the weldment [37]. Generally, filler metals which contain lower interstitial elements (oxygen, hydrogen, nitrogen, and carbon) or lower alloying elements than the base metal can be used to join titanium [37].

The filler material can be applied in the form of wire, insert or powder. Wire which is fed via a continuous wire feed system is considered to be the most practical and flexible method. Wire has several advantages such as low contaminant pick-up, high productivity and availability of a wide range of filler materials [32]. The most effective method of applying the filler wire is the use of continuous wire feed system. Wire feed rate is dependent on the welding speed, cross section area of the gap and filler wire size as shown by the following equation [43]:

$$\text{Wire feed rate} = \frac{\text{Welding speed} \times \text{Gap area}}{\text{Filler wire area}} \quad (2.4)$$

When the wire is fed into the laser beam, part of the energy is used to melt the wire, part is reflected by the wire, and part passes through the keyhole. Hence, the wire feed angle plays an important role in determining the energy absorbed by the weld [43]. The angle at which it is normally fed lies between 10 and 60 degrees but the best results have been reported to be 45 degrees by Dawes [43]. A smaller angle causes the wire to intersect with a large area of the laser beam, resulting in high reflection in laser beam and vaporization of the wire [43]. However, the use of filler metal requires a higher laser power and a lower weld speed [42].

## **2.8 Welding Defects**

### **2.8.1 Underfill**

The most visible weld defect found by visual inspection is underfill. The main reasons for underfill defects are the evaporation and expulsion of materials [52]. At higher laser power or lower speed (higher heat input), the material may evaporate causing underfill [47, 53]. Spatters may form at higher laser power which is also a reason for underfill formation. At higher speed the cooling rate is faster, so the FZ has shorter time to solidify with proper liquid metal flow all the way causing underfill [52]. The increase in gas pressure may also account for the expulsion of liquid metal, resulting in underfill [54].

Underfill may be avoided by reducing the welding speed, in other words by lowering the rate of solidification [55]. Underfill is a position for crack initiation, degrading tensile

and fatigue properties [32]. Underfill reduces the cross-sectional thickness of the weld and, hence reduces the strength of the weld. Wang *et al.* [53] suggested to reduce the underfill by slightly re-melting the weld surface at increasing focal length and decreasing laser power.

### **2.8.2 Porosity**

Porosity formation in the laser welding process is a major problem. The porosity is mainly caused by the gas bubbles in the molten materials that cannot escape before solidification [3]. Dawes [43] reported that in close fitted butt joints, the deep laser weld which is not fully penetrated through the thickness of the joint is prone to porosity formation. The bubbles have to cross a long route from the root of the weld to the top surface before escaping. For a through penetrated weld, there are two exits and shorter escape routes are available for the bubbles [43]. The other reasons for the formation of gas porosity are the surface grease, oil and dirt existing on the surfaces of the weld pieces and filler materials [42, 56]. Hydrogen is considered to be mainly responsible for the gas porosities in titanium joints [56].

Figure 2.8 shows the solubility curve for hydrogen in titanium as a function of temperature at one atmosphere external pressure [57]. The solubility of hydrogen in both solid and liquid titanium decreases with increasing temperature. The effect of temperature and pressure on solubility of hydrogen in liquid titanium can be presented by the following equation [57]:

$$\log S = 2370 / T_L + 0.626 + 0.5 \log P_{H_2} \quad (2.5)$$

Where,  $S$  is the solubility of hydrogen in liquid titanium (mL/100 g),  $T_L$  is liquidus temperature (K), and  $P_{H_2}$  is equilibrium pressure of hydrogen above the surface of liquid titanium (mm Hg).

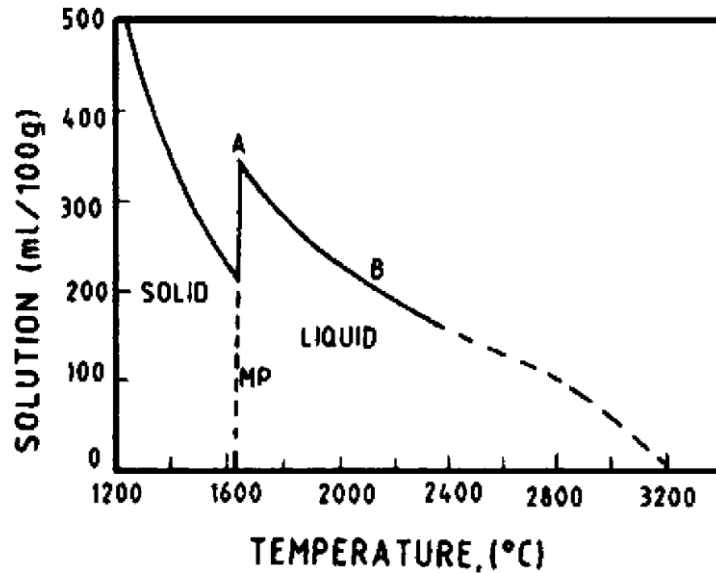


**Figure 2.8- Solubility curve for hydrogen in titanium as a function of temperature at one atmosphere external pressure [57].**

The solubility of hydrogen in liquid titanium decreases with the increase in the temperature of weld pool and the decrease in the partial pressure. Liquid titanium dissolves greater amount of hydrogen than solid titanium at melting point [5]. Therefore, hydrogen will accumulate at the liquid/solid interface during solidification. The evolved hydrogen can form porosity by nucleation or directly diffuses into existing pores. The low density bubbles formed in liquid metal can float up and the driving forces for this are the reduction in free energy of the system [57]. When several small pores coalesce to form a large pore, there will be a net increase in total pore volume due to both coalescence and reduction of surface tension pressure [5]. The mechanism of formation of gas porosity comprises three stages, namely nucleation, growth, and escape [5, 57]. AT

low welding speed, the weld pool will be liquid for a longer time which is favorable for the completion of three stages of the porosity formation mechanism mentioned above. If the speed is too high, the solidification will be very fast and does not favor the growth of bubbles and hence amount of porosity is lower at higher welding speed. At intermediate speeds, the time is sufficient for the nucleation and growth of the bubbles but the pool solidifies before the escape of the bubbles hence the porosity is the maximum [57]. The ranges of these welding speeds vary mainly with the laser power and materials thickness. As the weld center remains at temperature above the solidus for a longer period of time than the FZ/HAZ interface, the high temperature of the melt pool leads to increased fluidity. At locations near the fusion boundary, the temperature is low, and solubility of hydrogen in the liquid at these locations is high. Therefore, hydrogen from the weld center region is likely to diffuse to the FZ/HAZ interface due to the solubility and temperature gradients. Therefore, porosities tend to migrate from the weld center to the FZ/HAZ interface, resulting in decreased porosity at weld center and the presence of porosity near the fusion zone boundary [5, 57]. The center zone of the weld pool is the last region to solidify and thus is usually enriched in hydrogen also. In addition, the hydrogen-rich liquid in the center region has low temperature at the late stage of solidification and hence the gas cannot effectively escape, explaining the porosity in centerline grain boundaries [1].

Another main mechanism for the formation of porosity in titanium welds is the collapse of the keyhole [4]. Keyhole stability is related to the welding speed and the balance between the forces acting on the keyhole (mainly vapour pressure and surface tension) [34]. The keyhole collapses when there is a sudden drop in vapour pressure, resulting in

slumping of the molten metal into the keyhole [13]. Keyhole stability can be achieved at high welding speed only [58]. The pores caused by unstable keyholes are usually located at the lower half of welds [59, 60].

Nozzle angle of the laser and the shielding gasses are also reasons for the porosity formation [3]. The serious problem caused by porosity is the loss of weld cross section when they are large in number and close proximity and this will definitely affect the mechanical properties of the joints [43].

### **2.8.3 Centerline Grain Boundary**

The dendrites growing during solidification from both sides meet along the centerline of the weld, forming a planar centerline grain boundary [61]. A centerline grain boundary is the last region of the weld to solidify and thus is usually enriched in alloying elements and impurities. Therefore, the centerline grain boundaries may have low melting point constituents, eutectic and brittle phases and low toughness compared with other grain boundaries in a weldment [61]. The centerline grain boundaries are usually formed at relatively high welding speeds as typically experienced in laser welding. There is an absence of second-phase dispersoids or precipitates in most titanium alloys such as Ti-6Al-4V and the impurities at grain boundaries are limited. Even so the centerline grain boundary can still constitute a weak area.

### **2.8.4 Sag**

Sag is a weld defect which may be defined as an excessive weld metal flow downwards due to gravitational force [32], low viscosity [62], low cooling rate [63] and collapse of the weld metal [32].

### **2.8.5 Spatter**

Spatter produces when the liquid particles are expelled during welding, which adhere to the surface of the joint [32]. The spherical shape of the spatters indicates that they are solidified from small droplets of liquid metal without restraint resulting in loss of liquid metal [64]. Volatility of the alloying elements and instabilities of the keyhole can be the reasons of spatter [32].

### **2.8.6 Solidification Cracking**

Titanium alloys are generally not considered susceptible to fusion zone solidification cracking like other structural alloys, such as aluminum alloys and many austenitic stainless steels [37]. However, under severe conditions, solidification cracking along columnar beta grain boundaries has been reported by Baeslack [65]. Again titanium alloys are also very resistant to HAZ liquation cracking due to the absence of second-phase dispersoids or precipitate particles, or impurities at the grain boundaries [37].

## **2.9 Post-Weld Heat Treatment**

Two very popular heat treatment processes for Ti-6Al-4V alloy are stress relief annealing and solution heat treatment followed by aging. Stress relief annealing is done at low temperature in the range of 500-600°C followed by quenching. Solution treatment is usually done at high but below the  $\beta$ -transus temperature followed by quenching [66]. Solution treatment is followed by aging to produce a fine mixture of  $\alpha$  and  $\beta$  [15]. Stress relief annealing heat treatment increases the hardness and the tensile strength but decreases the ductility of the fusion zone as reported by Wang *et al.* [53] and Baeslack *et*

*al.* [67]. Solution heat treatment at high temperature followed by aging increases the ductility and decreases the hardness of the fusion zone as reported by Thomas *et al.* [68].

## **2.10 Mechanical Properties**

The goal of any weld is to create a structure that can meet all the demands of its service environment. In many cases, the best way of assessing the performance of a weld is to establish its mechanical properties. The strength across a laser weldment is determined by the strength of the weakest link in the composite weld region, which consists of the fusion zone, the near HAZ, the far HAZ and the BM [53]. The mechanical properties of the different zones may change due to the temperature experienced during the laser welding process.

### **2.10.1 Hardness**

Hardness values are commonly used to determine the less ductile phases in the weldment which may be prone to cracking [37]. Akman *et al.* [3] observed a large increase in FZ hardness in laser welded Ti-6Al-4V due to the high cooling rate associated with the formation of  $\alpha'$  martensite. Cao *et al.* [47] reported the lowest hardness in the BM and the hardness value increases from the HAZ to the FZ. Although Cao *et al.* [47] did not find any relation between the FZ average hardness and welding speed, Sun *et al.* [69] demonstrated the increase in FZ average hardness with increasing welding speed.

## 2.10.2 Tensile Properties

### *Global Tensile Property*

Tensile ductility of the Ti-6Al-4V is directly affected by the FZ and HAZ dimensions, microstructure, grain size, and weld defects [14]. The weld ductility can be degraded by the coarse prior- $\beta$  grain size due to the tendency of crack propagation along the prior- $\beta$  grain boundary [37]. Laser welding produces smaller prior- $\beta$  grain size than conventional arc welding process due to the lower heat input and higher cooling rate [37]. Cao *et al.* [47] showed that for 2-mm thick Ti-6Al-4V samples, the yield and tensile strength increase with increasing welding speed. The use of filler wire can significantly increase the tensile strength by reducing the underfill defect [48].

### *Local Tensile Property*

The weld is similar to a composite structure, consisting of the BM, HAZ and FZ with various microstructures. It is expected that each zone will have different mechanical properties. Although the global mechanical properties provide useful information, it presents no details on the local behavior of the different weld zones. As the global mechanical property of a weld is dependent on the combination of the local constitutive behavior of each zone, it is necessary to explore the local tensile behavior of the weld to clarify process-structure-property correlation. Local hardness and microstructure have been well characterized by many researchers. To date, the local mechanical properties of the friction stir welded aluminum alloys [70, 71] and the laser welded stainless steel [72] have been investigated but no literature is available on local mechanical properties of the laser welded Ti alloys.

### 2.10.3 Digital Image Correlation

Digital image correlation (DIC) is a very popular method and has been used by researchers for many years to study the stress and strain in machine parts. It is a non-contact optical technique that is capable of measuring full-field two-dimensional or three-dimensional surface deformations. DIC is highly sensitive method with wide tolerances in sample sizes, and requires a very simple surface treatment of the samples [73-76].

Figure 2.9 shows a simple schematic of a 3-D DIC technique indicating orientations for the two cameras and specimen. In general, when one camera is used, it is called 2-D DIC, and when two cameras are used, it is called 3-D DIC. There have been several works reported regarding 2-D DIC by He *et al.* [77]. In addition, Chu *et al.* [75, 78] developed and adapted the method for a wide range of applications. Recently, other researchers expanded DIC to include stereo-vision methodologies and associated applications [70, 71].

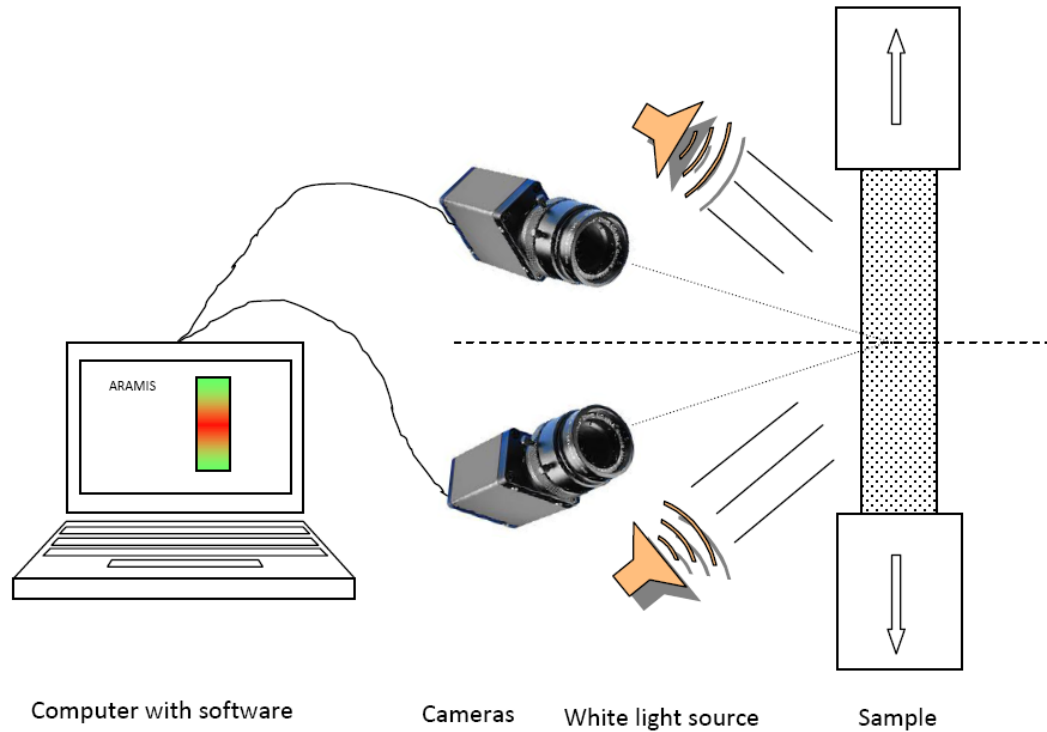


**Figure 2.9- Schematic of a 3-D DIC system**

Monocular vision (single camera) of 2-D DIC system is not capable to measure out-of-plane displacement. 3-D DIC is based on a binocular vision system (stereo-vision system) which is similar to the human depth perception and is capable to measure both in-plane and out-of-plane displacements [79].

DIC compares two digital images; one is the target image (image of specimen in a reference state) and the other one is source image (image of specimen after deformation). An intensive calibration process of the two cameras is required for the digital image correlation algorithm to get the accurate information about the placement and characteristics of the two cameras [70, 71].

The DIC algorithm searches for one-to-one correspondence of the points (pixels) in both images by matching all the pixel intensities in an area with a unique image pattern [79]. The single most popular type of images used in DIC is gray-scale image with random speckles. The size of the random speckles is very important and usually is very fine, on the scale of 1-100 microns. It can be black speckles on white background or vice versa. Usually the speckle pattern is generated by spraying either black or white paint using refined airbrush [70, 71, 79].

Several commercial softwares are available such as ARAMIS, Vic-3D, StrainMaster, Q-400, etc [80]. Here in this study, the DIC measurement is carried out with an ARAMIS 3D optical deformation analysis system developed by GOM (Gesellschaft für Optische Messtechnik), Germany.

## **Chapter 3 / Experimental Procedures**

---

### **3.1 Material and Equipment**

The material used is grade 5 Ti-6Al-4V titanium alloy sheets with two thicknesses of 3.175 mm and 5.08 mm. The dimensions of the samples used are approximately either  $102 \times 63$  mm or  $75 \times 38$  mm. The samples have been welded with the length in the welding direction. For each thickness, the large samples ( $102 \times 63$  mm) have been butt welded autogenously while the small samples ( $75 \times 38$ ) have been welded with the use of a filler wire. The surfaces of all specimens are brushed and cleaned by methanol to remove any contaminants prior to the clamping and welding. The sheets were laser welded at Aerospace Manufacturing Technology Center (AMTC), Institute for Aerospace Research (IAR), of the National Research Council of Canada (NRC) located in Montreal, Quebec, Canada.

The welding equipment used is a 4 kW continuous wave (CW) solid-state Nd: YAG laser system equipped with an ABB robot and a magnetic holding fixture. A collimation lens of 200 mm, a focal lens of 150 mm and a fibre diameter of 0.6 mm have been employed to produce a focusing spot diameter of approximately 0.45 mm. The weld surfaces are shielded by inert gases due to the high reactivity of titanium with oxygen at high temperature. High purity argon at a flow rate of 23.6 l/min (50 cfh) is used to shield the top surface of the work-piece and a mixture of argon and helium (50-50 in vol %) at a total flow rate of 66.1 l/min (140 cfh) is used to shield the bottom surface and the trails of the top surface. In the first part, the 3.175 mm thick samples have been autogenously welded at various welding speeds and laser powers. The heat input is calculated by laser

power divided by welding speed. In the second part, the 5.08 mm thick samples were welded at a laser power of 4.0 kW but at various welding speeds and defocusing distances. Effect of joint gap is investigated for 3.175 mm thick samples at welding speed of 1.69 m/min and 3.0 kW laser power, and for 5.08 mm thick samples at welding speed of 1.0 m/min and 4.0 kW laser power. Ti-6Al-4V filler wire with a nominal diameter of 1.14 mm is used at a 30° angle relative to the top surface of the workpiece. The wire feed rate is calculated from the volume flow rate constancy equation 2.4.

The effect of post-weld heat treatment (annealing, full heat treatment, i.e. solution treating + aging) have been investigated and compared with the as-welded joints for both thicknesses. Samples selected for post-weld heat treatment have been welded at 0.3 mm joint gap for both thicknesses. Three metallurgical specimens are cut from each joint for metallographic examination. The specimens are mounted using cold-setting epoxy resin, ground and polished to produce a mirror-like finish. Kroll's reagent (1-3 mL HF + 2-6 mL HNO<sub>3</sub> + 100 mL H<sub>2</sub>O) is used for 6 – 10 s, depending on the zones of interest. Microstructural examination has been carried out using an Olympus Inverted System Metallurgical Microscope GX71 equipped with an Olympus digital camera XC50 and AnalySIS Five digital image software. The Vickers micro-indentation hardness was measured using a Struers Duramin A-300 hardness tester at a load of 500 g, a dwell period of 15 seconds and an interval of 0.2 mm. According to the E384-89 ASTM standards (Standard Test Method for Micro-hardness of Materials), the spacing between two adjacent indentations must be at least three-time the diagonal length of the indentation. The diagonal length of the indentation is approximately 50 microns and therefore, a spacing of 200 microns (0.2 mm) is used in this work to acquire as much

hardness values as possible especially in the narrow HAZ. Three or four tensile samples are prepared according to the E8M-04 ASTM standards (Standard Test Methods for Tension Testing of Metallic Materials). Two samples are tested using the digital image correlation technique by using the software ARAMIS with a 250 kN MTS machine at AMTC-NRC. The surface treatment of the sample is done by painting a thin layer of white color followed by black speckles pattern using two refined airbrushes. The remaining tensile samples are tested at Concordia University by using an MTS-100 kN tensile test machine with a laser extensometer. All the tensile samples are tested at room temperature and at a constant crosshead rate of 2 mm/min.

### **3.2 Key Experiments**

To investigate the weldability of 3.175 and 5.08 mm thick butt joint sheets of Ti-6Al-4V with or without the use of a filler wire, following subtasks are defined:

- **Effect of laser power and welding speed on the weldability of 3.175 mm sheets**

The objective of this task is to investigate the weldability of 3.175 mm thick samples welded autogenously at various welding speeds and laser powers. The welding speeds are varied from 0.75 - 7.5 m/min and the laser powers are 2, 3, and 4 kW.

- **Effect of welding speed and defocusing distance on the weldability of 5.08 mm sheets**

The objective of this task is to investigate the weldability of 5.08 mm thick samples welded autogenously at different welding speeds and defocusing distances. The laser

power is constant (4 kW) in this process. Welding speeds are varied from 0.75 - 2.0 m/min and defocusing distances are -1 mm and -2 mm.

- **Effect of joint gap on the weldability of 3.175 and 5.08 mm sheets**

The effect of joint gap is investigated in this process for both 3.175 and 5.08 mm thick samples. Laser powers are 3 kW and 4 kW for thin and thick samples, respectively. Joint gaps are varied from 0.1 to 0.6 mm and the results are also compared with the autogenous welding at zero joint gaps.

- **Effect of post-weld heat treatment on the weldability of 3.175 and 5.08 mm sheets**

In this study, two post-weld heat treatment conditions have been investigated for both thicknesses. The stress relief annealing is carried out by heating the samples to 538°C for 4 hours followed by argon quenching while the full heat treatment (STA: solution treatment + aging) is carried out by heating the samples to 913°C for 45 minutes followed by argon quenching and then aging at 538°C for 4 hours followed by argon quenching. The samples are then compared with the as-welded condition.

### **3.3 Weld Geometry**

Figure 3.1 shows the different terms related to the weld geometry. All the dimensions are measured to evaluate the quality of the weld. All measurements of the transverse sections of the specimens have been taken using the AnalySIS Five image analysis system. A magnification of 50X is used to take the pictures for transverse section and 1000X is used

to take the pictures for microstructure. Various magnifications are used to take the best pictures for the defects.

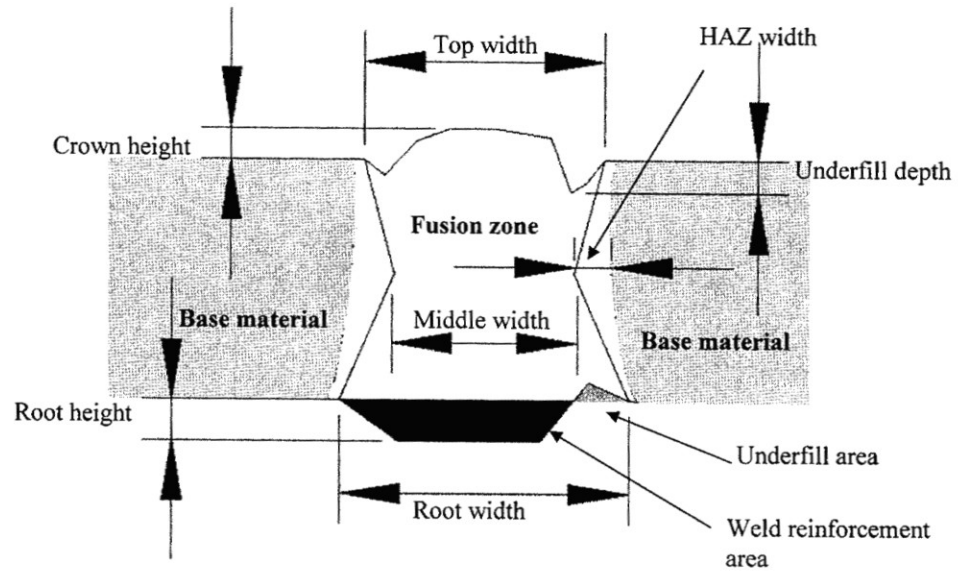


**Figure 3.1- Weld geometry of a typical butt joint**

## **Chapter 4 / Effect of Laser Power and Welding Speed**

The effect of laser power and welding speed on the weldability of 3.175 mm thick samples has been investigated at a defocusing distance of -1 mm as shown in Table 4.1.

**Table 4.1: Key experiments / effect of laser power and welding speed**

Sample #	Laser power (kW)	Welding speed (m/min)	Defocusing distance (mm)	Heat input (J/mm)	Notes
T 68	4.0	3.0	-1	80	
T 66	4.0	4.5	-1	53	
T 58	4.0	6.0	-1	40	
T 67	4.0	7.5	-1	32	
T 114	3.0	1.13	-1	160	
T 118	3.0	1.69	-1	106	
T 112	3.0	2.25	-1	80	
T 113	3.0	3.38	-1	53	
T 111	3.0	4.5	-1	40	LOP*
T 119	3.0	4.5	-1	40	2nd side welding of T 111
T 116	2.0	0.75	-1	160	
T 117	2.0	1.13	-1	106	
T 115	2.0	1.50	-1	80	

\* LOP = Lack Of Penetration

### **4.1 Weld Geometry**

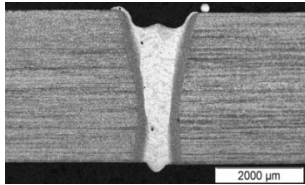
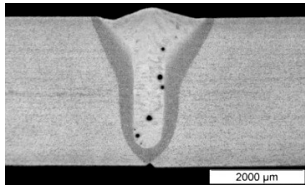
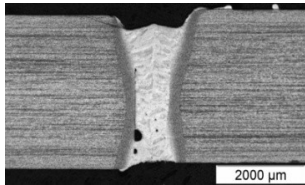
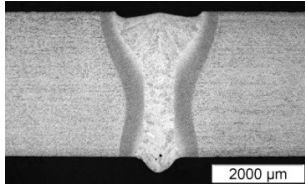
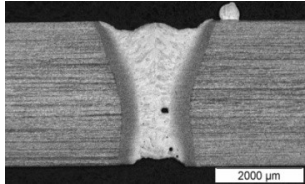
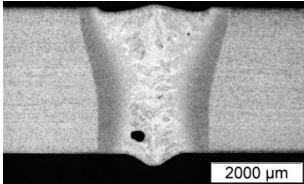
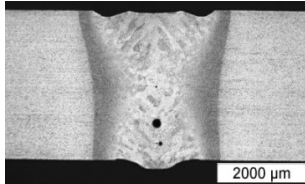
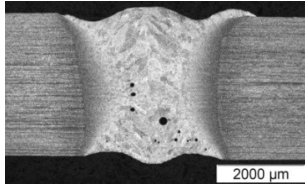
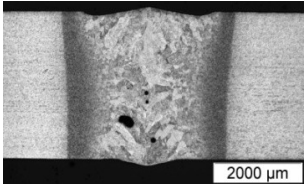
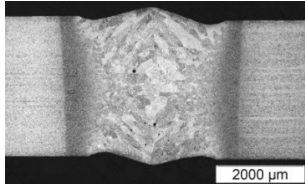
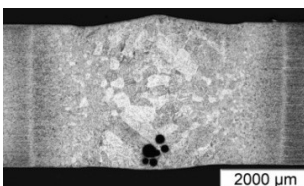
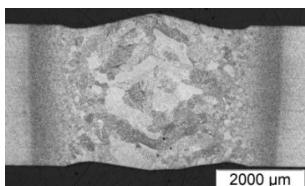
The transverse sections are shown in Figure 4.1. At a laser power of 2 kW, fully penetrated weld joints are obtained at welding speeds from 0.75 m/min to 1.5 m/min. However, at a speed of 0.75 m/min, wide FZ and HAZ are observed and at a welding speed of 1.5 m/min a narrow root is accompanied by sagging and underfill defects.

At a laser power of 3 kW, fully penetrated joints are found at welding speeds from 1.13 m/min to 3.38 m/min. However, for 1.13 m/min the weld bead is wide and for 3.38

m/min the narrow root, sagging and underfill defects are observed. At a welding speed of 4.5 m/min, the lack of penetration defect appears.

At a laser power of 4 kW, the samples are welded at speeds from 3.0 m/min to 7.5 m/min, and full penetrations are found for all the speeds. But in all the cases underfill and overlapping defects are observed. Sagging appears at a speed of 7.5 m/min where severe underfill defect is found on the top as well.

Full penetration can be obtained either at high power and high speed, or at low power and low speed. At higher laser power, however, the speed window for full penetration becomes wider.

LP (kW) HI (J/mm)	2	3	4
32			 <p>T 67 (7.5 m/min)</p>
40		 <p>T 111 (4.5 m/min)</p>	 <p>T 58 (6.0 m/min)</p>
53		 <p>T 113 (3.38 m/min)</p>	 <p>T 66 (4.5 m/min)</p>
80	 <p>T 115 (1.50 m/min)</p>	 <p>T 112 (2.25 m/min)</p>	 <p>T 68 (3.0 m/min)</p>
106	 <p>T 117 (1.13 m/min)</p>	 <p>T 118 (1.69 m/min)</p>	
160	 <p>T 116 (0.75 m/min)</p>	 <p>T 114 (1.13 m/min)</p>	

**Figure 4.1- Effect of heat input on transverse sections**

Figure 4.2 shows the relationships among welding speed, laser power, heat input, and FZ and HAZ dimensions. It is seen that with increasing welding speed at a given laser power, the FZ and HAZ areas decrease. At a given welding speed, the FZ and HAZ areas increase with increasing laser power. The iso-heat input values are indicated by the same color in the graphs. It is seen that at a given heat input, larger FZ and HAZ areas can be obtained at higher laser power. For fully penetrated joints, the smaller FZ and HAZ areas can be obtained at lower power or speed at a given heat input. However, the minimum FZ and HAZ areas are obtained at high laser power with low heat input.

The FZ top and root widths follow similar tendency as the FZ and HAZ areas. The FZ middle width also decreases with increasing welding speed but remains relatively constant over welding speed above approximately 2 m/min.

Figure 4.3 shows the relationship between welding speed and weld reinforcement at laser powers of 2, 3 and 4 kW. The crown height decreases with increasing welding speed. The large crown height obtained at lower welding speed is probably due to the expansion and flotation of the gas pores. At the lower welding speed the gas porosities have longer time available to nucleate and grow. On the other hand, the root height increases at 2-3 kW but decreases at 4 kW with increasing welding speed. At the welding speed of 7.5 m/min, the root height is again the maximum due to the sagging defect, resulting in a large underfill area on the top surface. Both the top and bottom reinforcement areas decrease with increasing welding speed. Therefore, the similar tendency can be obtained for the total reinforcement area.

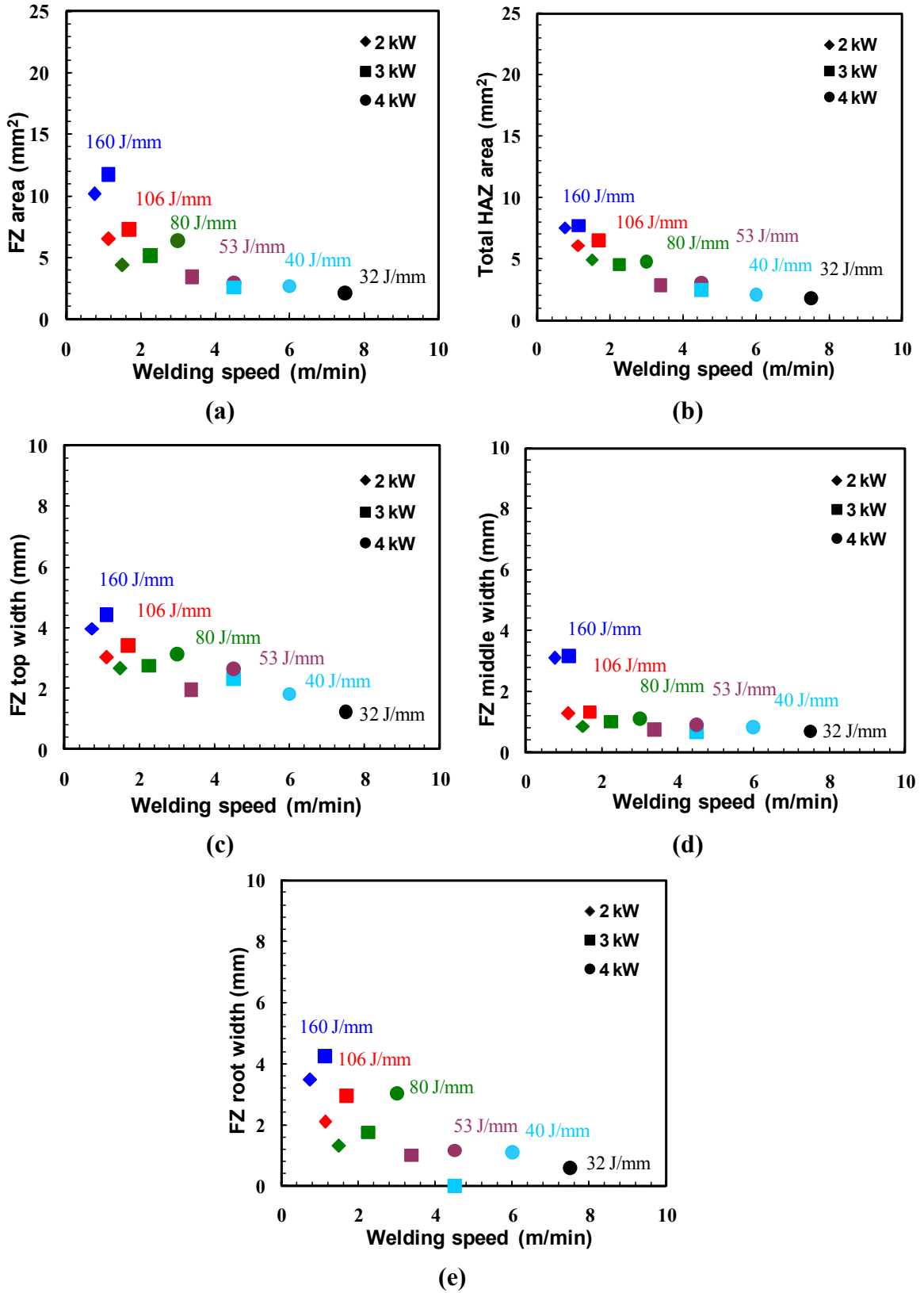
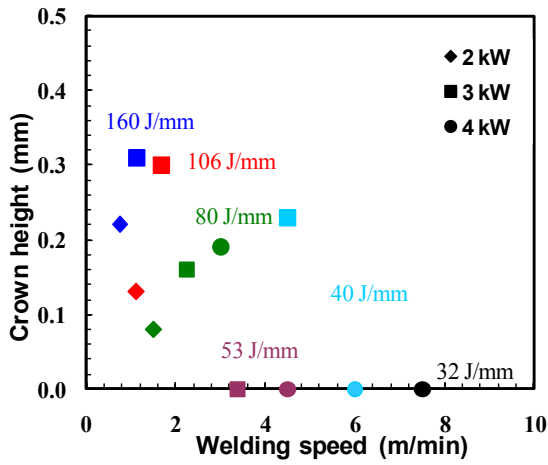
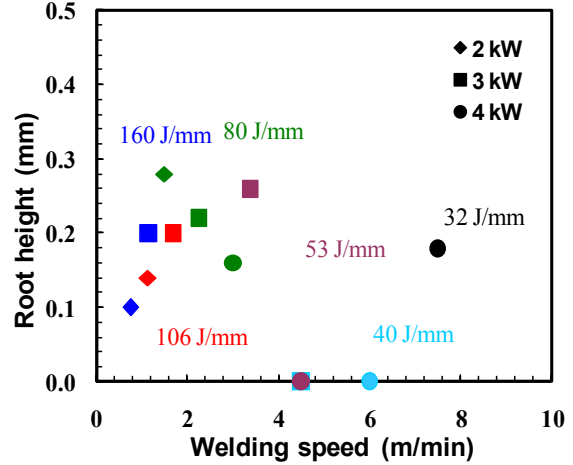


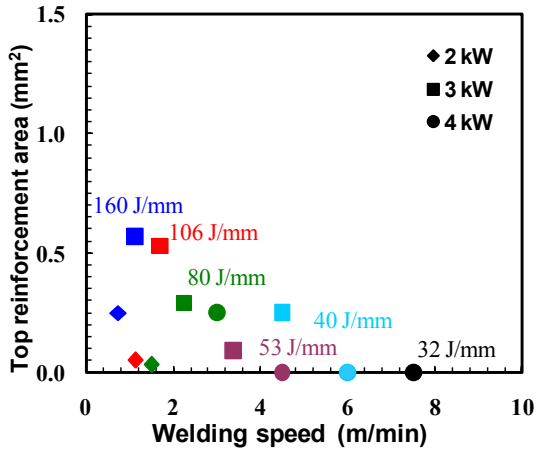
Figure 4.2- Effect of laser power and welding speed on FZ and HAZ dimensions



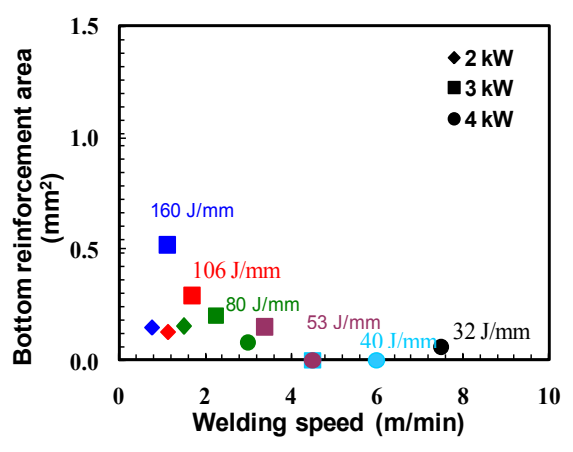
(a)



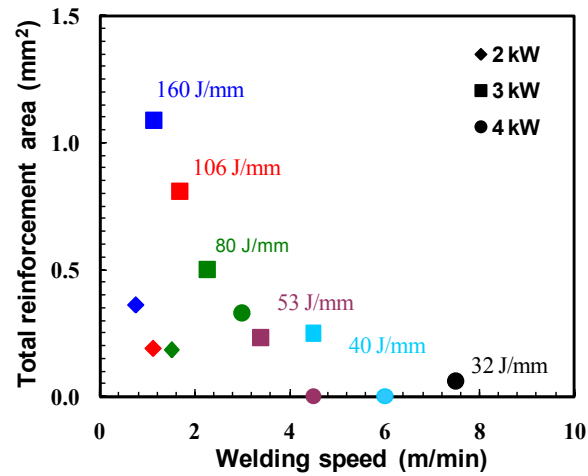
(b)



(c)



(d)



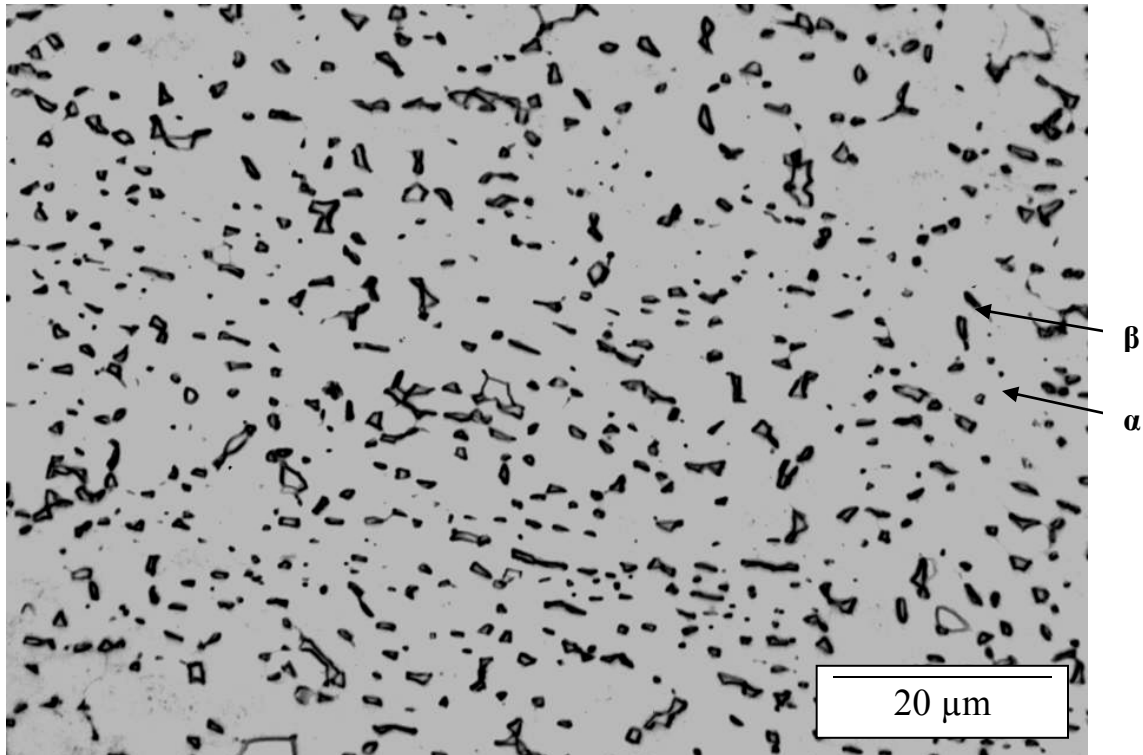
(e)

Figure 4.3- Effect of laser power and welding speed on weld reinforcement dimensions

Although higher laser power (4 kW) provides a wider range of welding speed for fully penetrated welds, the weld geometries are investigated for the samples welded in the range of 3 to 7.5 m/min welding speed. Lower welding speed than 3 m/min may generate wider welds and cause more overlap as observed at 4 kW. Higher welding speed than 7.5 m/min may create more underfill or even drop-out. In addition, severe underfill is obtained at 4 kW (Figure 4.1). Therefore, 4 kW power is too high for the 3.175 mm thickness and is not recommended. The samples welded at 2 kW laser power, welding speeds of 1.13 m/min and at 3 kW laser power, welding speeds of 1.69 and 2.25 m/min show relatively smooth crown and root heights with narrow and uniform weld widths, which are the optimum weld geometries obtained among the tested samples.

## **4.2 Microstructure**

The microstructure of the BM consists of equiaxed  $\alpha$  with intergranular  $\beta$  (Figure 4.4). The dark regions are intergranular  $\beta$  and bright regions are equiaxed  $\alpha$ . The  $\alpha$  -  $\alpha$  grain boundaries are not well defined. This microstructure is a typical mill-annealed structure of Ti-6Al-4V alloy. Mill annealing is done to place the alloy in a soft and relatively machinable condition by heating to about 730°C for 4 hours and then furnace cooling to room temperature [15].



**Figure 4.4- A typical base material microstructure of Ti-6Al-4V alloy in mill-annealed condition**

The microstructure of the fusion zone (Figure 4.5) mostly consists of  $\alpha'$  martensite with acicular morphology which is a result of diffusionless transformation of the  $\beta$ -phase [10]. There is still some retained  $\beta$  available in the microstructure due to the presence of  $\beta$ -stabilizer (Vanadium). Vanadium brings the martensite formation temperature below the room temperature, resulting in some remaining  $\beta$  always present [15]. The  $\alpha'$  martensite is a supersaturated non-equilibrium hexagonal  $\alpha$ -phase. The volume fraction of  $\alpha'$  increases with increasing cooling rate [37].

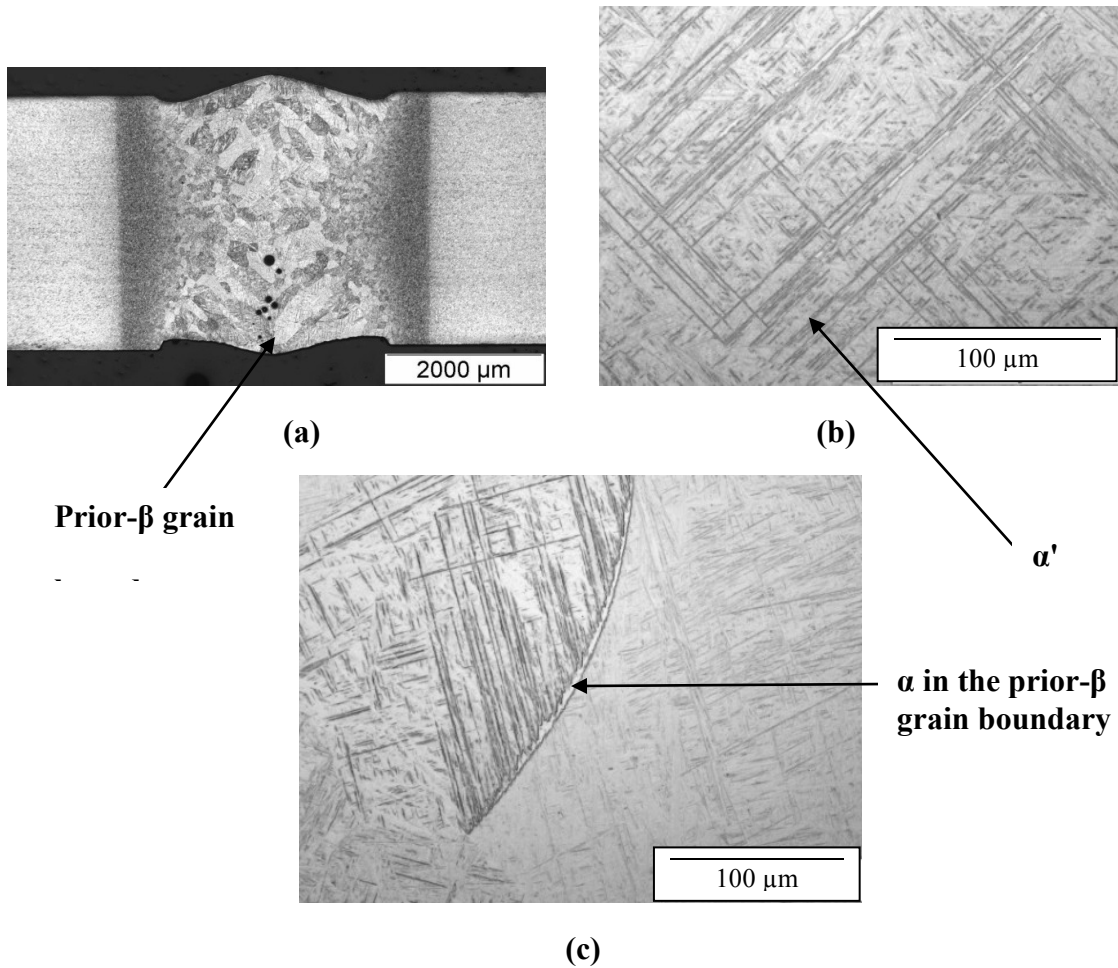
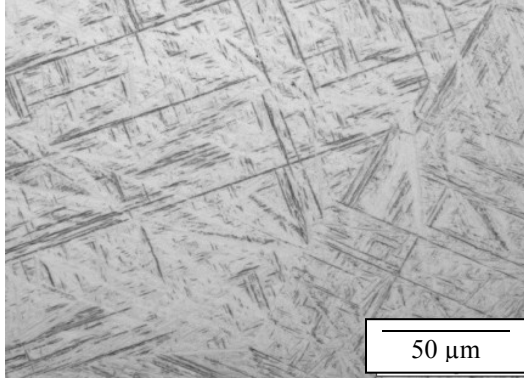


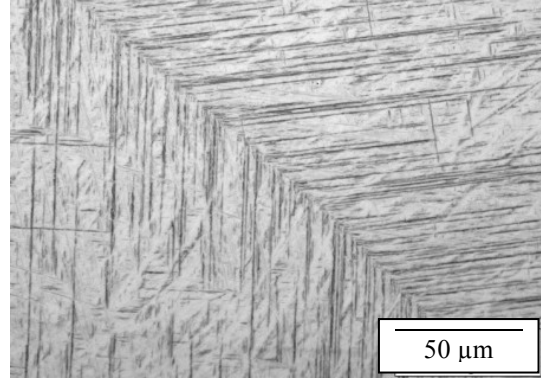
**Figure 4.5- Typical FZ microstructures at 3 kW and 1.69 m/min**

In Figure 4.5a, prior- $\beta$  grain boundaries are clearly exposed in the FZ structures. The presence of  $\alpha$  in the prior- $\beta$  grain boundary (Figure 4.5c) indicates that the cooling rate is close to the lower limit of  $\alpha'$  forming cooling rate which has been reported to be approximately  $410^{\circ}\text{C/s}$  [20].

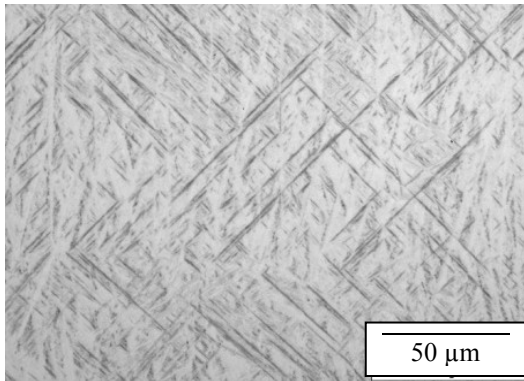
In Figure 4.6, the effect of welding speed on the FZ microstructure at three laser powers is shown. No significant differences in the FZ microstructure are observed at different welding speeds under the optical microscope.



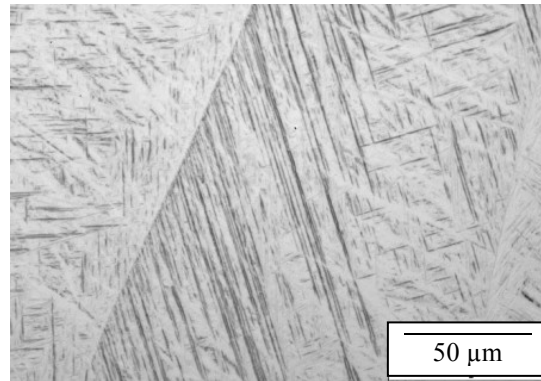
**(a) 2 kW, 0.75 m/min**



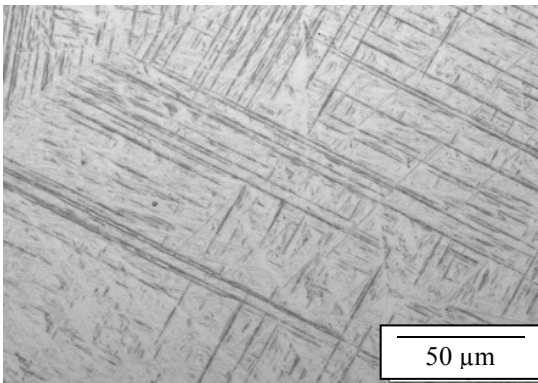
**(b) 2 kW, 1.13 m/min**



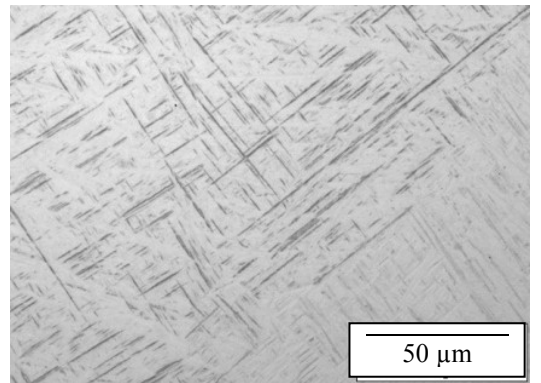
**(c) 2 kW, 1.5 m/min**



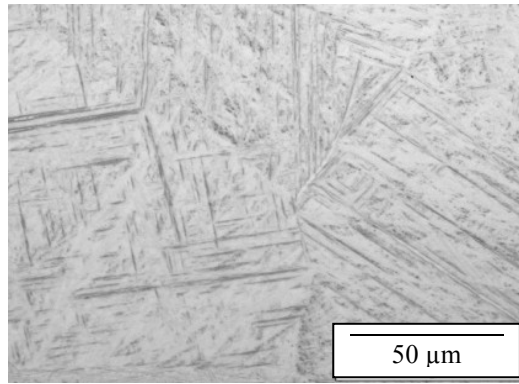
**(d) 3 kW, 1.13 m/min**



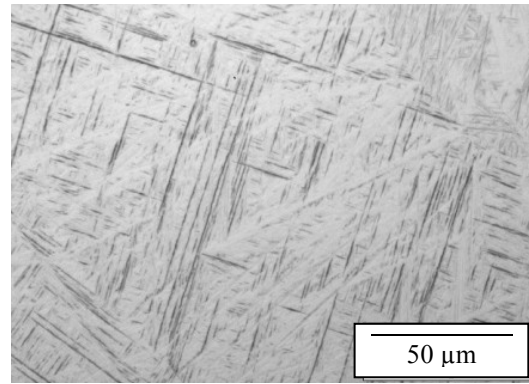
**(e) 3 kW, 1.69 m/min**



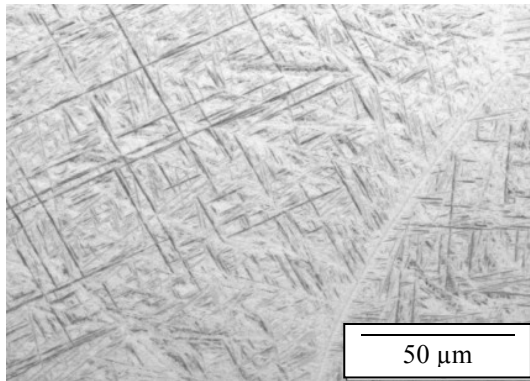
**(f) 3 kW, 2.25 m/min**



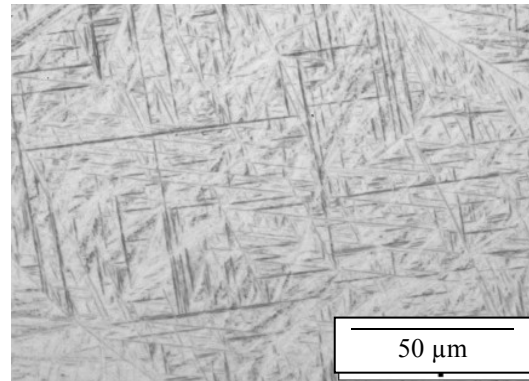
**(g) 3 kW, 3.38 m/min**



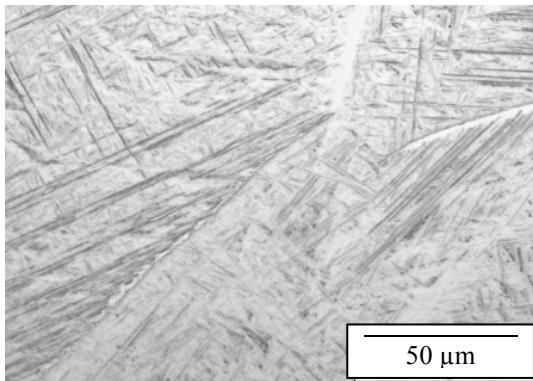
**(h) 3 kW, 4.50 m/min**



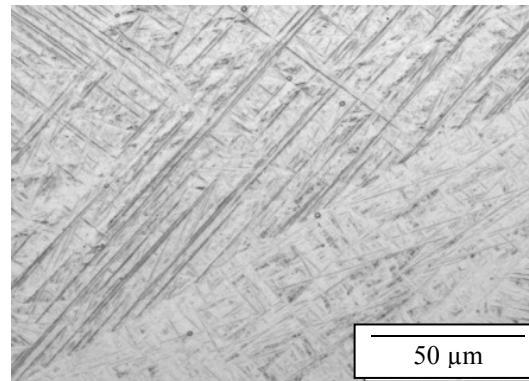
**(i) 4 kW 3.0 m/min**



**(j) 4 kW, 4.5 m/min**



**(k) 4 kW, 6.0 m/min**



**(l) 4 kW, 7.5 m/min**

**Figure 4.6- Effect of laser power and welding speed on FZ microstructures**

The HAZ can be easily distinguished from the other zones as shown in Figure 4.1. It is obvious that the near HAZ (close to FZ) experiences higher temperature during welding than the far HAZ (close to BM). The near HAZ region is cooled from above  $\beta$ -transus but

below the liquidus temperature and the far HAZ region is cooled from below  $\beta$ -transus temperature but sufficient to change the microstructure. Figure 4.7 shows the microstructures of three locations in the HAZ. The near HAZ consists of almost 100%  $\alpha'$  martensite with a very small amount of  $\alpha + \beta$ . The middle HAZ consists of a mixture of primary  $\alpha$  and  $\beta$ -phases with  $\alpha'$ . The far HAZ consists of  $\alpha + \beta$  with small amount of  $\alpha'$ . The volume fraction of  $\alpha'$  decreases from the near HAZ to the far HAZ.

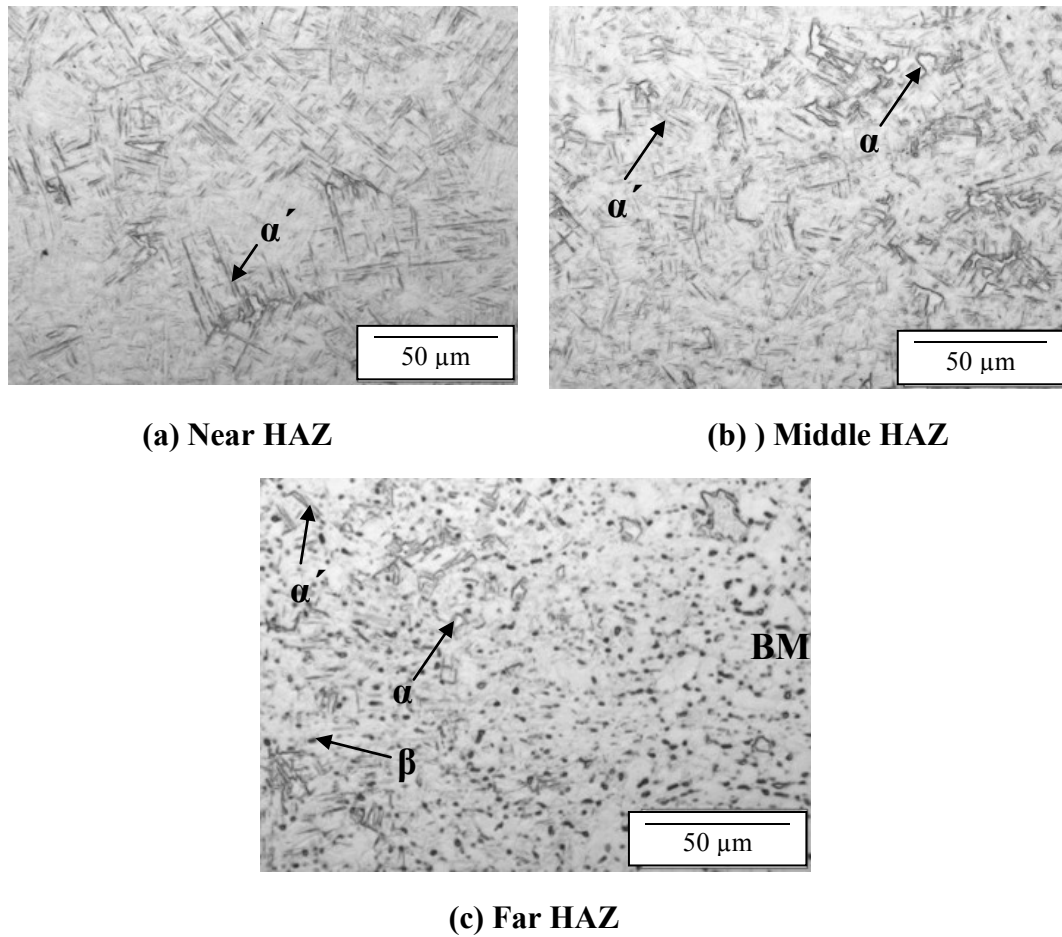


Figure 4.7- Microstructures of heat affected zone at 3 kW and 1.13 m/min

## 4.3 Defects

### 4.3.1 Underfill

As shown in the Figure 4.1, the underfill defect is frequently observed on both the top and root surfaces. Figure 4.8 shows the effect of laser power and welding speed on top and root underfill depth and total underfill area. It is seen that the top maximum underfill depth increases with increasing welding speed for all the laser powers. This may be due to the less time available for the liquid metal flow to fill the groove completely at higher welding speed. The bottom maximum underfill depth decreases with increasing welding speed for laser powers of 2 and 3 kW. Higher bottom maximum underfill depth is obtained at higher laser power due to the increased evaporation of the molten metal. According to the Aerospace specification for fusion welding (AWS D17.1) [81], the acceptable criterion under class A for maximum underfill depth for 3.175 mm thick sample is  $3.175 \times 0.07 = 0.222$  mm for each side. In Figure 4.1.8a, this underfill limit is shown by a horizontal dashed line. At lower laser powers of 2 and 3 kW, all the samples are within the acceptable specification. For 4 kW laser power, the values are very close to the acceptable line at lower welding speed but almost twice more than the specification value at higher welding speed. Therefore, a laser power of 4 kW is not recommended for laser welding of 3.175 mm thick Ti-6Al-4V alloy.

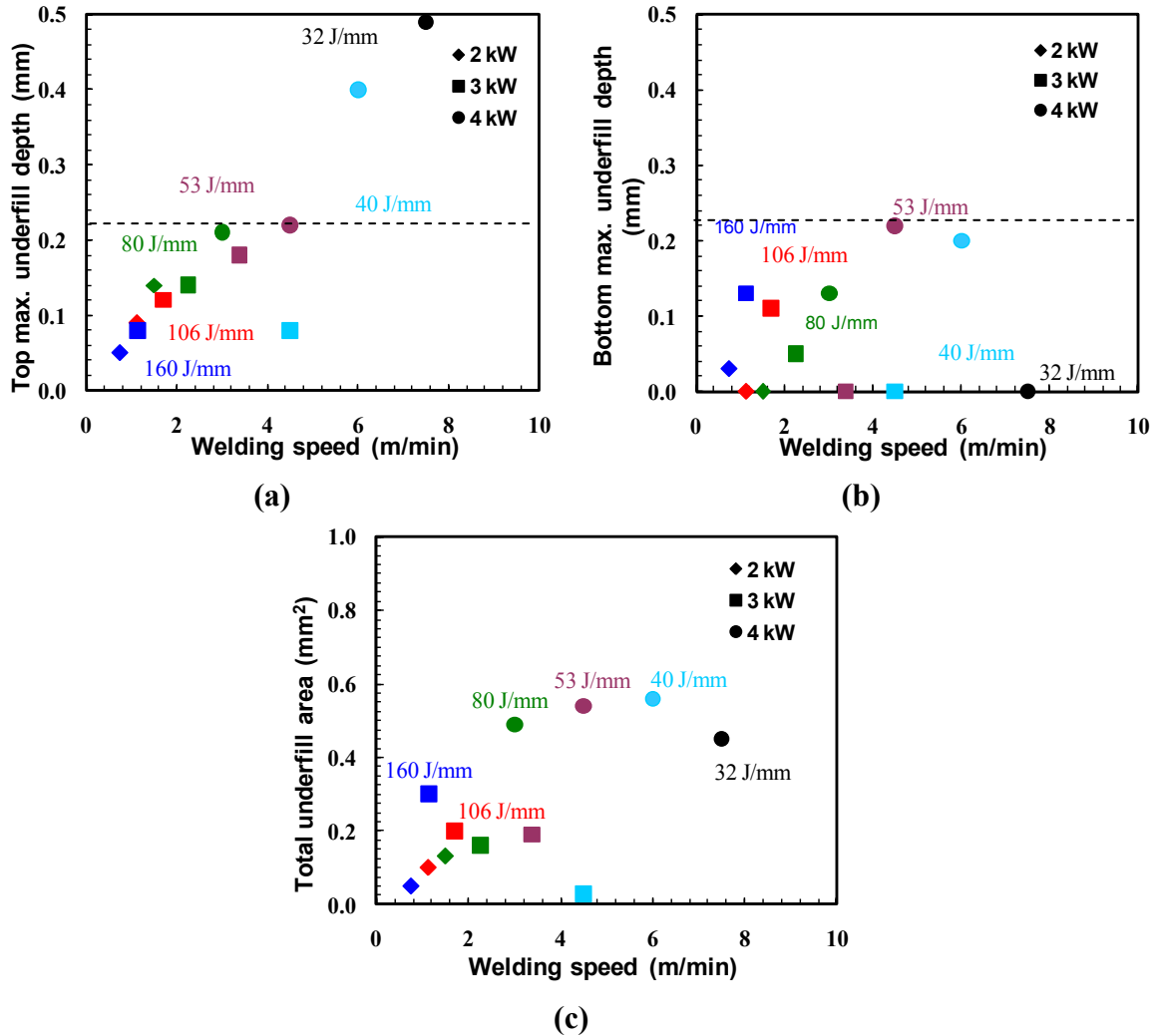
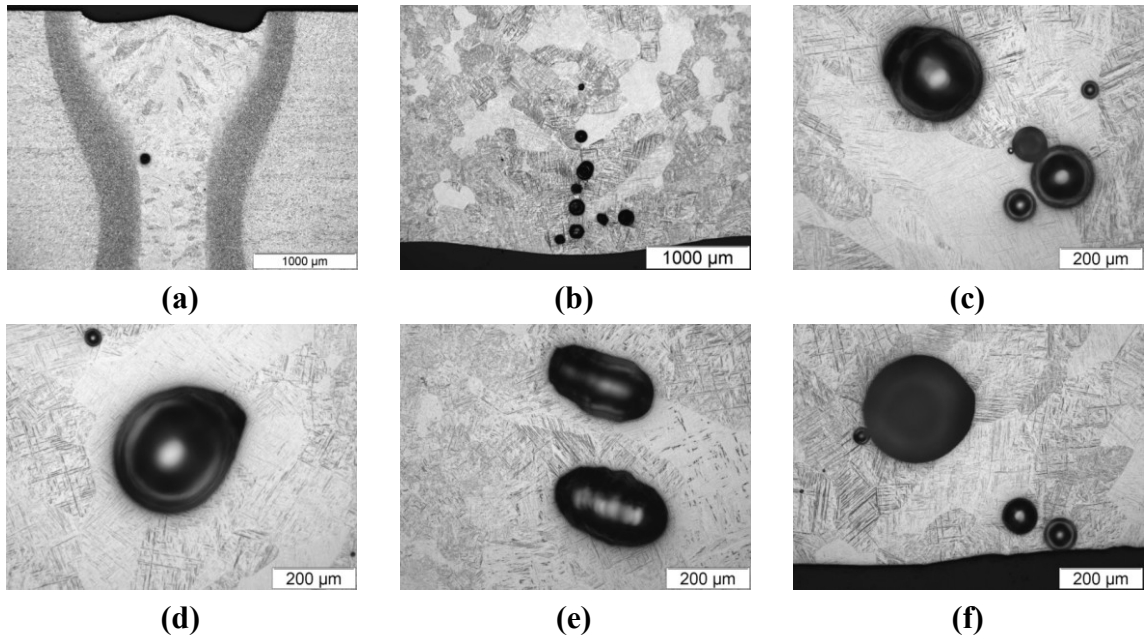


Figure 4.8- Effect of laser power and welding speed on underfill

### 4.3.2 Porosity

Porosity is one of the main issues encountered in Ti alloy laser welding. There are several types of porosity as observed in this work (Figure 4.9). Centerline porosity is observed in most of the samples. Some porosity appears near the FZ/HAZ interface but most are located at the lower half of the FZ. There are also some scattered porosities present in some samples. The porosity is mainly caused by the gas bubbles either already in the molten materials or entrapped during welding that cannot escape before solidification.



**Figure 4.9- Typical porosities observed in the welded joints**

The size and area of porosity are measured in order to understand their evolution with welding speed. Figure 4.10 shows the effect of laser power and welding speed on the porosity area and percentage of porosity area (porosity area/FZ area).

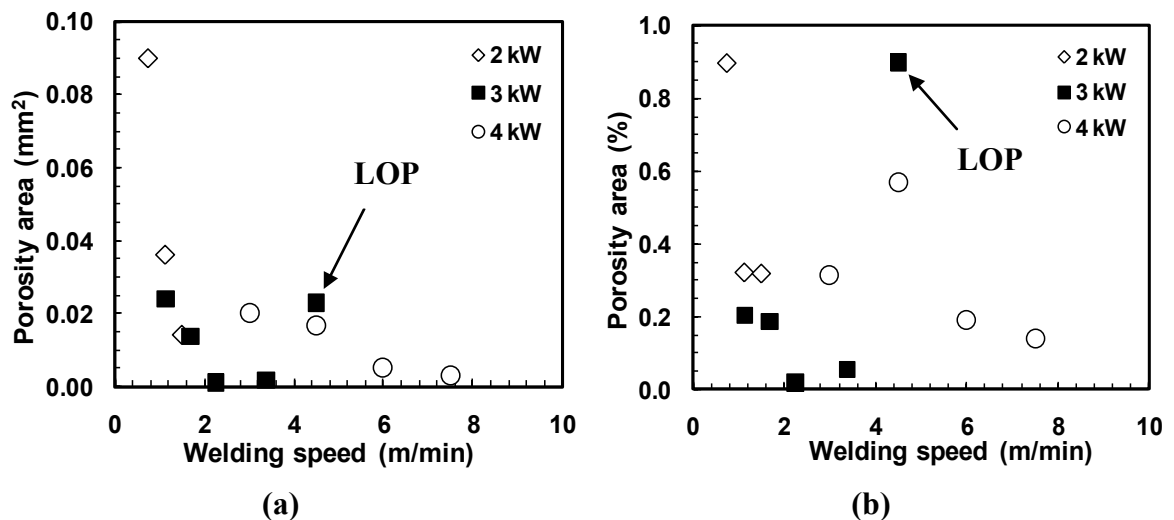


**Figure 4.10- Effect of welding speed on porosity area and percentage of porosity,** It is seen that the porosity area decreases with increasing welding speed. It is found that more porosity is formed at lower welding speed due to longer time available to coalesce.

In particular, there is a significant increase in porosity area at a welding speed of 0.75

m/min indicating that the stability of the keyhole becomes a main concern at welding speed less than 1 m/min.

### 4.3.3 Overlap

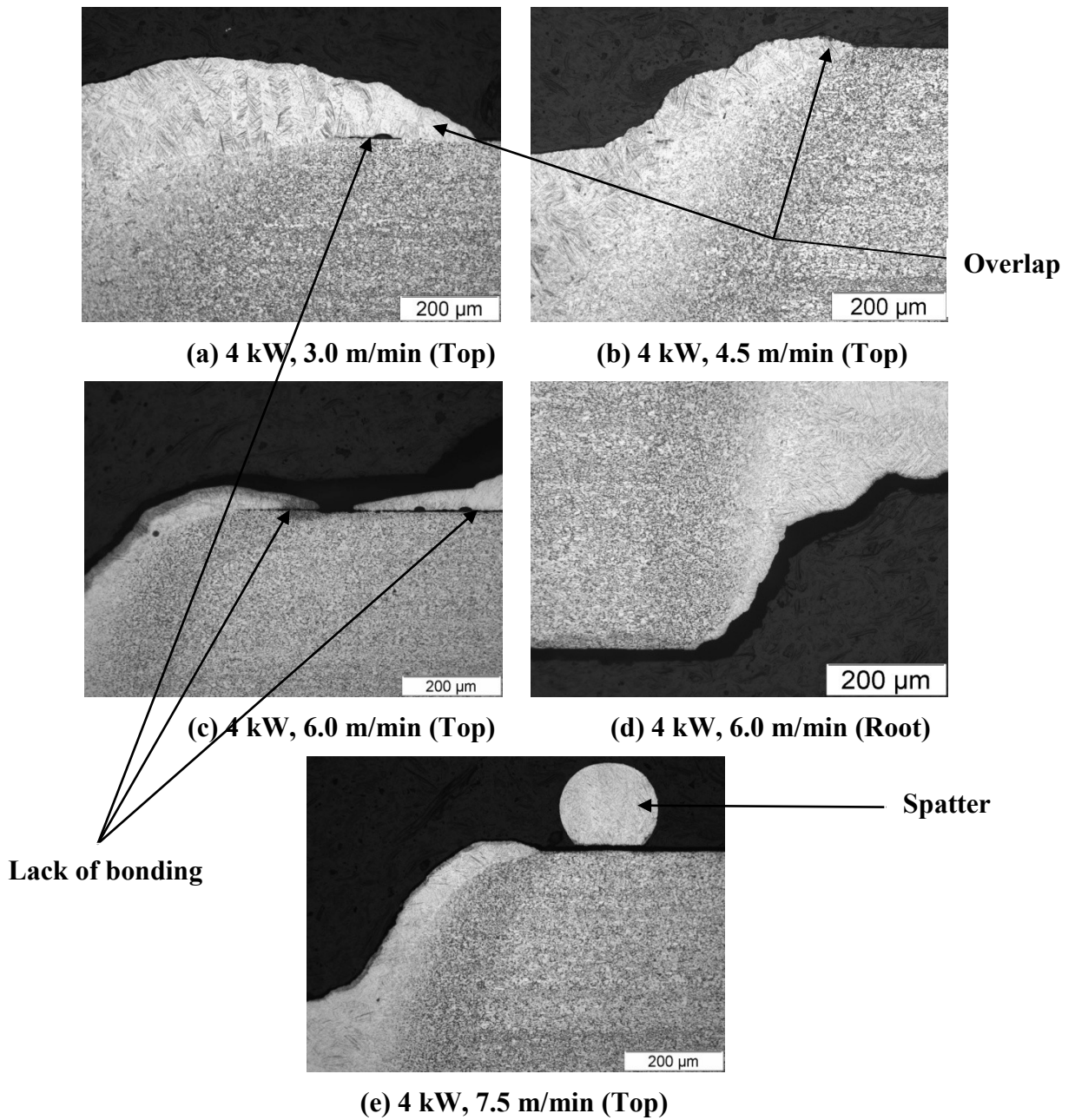


Figure 4.11- Some examples of overlap in welded joints at 4 kW laser power

Typical overlap defects are shown in Figure 4.11. In this study, overlap defects are not observed at 2 and 3 kW laser powers but appear for all the samples welded at a laser power of 4 kW due to higher turbulent flow of the molten metal caused by vapour pressure during the welding. Once again the 4 kW laser power is not recommended for 3.175 mm thick samples. Overlap defect works as a stress concentrator for welded joints and therefore is not desirable.

#### **4.3.4 Other Defects**

As shown in Figure 4.1, centerline grain boundary is frequently observed through the joint thickness. Saggings are observed in the samples mainly welded at high speed (i.e. high cooling rate). In Figure 4.1.1, samples T 115, T 113 and T 67 show the sagging defects.

#### **4.4 Micro-Indentation Hardness**

Figure 4.12 shows a typical distribution of micro-indentation hardness values taken at the top, middle and root regions of a weld joint. It is seen that the base material shows the lowest hardness and the fusion zone shows the maximum values. The reason for the highest hardness in the FZ is the presence of  $\alpha'$  martensite. The hardness gradually decreases in the HAZ with the decreasing amount of  $\alpha'$  martensite from the near HAZ to the far HAZ and then to the BM. The hardness of the near HAZ is almost similar to that in the FZ because the two regions have almost the same martensitic structure. The base material has an average hardness of approximately  $323 \pm 5$  HV 500 gf and FZ has an average hardness of  $368 \pm 10$ ,  $367 \pm 9$  and  $421 \pm 10$  HV for the 2, 3 and 4 kW laser power respectively, indicating 13.9%, 13.62% and 30.34% increment of the average

hardness. The FZ and HAZ widths are different in the top, middle and root areas of the weld. The vertical lines in Figure 4.1.12 indicate the different regions, mainly determined from the middle widths of the FZ and HAZ.

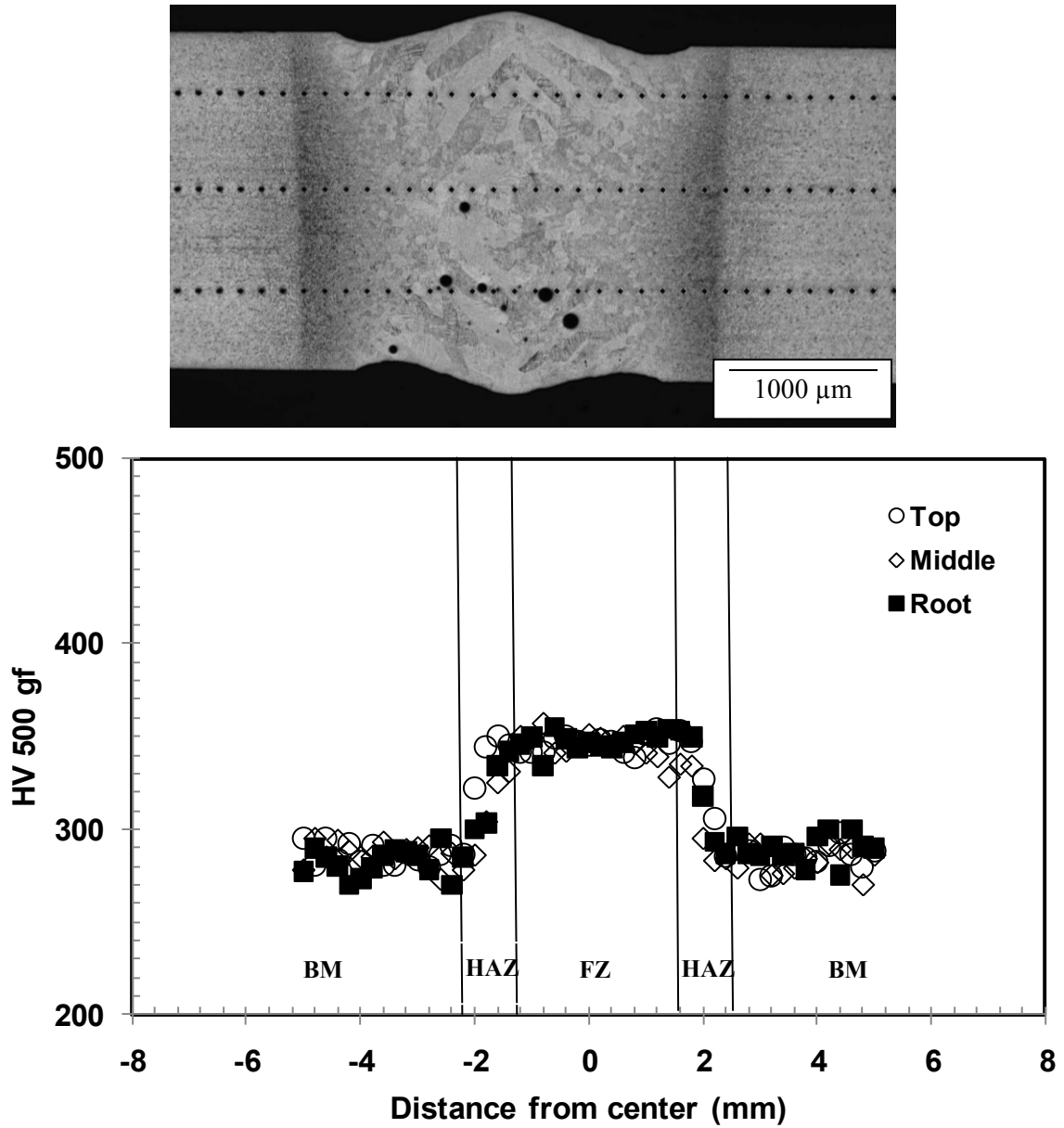
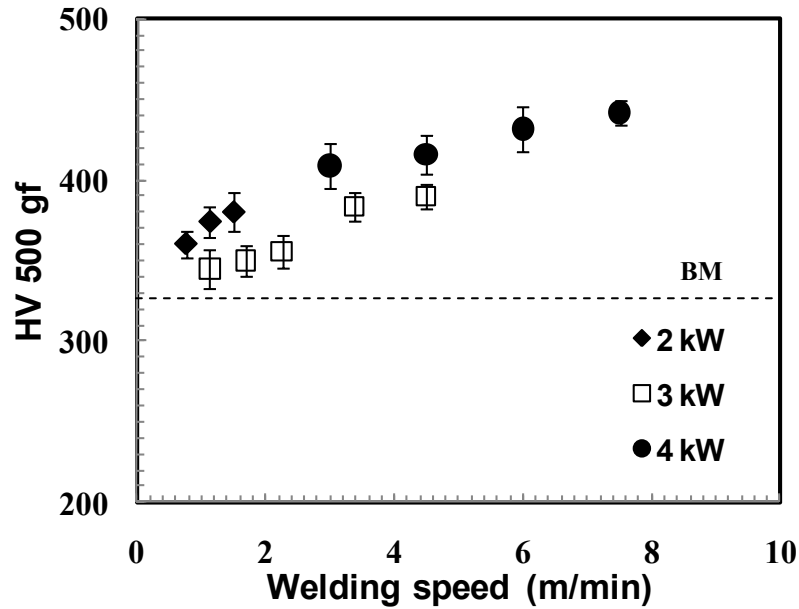


Figure 4.12- Typical hardness distribution profile (3 kW and 1.69 m/min)



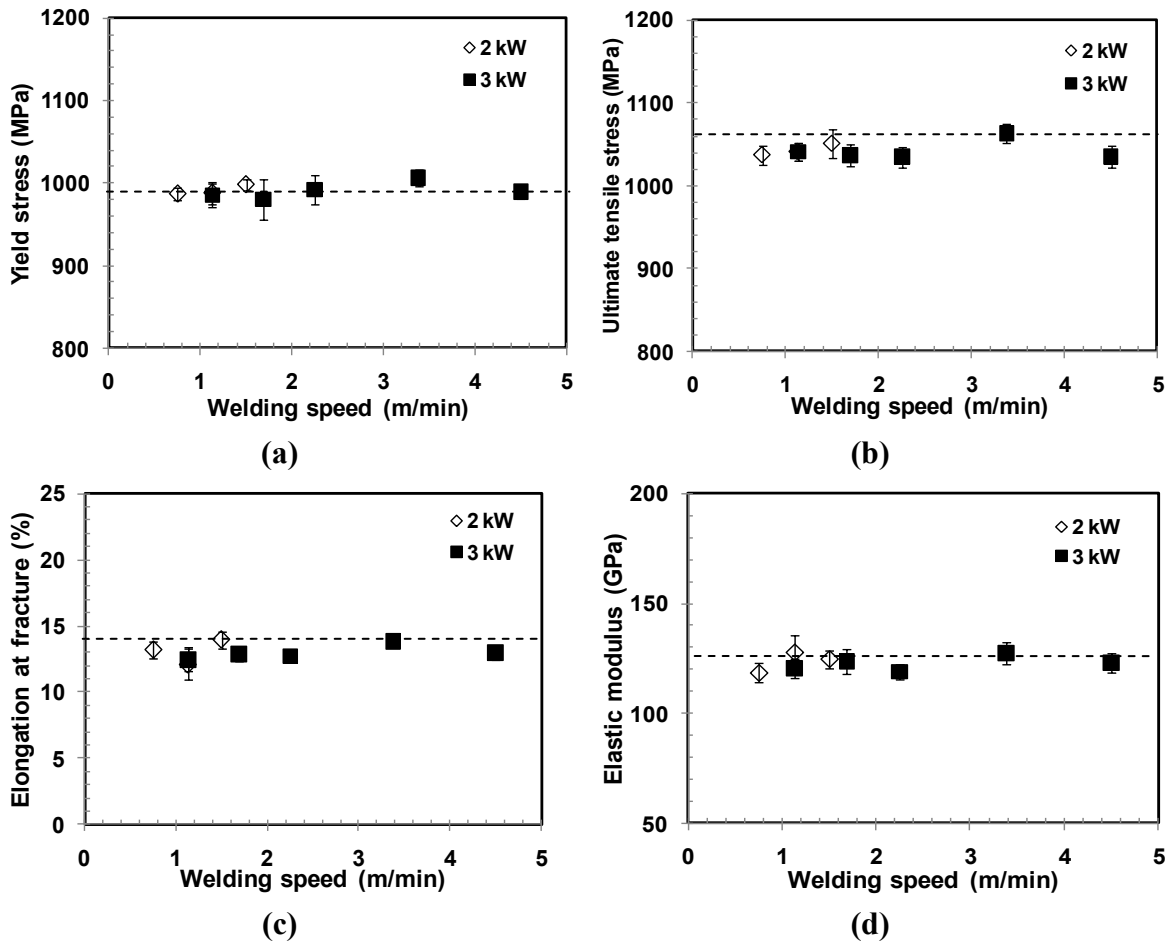
**Figure 4.13- Effect of welding speed on FZ hardness for 3 laser powers**

Figure 4.13 shows the effect of welding speed on average FZ hardness for different laser powers. Dashed line in the diagram indicates the average BM hardness for all the samples. The FZ average hardness increases with increasing welding speed because the higher welding speed is associated with higher cooling rate. Higher cooling rate produces finer martensite [82] and finer prior- $\beta$  grains [69] which mainly increase the FZ hardness.

#### **4.5 Global Tensile Properties**

Tensile samples for 4 kW laser power are not prepared for the mechanical property testing as they already failed to meet the criteria of high quality welds in terms of the geometry and defects. The sample welded at laser power of 3 kW and welding speed of 4.5 m/min shows a lack of penetration. This sample has been welded again from the other side (root side) using the same parameters. Figure 4.14 shows the relationship between welding speed and global tensile properties for 2 and 3 kW laser powers. Four tensile

samples are prepared from each joint. Two of them are tested by digital image correlation (DIC) technique and the other two by conventional MTS machine. The tensile properties obtained from the two testing methods are quite similar indicating the testing methods used are reliable. No significant differences are observed in the global tensile properties for different welding speeds and laser powers. This is an agreement with the results reported by Mazumder and Steen [49]. Dashed lines in the figures indicate the associated base metal values.



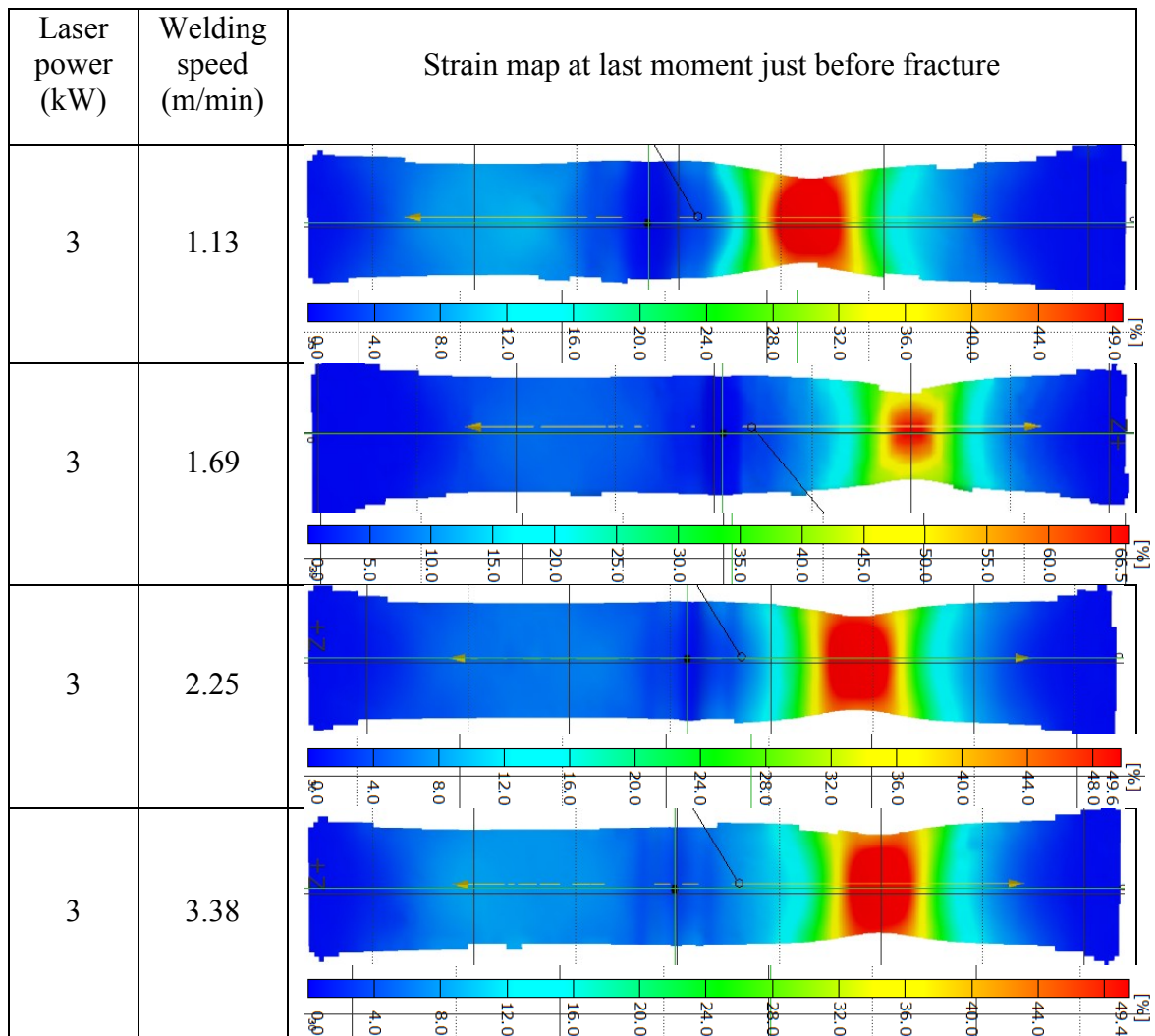
**Figure 4.14- Effect of welding speed on global tensile properties at 2 and 3 kW laser powers**

All the 32 samples failed in the BM indicating stronger FZ due to the presence of  $\alpha'$  martensite. The average joint efficiency has been calculated as 98.1% ranging from a minimum of 97.45% to a maximum of 100%. The joint efficiency is defined as the ratio of the tensile strength of the welded joint to that of base metal. The BM tensile properties are taken from Cao *et al.* [48] for Ti-6Al-4V from the same source. Cao *et al.* [48] reported that the BM yield stress is 996 MPa, ultimate tensile stress is 1062 MPa, and elongation at fracture is 14%.

#### **4.6 Local Tensile Properties**

With the digital image correlation (DIC) technique using the ARAMIS system, it is possible to capture digital images of different stages during deformation of the tensile testing from beginning to the failure. Weld being a composite of three different zones with different microstructures, it is expected that these three different zones show different mechanical properties. The differences in micro-indentation hardness are already discussed in Section 4.4. Figure 4.15 shows the digital images at the last moment just before the fracture for each sample. The different colors indicate different strains prior to failure. It is now possible to create any size and any number of gage lengths on the images from where it is possible to determine stress-strain diagrams for a selected gage length. An iso-stress condition is assumed for all the samples. In iso-stress condition, the global stress is considered as the corresponding local stress in any position of the sample within the gage length. Local strain data can be extracted from the ARAMIS system and plotted against the corresponding global stress data to produce the stress-strain response for virtually any position within the displacement data field. Iso-stress condition has been used by many researchers to determine the local tensile

properties so far [70, 71, 79]. Once the stress-strain diagram is revealed, it is possible to determine the elastic modulus, yield stress, ultimate tensile stress, and elongation at fracture and so on. It is obvious from the digital images that the strain concentration is maximum in the base metal indicating that the BM is the weakest region. In spite of the presence of underfill and porosity, the strain localization is minimum in the FZ where the  $\alpha'$  martensite microstructure is strong but less ductile. Therefore, it is clear that underfill and porosity do not have significant effect on the mechanical properties of the Ti laser welds.



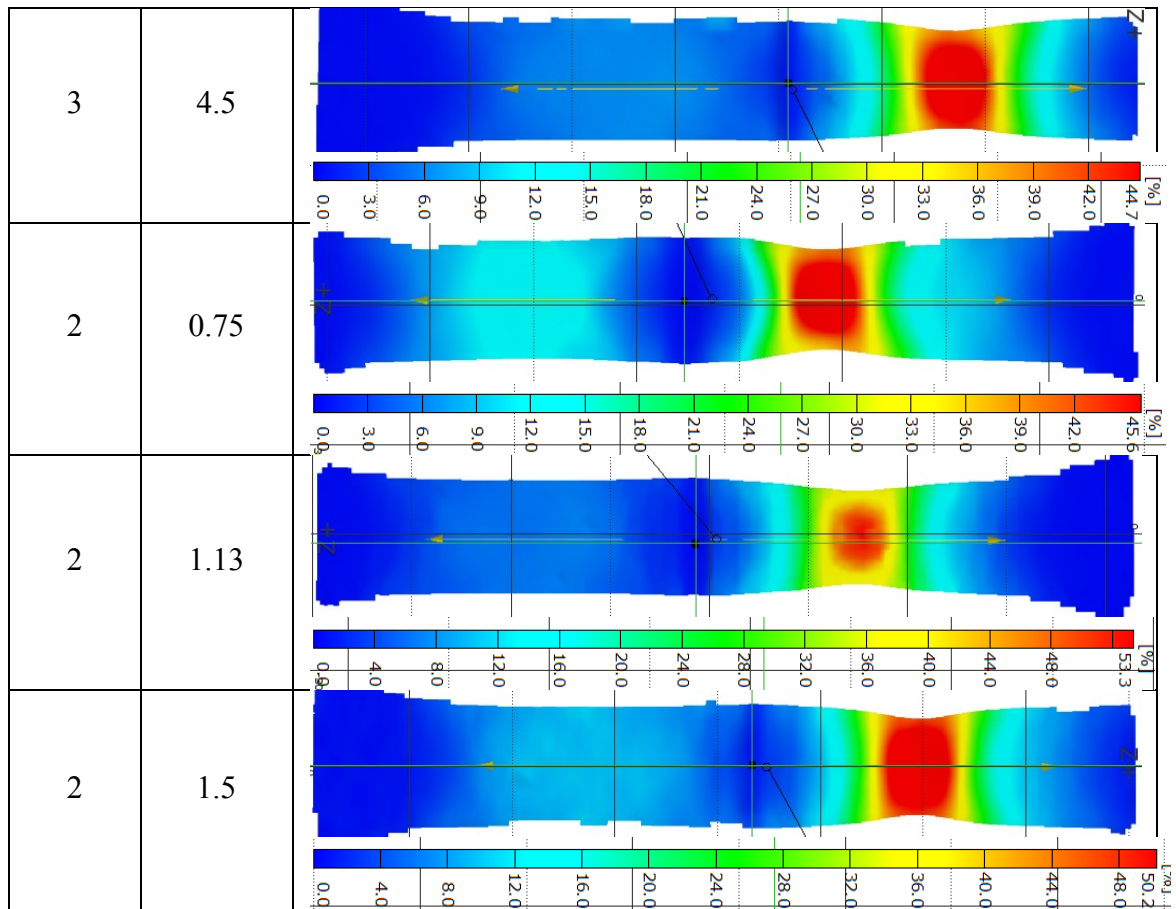


**Figure 4.15- Digital images of the last moment just before failure**

It is now well established that the elastic modulus of Ti-6Al-4V alloy changes with heat treatment, deformation, and microstructure unlike most of other metals and alloys [83-86]. The change in elastic modulus has been determined by Lee *et al.* [83] as shown in Figure 4.16a. The figure shows that the elastic modulus is the lowest at the quenching temperature of 800°C which is close to the quenching temperature of heat affected zone roughly reported as 720 to 985°C by Cao *et al.* [47]. It has been also reported that the elastic modulus is maximum when Ti-6Al-4V is quenched from 1200°C which is much less than the fusion zone temperature in laser welding. In a laser weld, the pool temperature was reported to be ~3000°C by Khan and Debroy [87], about 1350°C higher than the liquidus temperature (~1650°C) of Ti-6Al-4V. The FZ has a martensite structure

and hence its elastic modulus should be similar to that obtained from the quenched Ti-6Al-4V alloy. The yield stress has been also reported to be minimum at the quenching temperature of 800°C and maximum at quenching temperature of 1200°C as shown in Figure 4.16b [83]. Hence it is expected to obtain the minimum elastic modulus and yield stress in the HAZ and the maximum in the FZ.

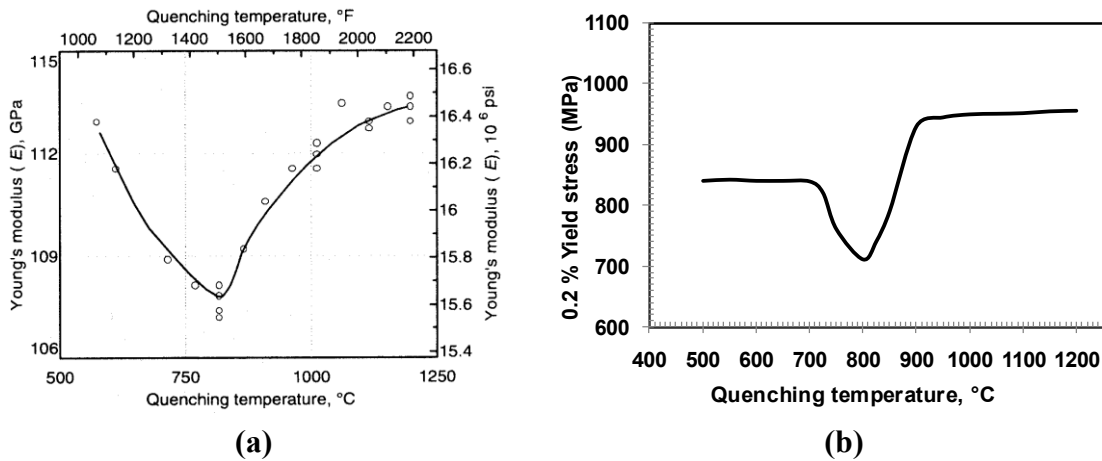


**Figure 4.16- Variation of elastic modulus [86] and yield stress [83] of Ti-6Al-4V alloy with quenching temperature**

Figure 4.17 shows the representative trends in local tensile properties. Elastic modulus is around 200 GPa in the FZ and in the range of a 130-140 GPa in the BM indicating about 42-53% increase in the FZ. This may be due to the presence of very fine martensite in the FZ cooled from a temperature  $\sim 3000^{\circ}\text{C}$  during the laser welding. The elastic modulus is minimum in the HAZ. Yield stress is slightly higher in the FZ than in the BM and the minimum is in the HAZ which also supports the results from the literature [83]. Sometimes the stress in the FZ does not reach up to the yield prior to failure. Thus, the FZ deforms elastically at the fracture (indicated by a break line in Figure 4.17d) and the localized maximum plastic strain at fracture at this point is zero (Figure 4.17f). The yield stress of the BM found by DIC technique is almost the same as reported by Cao *et al.* [48]. This proves the reliability of the DIC technique in the determination of local tensile

properties. Localized plastic strain is the maximum at the area of fracture. FZ shows the minimum localized plastic strain due to the less ductile and harder martensite.

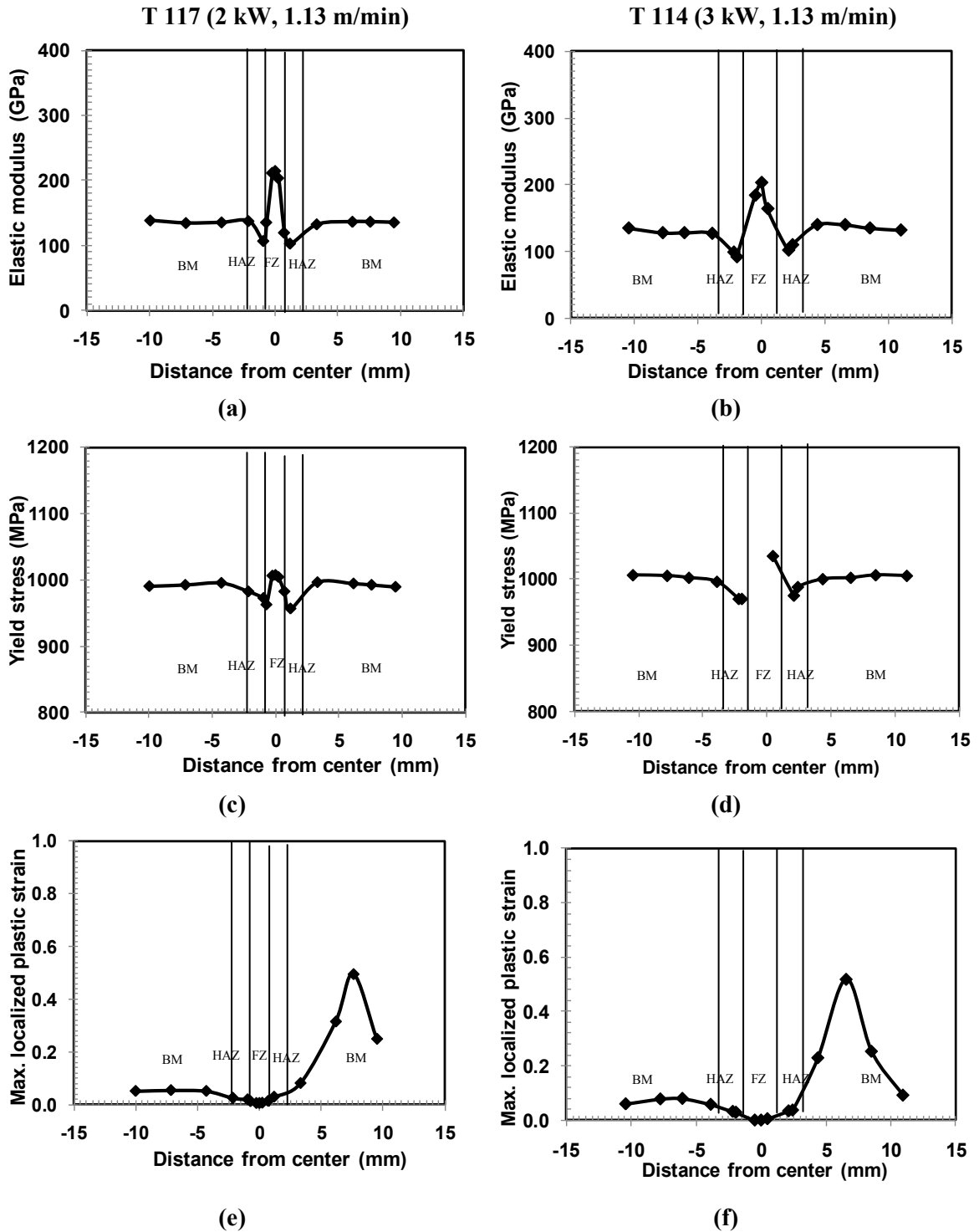
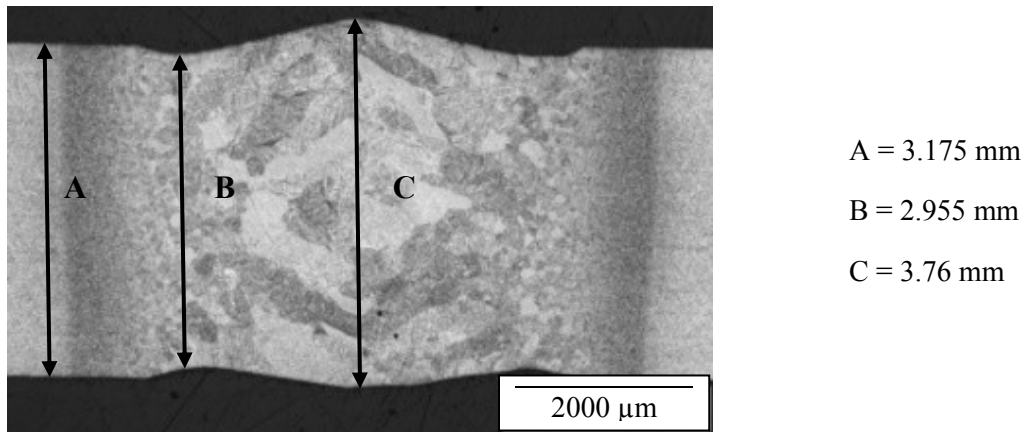


Figure 4.17- Local tensile properties for sample T 117 (2 kW, 1.13 m/min) and T 114 (3 kW, 1.13 m/min)

Simplification of the iso-stress condition is a limitation of this work. The samples are tested in the as-welded condition (not machined to a flat surface). It is obvious that the thickness throughout the whole weld is not the same. For example, Figure 4.18 shows the difference among the thicknesses of a sample in the BM (A), near HAZ with underfill (B) and with reinforcements (C). Then the stresses with corresponding areas have been calculated rather than considering an iso-stress condition.



**Figure 4.18- True thicknesses of the sample ( 3 kW, 1.13 m/min) at different positions**

It is found that the elastic modulus in the middle of the FZ drops down to 174 GPa if we consider the actual cross sectional area instead of 203 GPa found in iso-stress condition. Similarly the elastic modulus of the underfill/ HAZ area is found to be 109 GPa instead of 91 GPa in iso-stress condition. The base metal elastic modulus varies from 130 to 140 GPa. It should also be noted that the DIC technique for local tensile property measurement assumes the material in a stress-free condition [70]. However, residual stress is more or less built due to non-equilibrium cooling during the laser welding. This is also a limitation of the DIC technique which can be a significant source of error during the local tensile property measurement of the FZ and HAZ.

Besides, it is very difficult to select a gage length over the HAZ area as it always includes part of either FZ or BM due to its hourglass shape (Figure 4.19). Therefore, the local properties of HAZ are very tricky to calculate and there will always exist some error in the measurement.

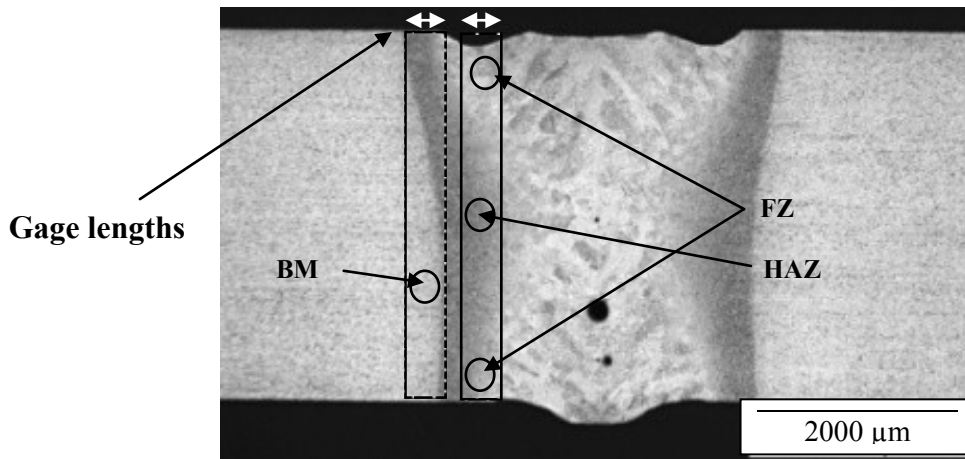
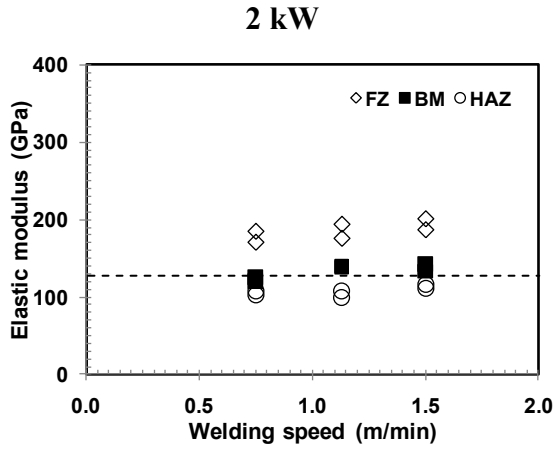
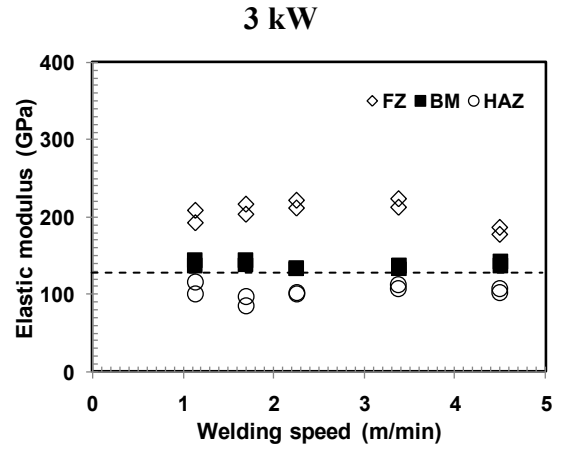


**Figure 4.19- Determination of local properties of HAZ**

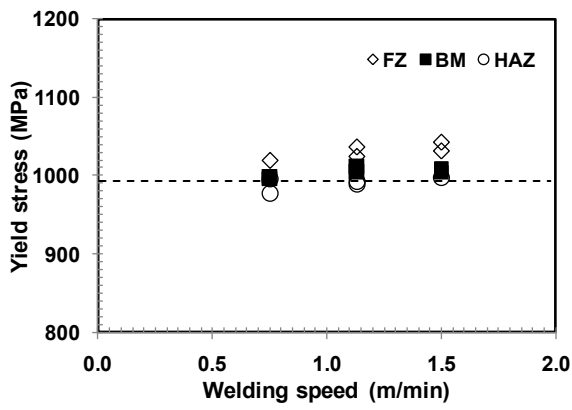
Figure 4.20 shows the variation of local tensile properties with the welding speed for 2 and 3 kW laser powers, respectively. Dashed line on the figures indicates the corresponding BM value reported by Cao *et al.* [48]. Elastic modulus seems to increase slightly with increasing welding speed for fully penetrated joints for both the laser powers (Figures 4.20a & b). Yield stress also increases slightly with increasing welding speed (Figures 4.20c & d). This is due to the finer martensite and prior- $\beta$  grain size associated with the increasing welding speed. Due to the significant grain refinement at higher welding speed, the localized plastic strain at fracture also increases slightly with increasing welding speed (Figures 4.20e & f). The elastic modulus and yield stress of the BM are very close to the reported values of Cao *et al.* [48].



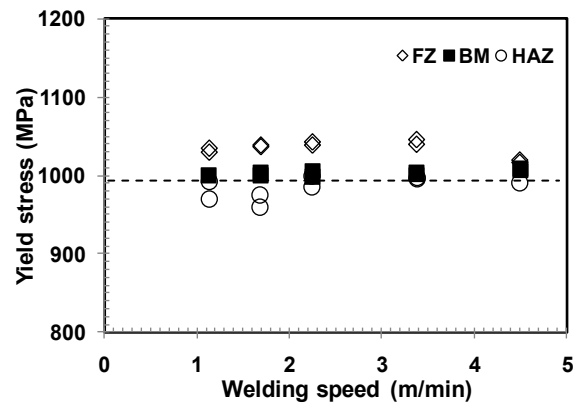
(a)



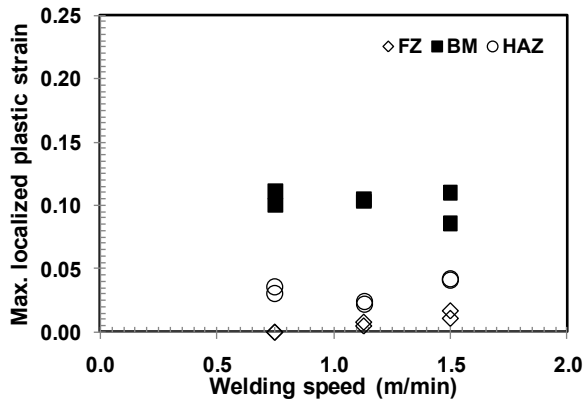
(b)



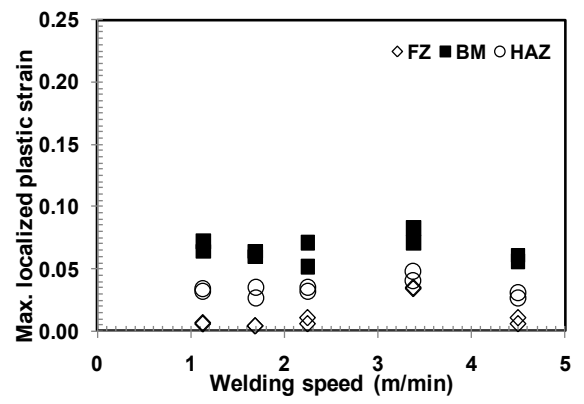
(c)



(d)



(e)



(f)

Figure 4.20- Local tensile properties for 2.0 kW and 3.0 kW laser powers

## 4.7 Fractography

Figure 4.21 shows the SEM fracture surface of the tensile tested samples. Fractures took place in a cup and cone style with dimple structures indicating ductile fracture.

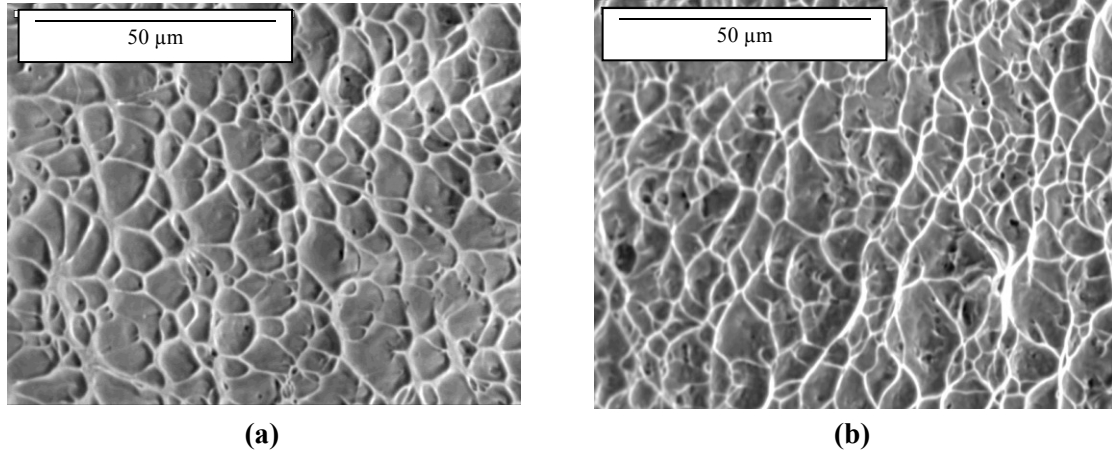


**Figure 4.21- SEM fracture surface of the samples (a) 2 kW, 1.13 m/min, (b) 3 kW, 1.13 m/min**

## 4.8 Operating Window

Figure 4.22 shows the operating window drawn from the results obtained for the laser welding of 3.175 mm thick Ti-6Al-4V alloy.

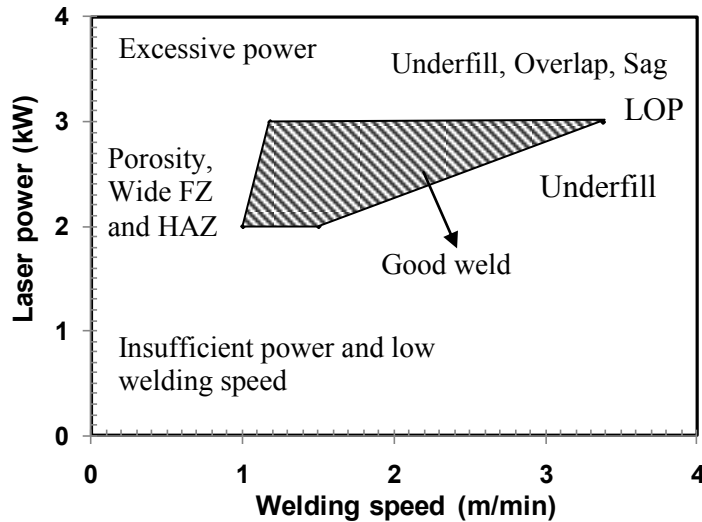


**Figure 4.22- Operating window for the laser welding of 3.175 mm Ti-6Al-4V alloy**

## Chapter 5/ Effect of Welding Speed and Defocusing Distance

---

The effect of welding speed and defocusing distance on the weldability of 5.08 mm thick sheets has been investigated at a laser power of 4 kW and at defocusing distances of -1 mm and -2 mm. Table 5.1 shows the process parameters used in this part of the study.

**Table 5.1: Key experiments / effect of welding speed and defocusing distance**

Sample #	Laser power (kW)	Welding speed (m/min)	Defocusing distance (mm)	Notes
T 138	4.0	0.75	-1	
T 137	4.0	1.0	-1	
T 136	4.0	1.5	-1	
T 135	4.0	1.75	-1	NR*
T 140	4.0	1.75	-1	2nd side welding of T 135
T 134	4.0	2.0	-1	LOP
T 139	4.0	2.0	-1	2nd side welding of T 134
T 142	4.0	0.75	-2	
T 141	4.0	1.0	-2	
T 143	4.0	1.5	-2	

\* NR = Narrow Root

### 5.1 Weld Geometry

Figure 5.1 shows the effect of welding speed and defocusing distance on the weld transverse sections. Fully penetrated welds are obtained at welding speeds from 0.75 m/min to 1.75 m/min. It is observed that the FZ width is relatively wide at 0.75 m/min and evolved with increasing welding speed to render a narrow FZ root at 1.75 m/min. At low welding speeds, keyhole instability and collapse contributed to the formation of porosity. At extremely lower welding speeds, the change from keyhole to conduction welding mode may appear and imparts a large weld bead profile with a bead width to

penetration ratio less than 1. In contrast, at a high welding speed of 2.0 m/min, a lack of penetration occurs, as indicated in Figure 5.1h.

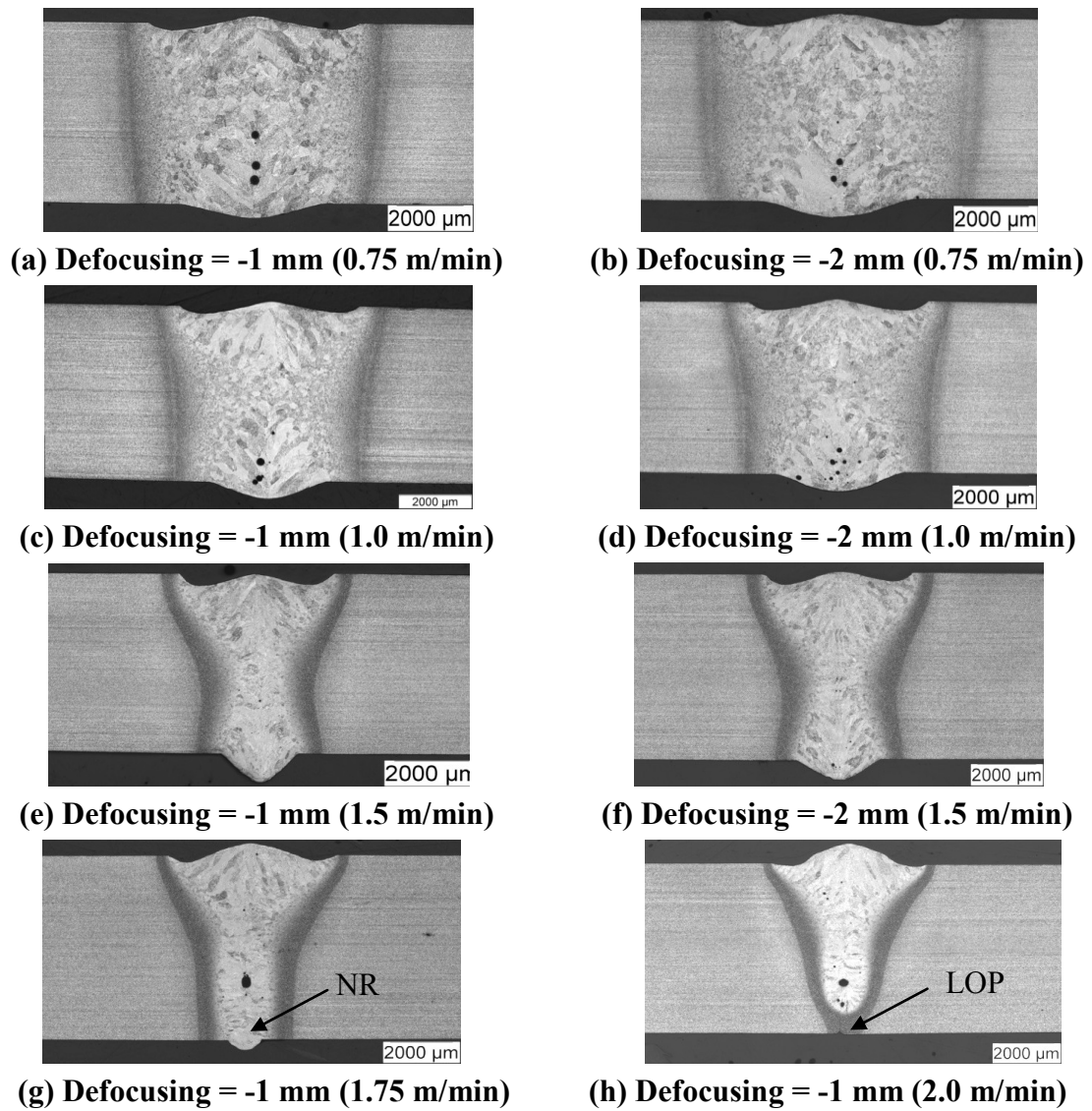


**Figure 5.1- Effect of welding speed and defocusing distance on transverse sections**

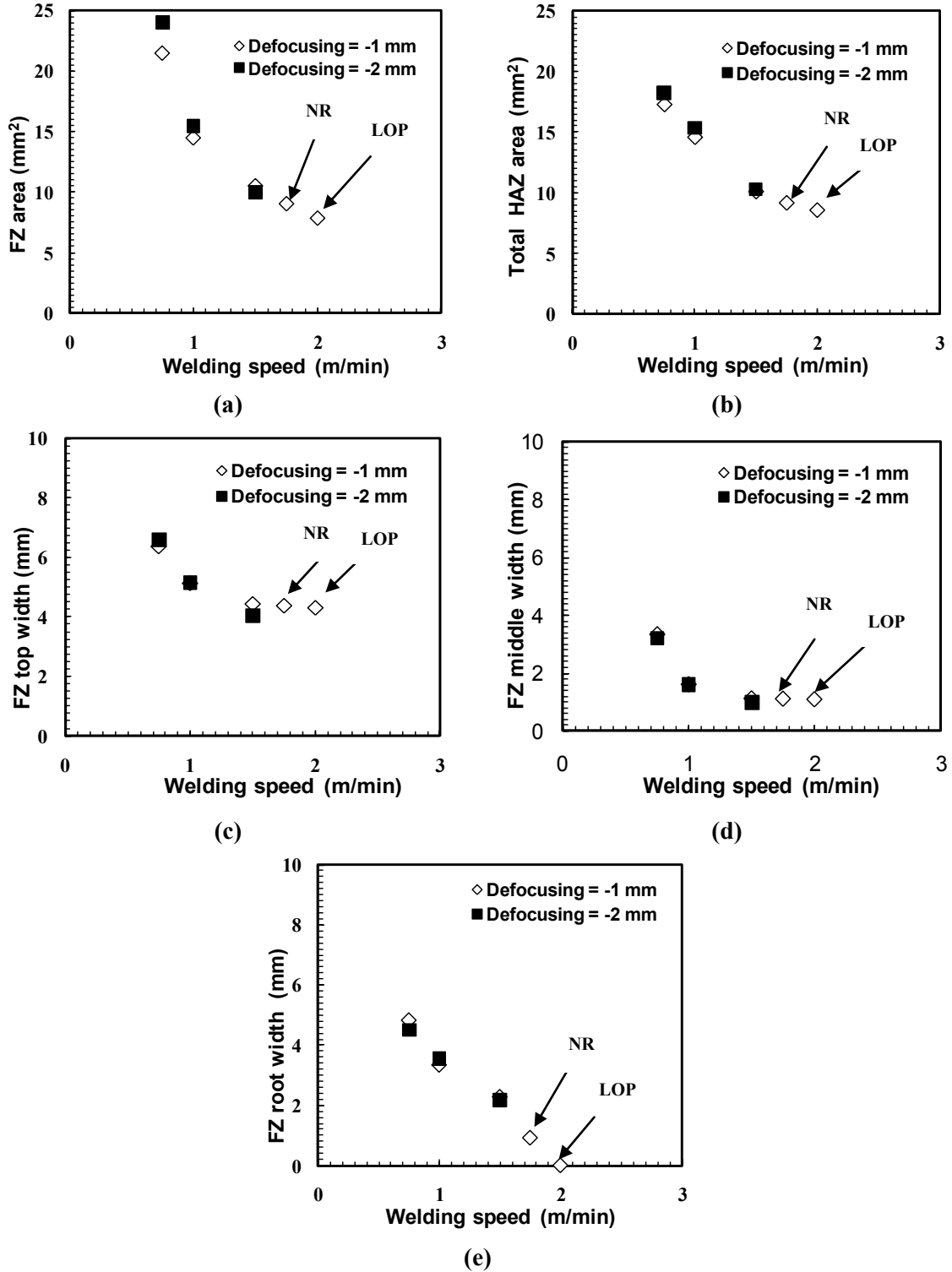
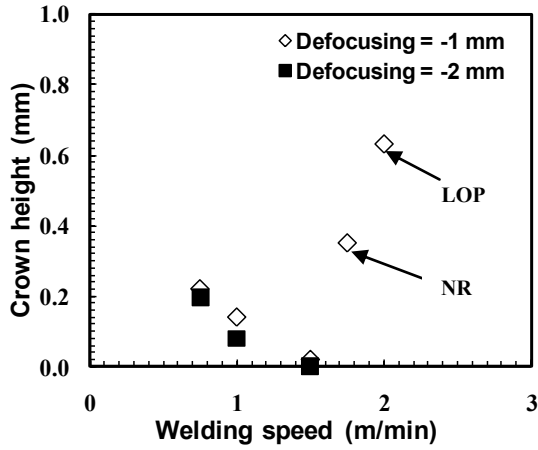
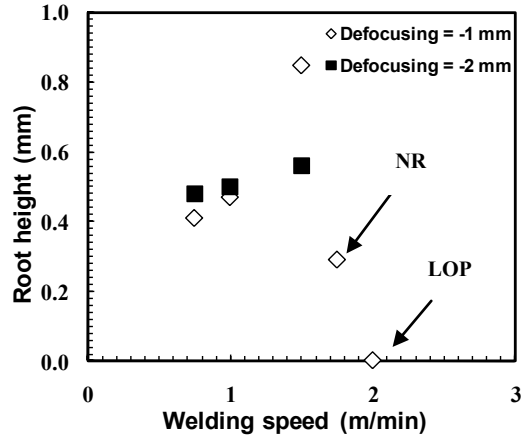


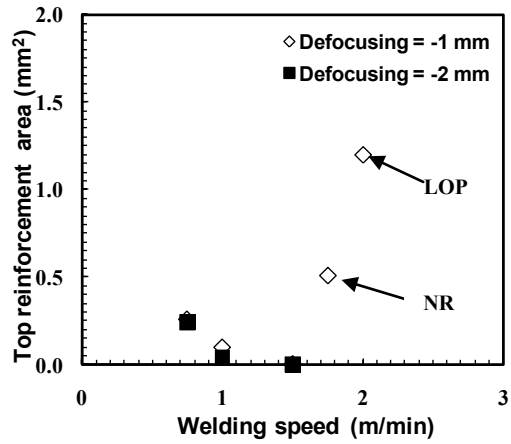
Figure 5.2- Effect of welding speed and defocusing distance on FZ and HAZ dimensions



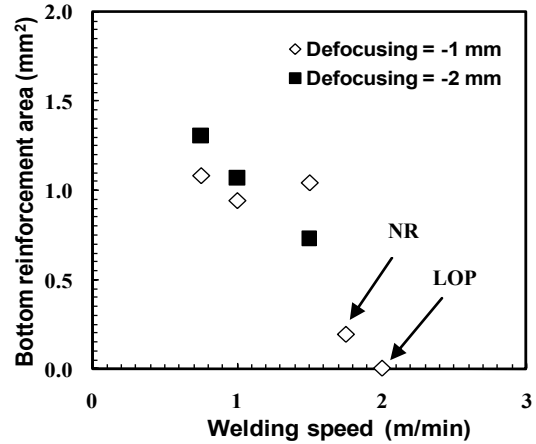
(a)



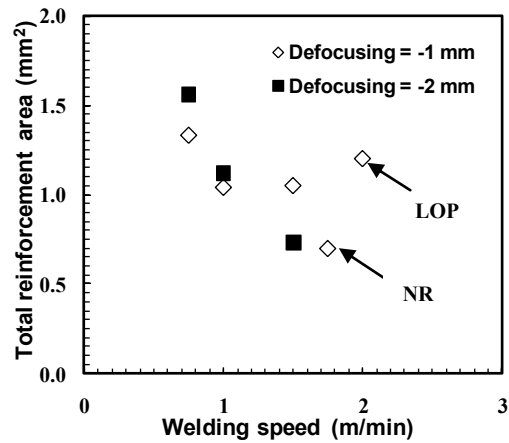
(b)



(c)



(d)



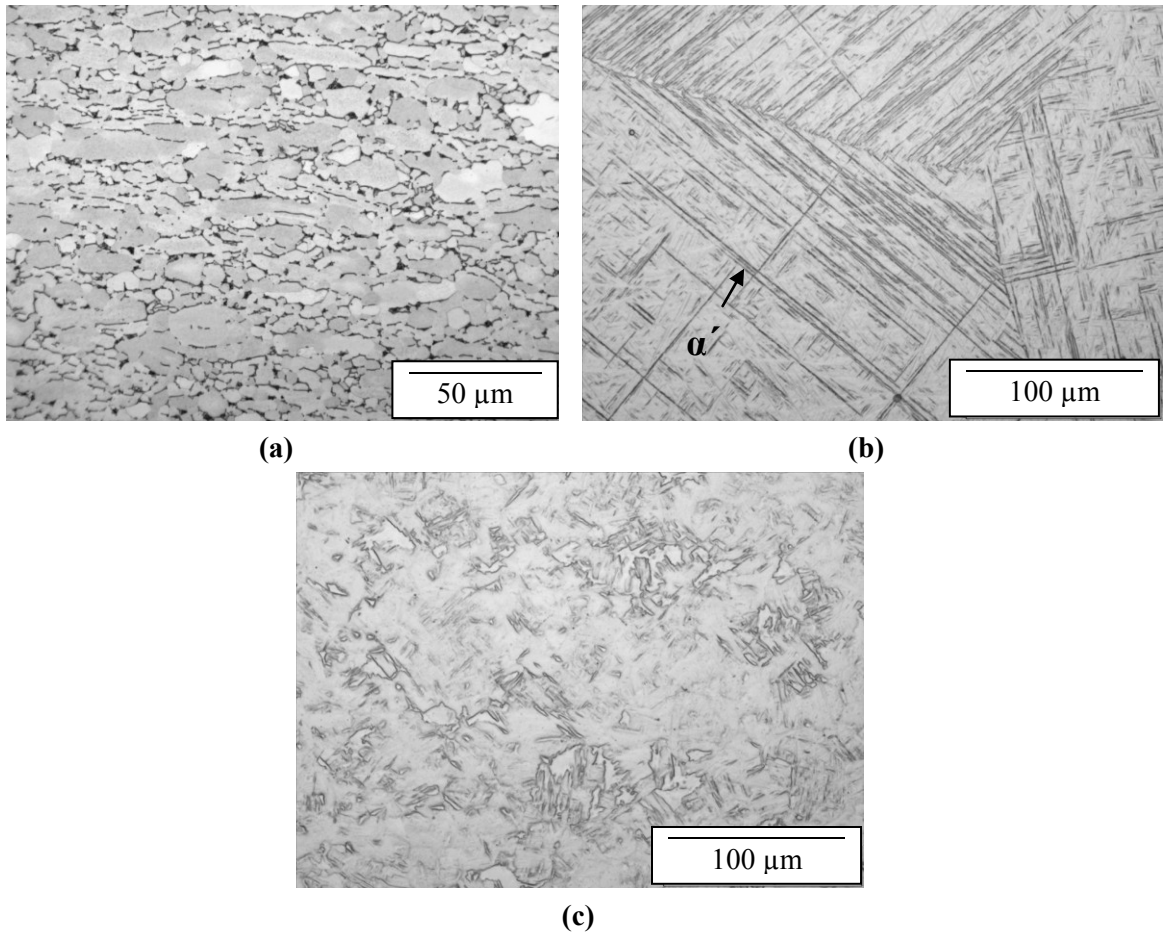
(e)

Figure 5.3- Effect of welding speed and defocusing distance on weld reinforcement

The influence of welding speed and defocusing distance on the weld bead characteristics is shown in Figure 5.2. The areas of the FZ and HAZ as well as the FZ widths at top, middle and root of the welds decrease with increasing welding speed. This is in agreement with the results found with the 3.175 mm thick samples. However, no significant difference in the joint dimensions has been found at the two defocusing distances (-1 and -2 mm). Figure 5.3 shows the effect of welding speed and defocusing distance on weld reinforcement. The crown height, top and root reinforcement areas decrease but root height increases with increasing welding speed. The maximum reinforcement area is obtained at the lowest speed and at a defocusing distance of -2 mm. Samples with NR and LOP have higher crown heights and lower root heights than fully penetrated samples.

## 5.2 Microstructures

Figure 5.4a shows a typical BM structure consisting of slightly elongated equiaxed  $\alpha$  with intergranular  $\beta$ . The FZ microstructure (Figure 5.4b) consists of fully acicular  $\alpha'$  martensite with small amount of  $\beta$ -phase. But the size of the martensite plate is larger than that in the 3.175 mm thick samples. This may be associated with the slower cooling rate. For 3.175 mm thick samples, cooling rate is clearly higher than 5.08 mm thick samples. The HAZ microstructure shows a mixture of both the BM and FZ structures, i.e. it contains the equiaxed  $\alpha$  with intergranular  $\beta$  and some smaller size  $\alpha'$  martensite (Figure 5.4c).



**Figure 5.4- Typical microstructures of (a) BM (b) FZ (c) Middle HAZ**

## **5.3 Defects**

### **5.3.1 Underfill**

Underfill defects are observed in almost all fully penetrated joints. The effects of welding speed and defocusing distance on underfill defects are shown in Figure 5.5. Both the underfill depth and area increase with increasing welding speed up to a certain limit (1.5 m/min) and then decrease with further increase in the welding speed. The occurrence of a maximum underfill depth and area at an intermediate welding speed (1.5 m/min) can be reasoned on the basis of the combined effects of the evaporation/spatter of the molten

weld pool and liquid metal flow, those are dominant at low and high welding speeds, respectively. Samples with narrow root and lack of penetration have less underfill defect than fully penetrated samples.

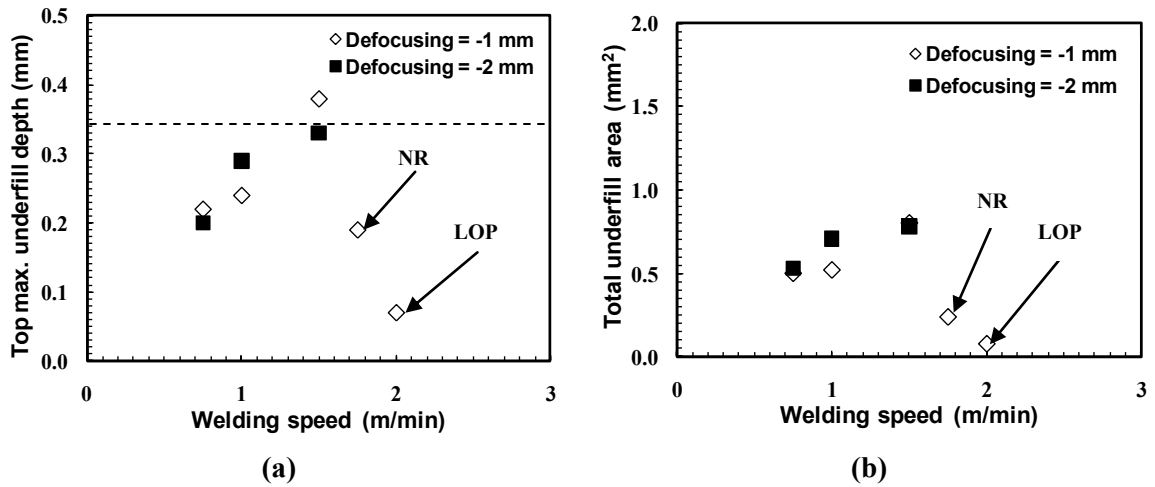
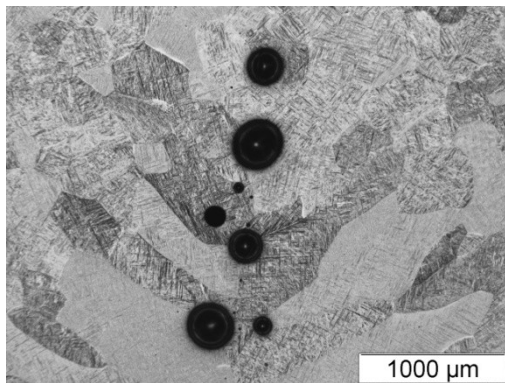


**Figure 5.5- Effect of welding speed and defocusing distances on underfill**

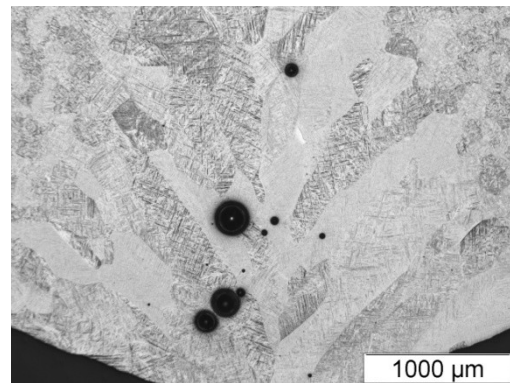
According to AWS D17.1 [81], the specification for fusion welding for aerospace applications stipulates a maximum underfill depth of  $0.07t$  (where  $t$  is the thickness or 5.08 mm in this part of work) for Class A welds. Hence, over the range of welding conditions examined, the autogenous laser welds in Ti-6Al-4V satisfy Class A requirements in that the underfill discontinuity remained below 0.36 mm ( $0.07 * 5.08$  mm), as indicated by the dashed line in Figure 5.5a, for all welds with the exception of the specimen T 136 (1.5 m/min and -1 mm defocusing distance) that is close to the borderline.

### 5.3.2 Porosity

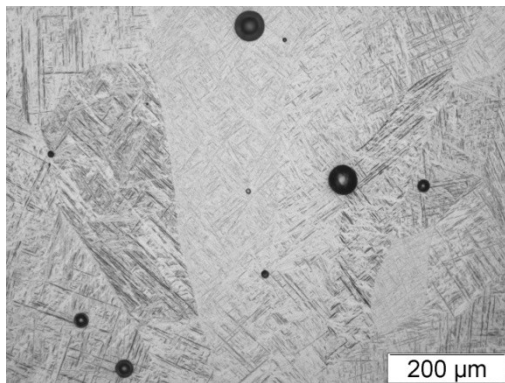
Porosity is frequently observed in the fusion zone of 5.08 mm thick samples. They are mainly located in the centerline and near the HAZ/FZ boundaries. Randomly distributed porosity can also be observed. Most of the porosity is found in the lower half of the fusion zone especially at lower welding speeds due to the unstable keyhole. Figure 5.6 shows some typical examples of porosity observed in the 5.08 mm thick samples.



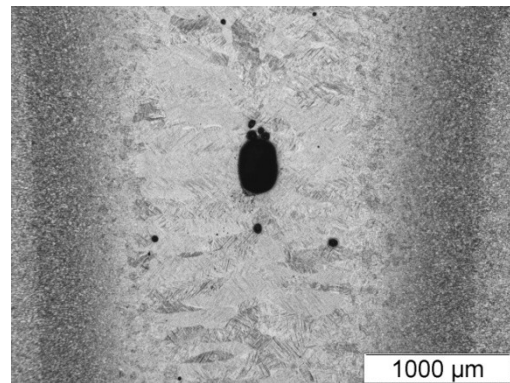
**(a) Defocusing -1 mm, 0.75 m/min**



**(b) Defocusing -1 mm, 1.0 m/min**



**(c) Defocusing -1 mm, 1.5 m/min**



**(d) Defocusing -1 mm, 1.75 m/min**

**Figure 5.6- Some examples of typical porosities**

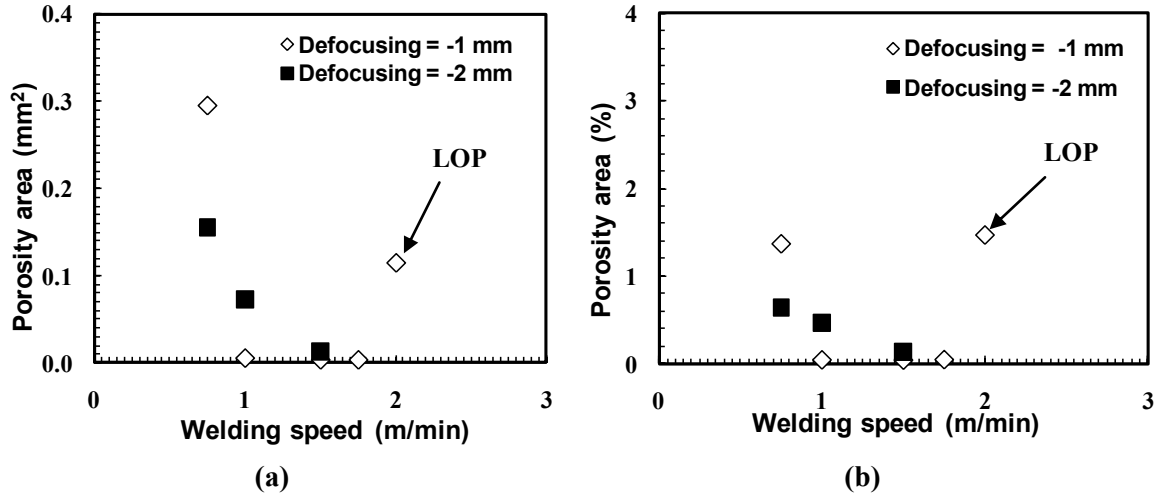


**Figure 5.7- Effect of welding speed on porosity area and percentage of porosity at 2 defocusing distances**

Excluding the weld with LOP defect, the general trend is that porosity area decreases with increasing welding speed, as indicated in Figure 5.7. More porosity is formed at lower welding speed, probably due to longer time available for the growth. It is well known that the welds without full penetration have higher amount of porosity. Higher porosity obtained at welding speed less than 1 m/min indicates that the stability of keyhole is one of the main concerns for porosity formation. As the porosity area is very high when the welding speed is less than 1 m/min, the optimum welding speed should be  $\geq 1$  m/min. For the two defocusing conditions studied in this work, it is found that the overall percent porosity area remains below 2% for welding speed between 0.75 – 2.0 m/min as shown in Figure 5.7b.

#### 5.4 Micro-Indentation Hardness

Figure 5.8 shows the typical hardness profiles of a sample welded at 4 kW laser power, 1.5 m/min speed and -1 mm defocusing distance. The microhardness behaviour evolves from the lowest values in base metal ( $313 \pm 8$  HV) to the highest values in the FZ ( $361 \pm$

10 HV) of the Ti-6Al-4V weldments. The maximum hardness in the FZ (~15 % increase relative to base metal) is related to the presence of  $\alpha'$ , which exhibits high strength and hardness but at the expense of ductility and toughness. The hardness significantly decreases in the HAZ with the decrease in the amount of  $\alpha'$  from the near HAZ to the far HAZ. The hardness in the near HAZ remains practically similar to that in the FZ due to the dominating presence of the  $\alpha'$  phase in the microstructure. Figure 5.9 indicates the effect of welding speed on the FZ average hardness. It is found that the average hardness has a trend to increase with increasing welding speed. This is related to the decrease in heat input. At higher welding speed, the higher cooling rate after welding results in the formation of more refined  $\alpha'$  and prior- $\beta$  grains.

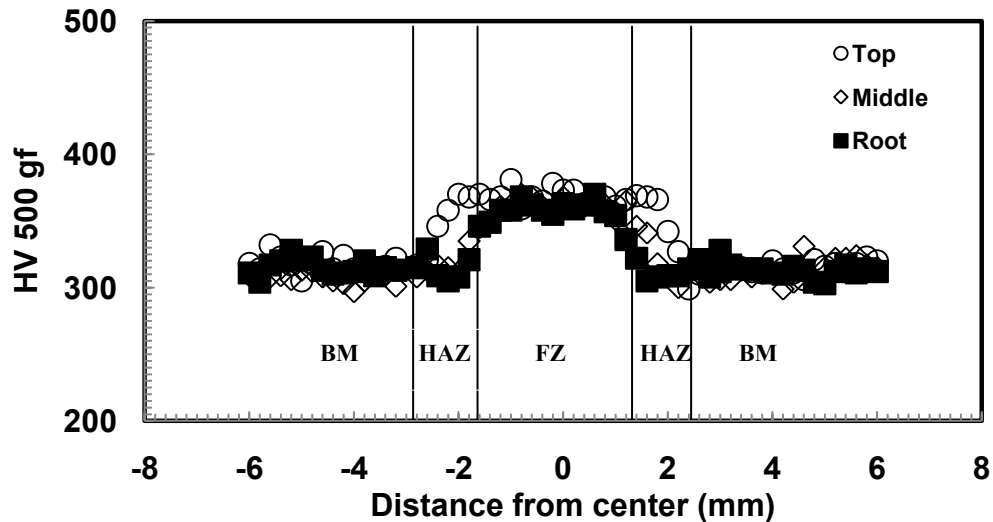


Figure 5.8- A typical hardness distribution profile (4 kW, 1.5 m/min, -1 mm)

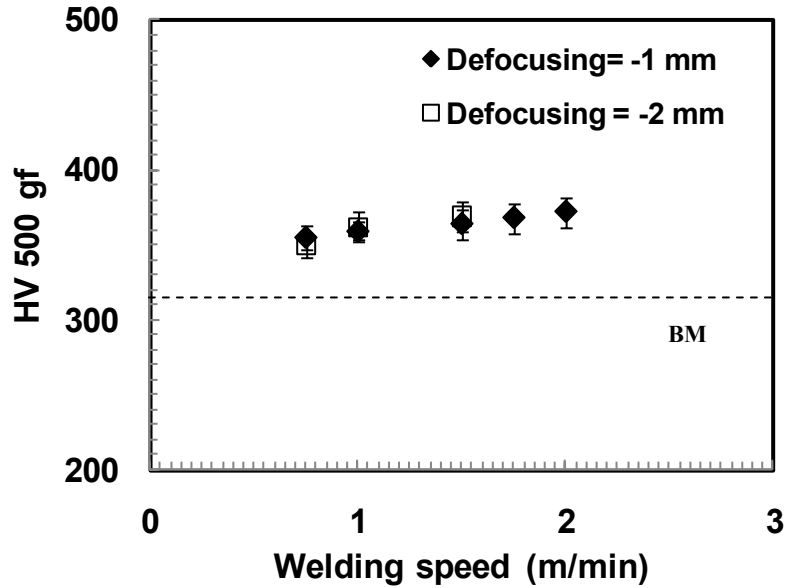
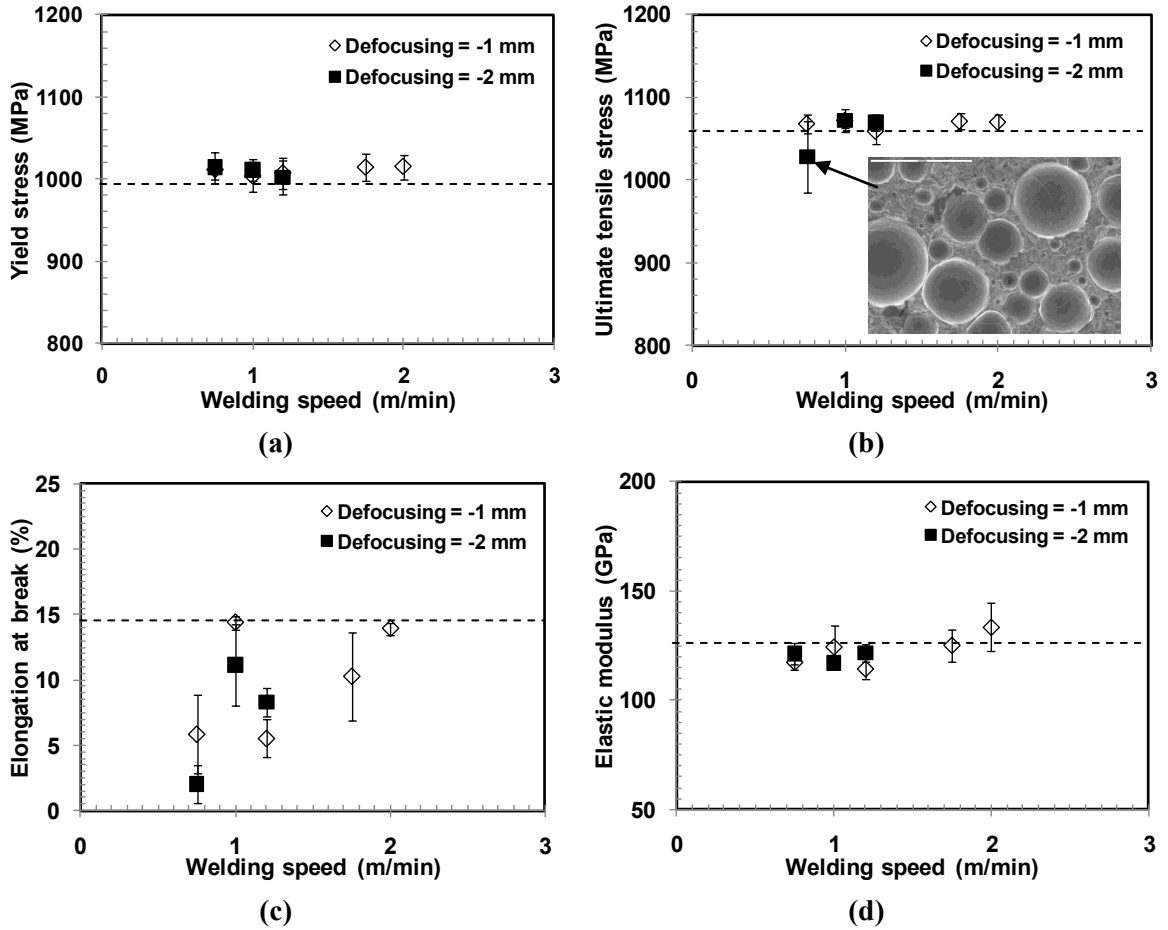


Figure 5.9- Effect of welding speed on FZ average hardness

### 5.5 Global Tensile Properties

Four tensile samples have been prepared from each joint. Two of them are tested by digital image correlation (DIC) technique and the other two by conventional MTS machine. The samples welded at defocusing -1 mm and welding speeds of 1.75 and 2.0 m/min showed narrow root and lack of penetration, respectively. These samples have been welded again from the other side (root side) using the same parameters. Figure 5.10 shows the effect of welding speed and defocusing distance on the global tensile properties. Yield stress and ultimate tensile stress remain almost constant for all the welding speeds and defocusing distances except the sample welded at welding speed of 0.75 m/min and defocusing distance of -2 mm. The elongation at break is also the lowest for this sample. The reason for this is the presence of a cluster of porosities in the FZ as observed at the fracture surface by scanning electron microscope (Figure 5.10b).



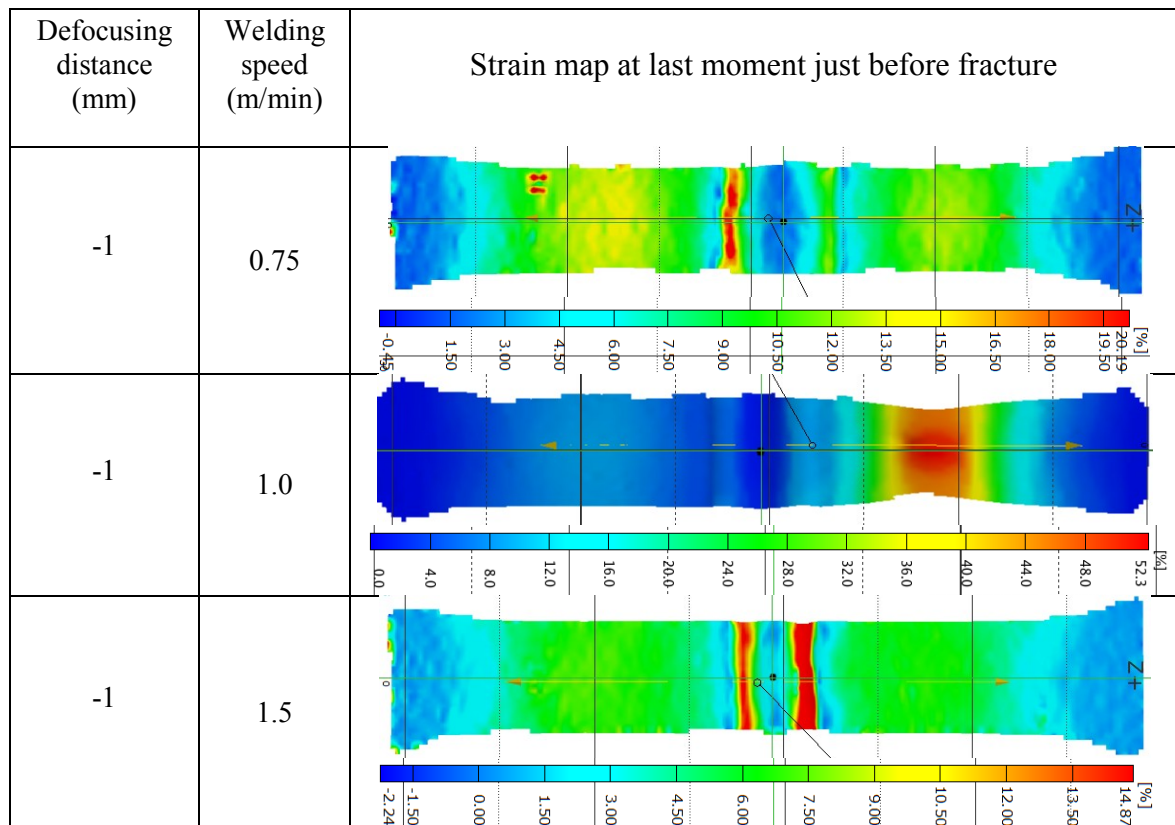
**Figure 5.10- Effect of welding speed on global tensile properties for 2 defocusing distances**

Dashed lines in the figures indicate the associated base metal values. The average joint efficiency has been calculated as 100.16% in terms of UTS ranging from a minimum of 96.79% to a maximum of 100.94%. Table 5.2 shows the failure locations and average joint efficiencies of all the tensile samples in this part of the study. Porosity is the main reason for the failure of the samples welded at lower welding speed. The result is clarified after observing the fracture surfaces using the SEM. A cluster of porosities is observed for all the samples welded at a speed of 0.75 m/min for the two defocusing distances, leading to failure in the FZs. Figure 5.7 confirms the presence of maximum porosity areas in these samples.

**Table 5.2: Failure locations and joint efficiencies of all the samples of this part of study**

Defocusing distance (mm)	Welding speed (m/min)	Failure locations (4 samples)	Joint efficiencies (%)
-1	0.75	4 FZ	100.56
	1.0	4 BM	100.94
	1.5	4 HAZ	99.72
	1.75	1 BM + 1 HAZ+ 2 FZ	100.85
	2.0	4 BM	100.75
-2	0.75	4 FZ	96.79
	1.0	1 BM + 3 HAZ	100.94
	1.5	4 HAZ	100.75

The digital images of the last moment just before fracture (Figure 5.11) for the samples failed in the FZ (at a welding speed of 0.75 m/min) show the maximum strains at the region of the underfill defects which means that the fracture initiates from the underfill defect and propagates through the weak FZ containing a cluster of porosities.



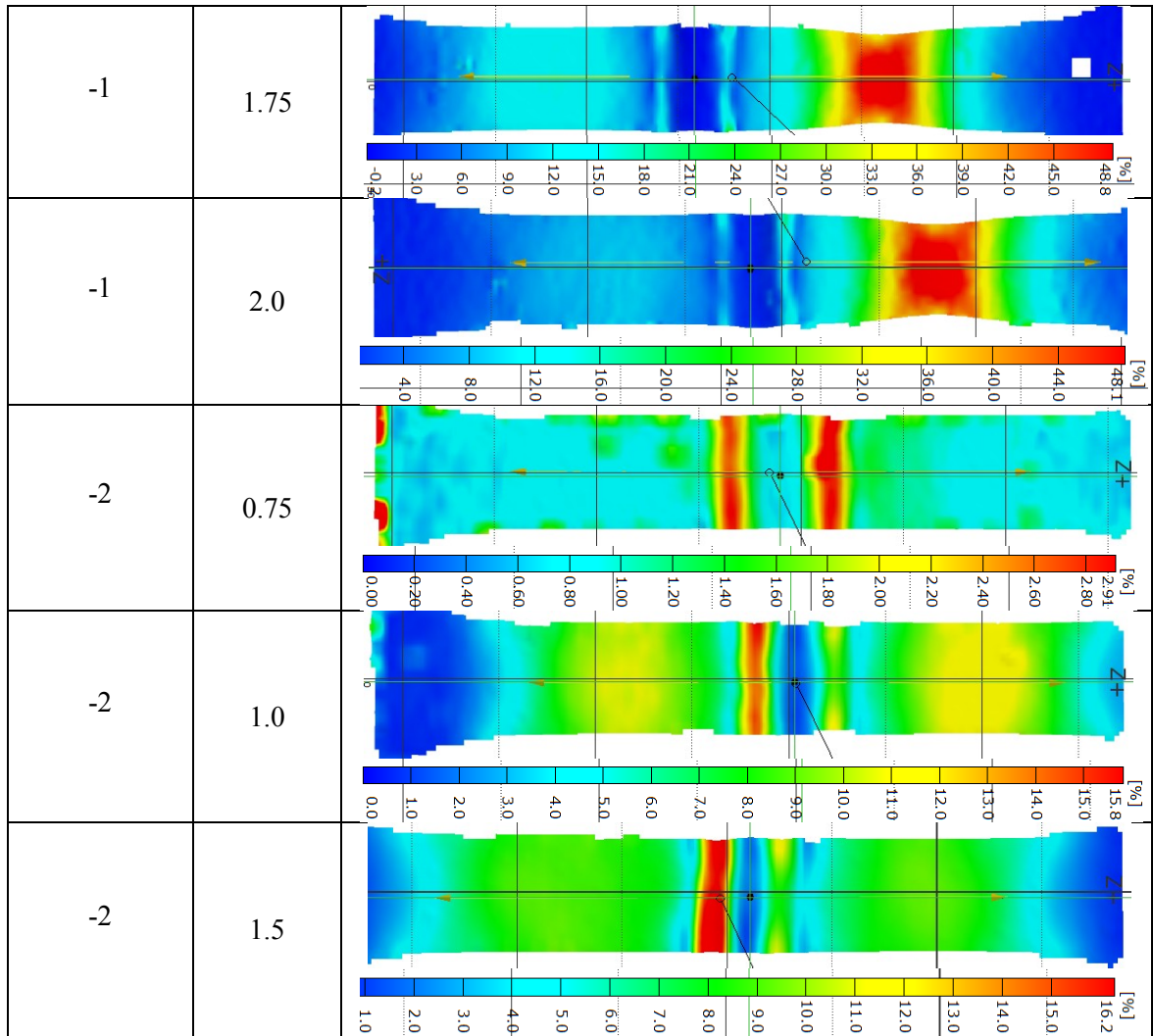


**Figure 5.11- Digital images of the last moment just before failure**

To further investigate whether the fracture initiates from the underfill defect or not, the distances on the digital image and the weld geometry data are compared. Figure 5.12 shows the result of the comparison. It is clear from the figure that the FZ top width is equal to the distance of the most rigid (minimum strain) position plus the two maximum strain positions. The most rigid position corresponds to the distance of the FZ middle width. Therefore, the maximum strain zones reflect the areas with underfill defects.

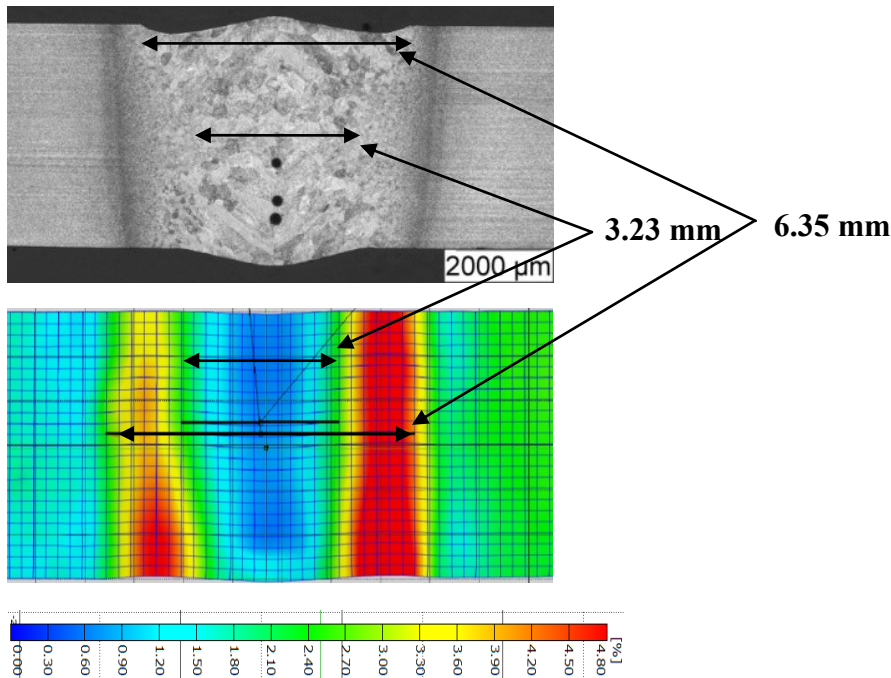


**Figure 5.12- Comparison of the digital image and transverse section of the sample welded at 0.75 m/min, Defocusing = -1 mm**

Failure in the HAZ is mainly due to the underfill defect. Samples welded at intermediate speed ( $\sim 1.5$  m/min) failed in the HAZ area. The underfill depths are the maximum at this welding speed as discussed earlier (Figure 5.5). Crack initiates from the underfill and propagate through the HAZ as the FZ has lower porosity at this welding speed (Figure 5.7). Failure in the BM is due to the presence of strong FZ in this case. Both the underfill defect and porosity are low for the samples failed in BM. Therefore, it is clear that underfill is the initiator of the tensile failures for all the samples failed in either FZ or HAZ. The propagation of the crack depends on the amount of porosity in the FZ. If the porosity area is high enough ( $\sim \geq 0.15$  mm<sup>2</sup>), the crack is more likely to propagate through the FZ. Although the maximum underfill depth for 5.08 mm thickness is 0.36 mm according to the AWS D17.1 [81] specifications, 0.29 mm of underfill depth is found to be the maximum tolerated value in this work. If the underfill depth is high enough

( $\sim \geq 0.29$  mm), the crack will propagate through the HAZ if the porosity area remains less than the threshold ( $\sim \geq 0.15$  mm<sup>2</sup>).

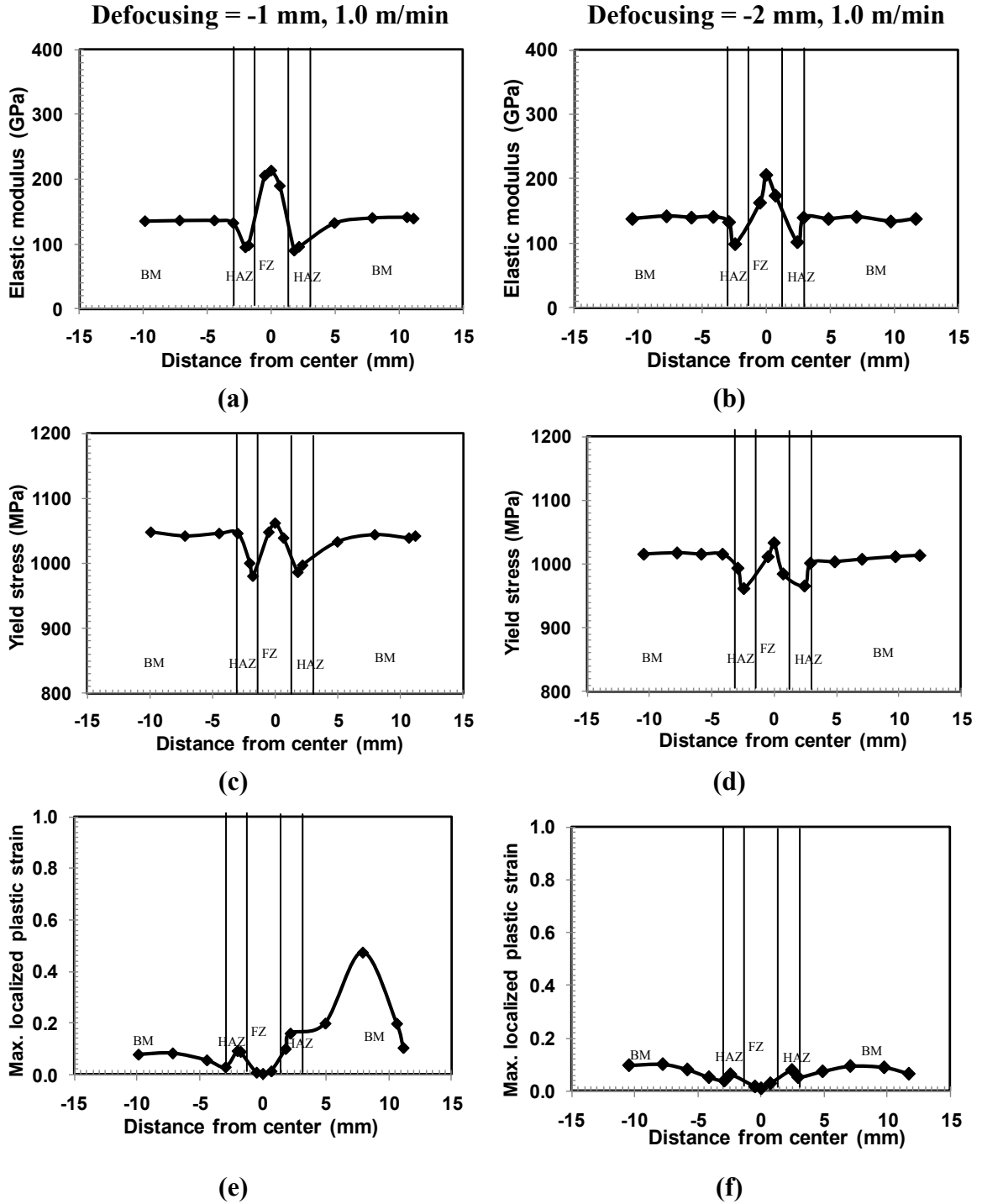


Figure 5.13- Local tensile properties of Defocusing = -1 mm, 1.0 m/min (failed in the BM) and Defocusing = -2 mm, 1.0 m/min (failed in the HAZ)

## 5.6 Local Tensile Property

Figure 5.13 shows the local tensile properties throughout the gage lengths of the samples welded at a welding speed of 1.0 m/min for the two defocusing distances. The local properties are very similar to those obtained for 3.175 mm sheets. Elastic modulus increases in the FZ and then decreases in the HAZ. Yield stress is slightly higher in the FZ than in the BM and is minimum in the HAZ. Localized plastic elongation is the maximum in the fracture zone (BM) and almost zero in the FZ as shown in Figure 5.13e & f. Although the fracture occurred in the HAZ for the sample at defocusing distance of -2 mm and welding speed of 1.0 m/min, the localized plastic strain is maximum in the base metal (Figure 5.13f). Therefore, it is not always true that fracture will originate at the position of maximum strain.

Figure 5.14 shows the effect of welding speed on the local tensile properties for defocusing -1 mm and -2 mm. FZ shows the maximum elastic modulus and yield stress and the minimum localized plastic strain at fracture. Elastic modulus and yield stress increase with increasing welding speed for the two defocusing distances due to the finer martensite and prior- $\beta$  grains (Figure 5.14a, b, c, & d). Elastic modulus and yield stress of the heat affected zones for the last two samples at defocusing -1 mm (Figure 5.14a & c) seem to increase with increasing welding speed. This may be due to the strengthening of the HAZ by refined martensitic structure for double sided welding. This type of HAZ strengthening has been reported by Wojnowski *et al.*[88] for steels by multi-pass welding. The localized plastic strain of the FZ is found to increase with increasing welding speed for the prior- $\beta$  grain refinement (Figure 5.14e & f).

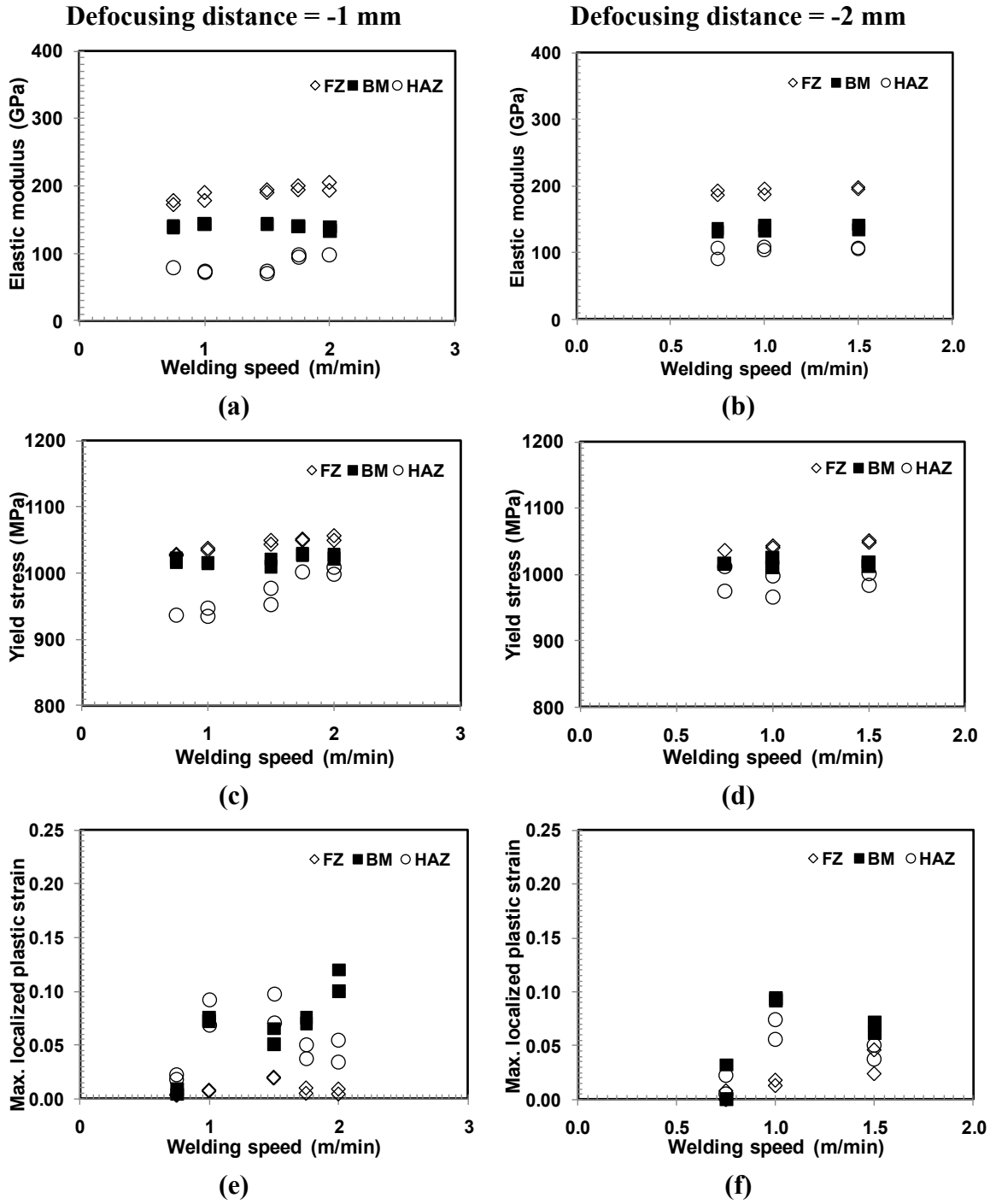
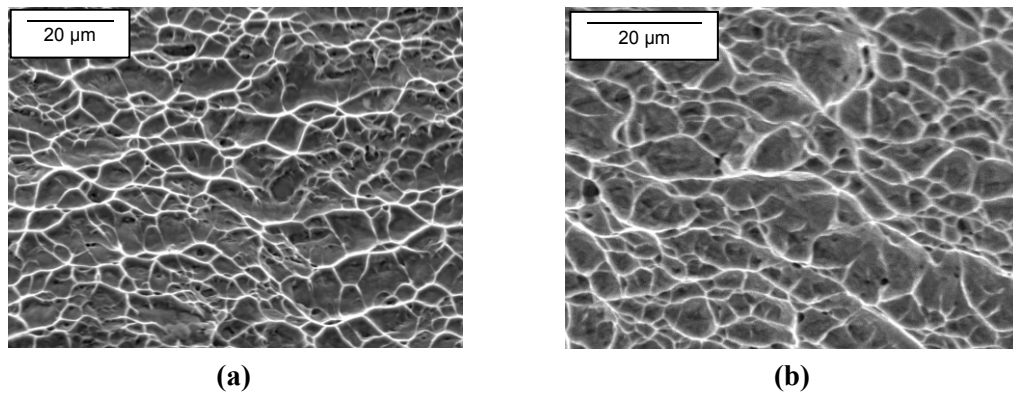


Figure 5.14- Local tensile properties for Defocusing = -1 mm and Defocusing = -2 mm

## 5.7 Fractography

Figure 5.15 shows the scanning electron microscope fractographic analysis of the samples. The analysis revealed the presence of ductile dimple structure involving the operation of a micro-void coalescence mechanism.



**Figure 5.15- SEM fracture surfaces (a) Defocusing -1 mm, 1.0 m/min (b) Defocusing -2 mm, 0.75 m/min**

## 5.8 Operating Window

Figure 5.16 shows the operating window for the laser welding of 5.08 mm thick Ti-6Al-4V alloy with 4.0 kW laser power and defocusing distances of -1 and -2 mm.

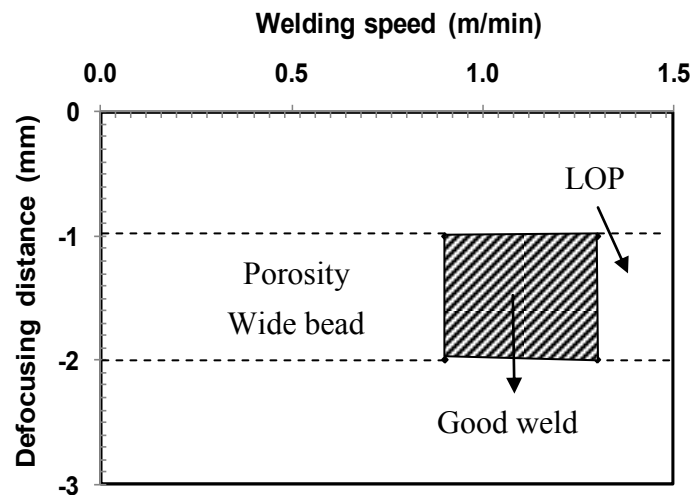


**Figure 5.16- Operating window for the 5.08 mm thickness**

## Chapter 6/ Effect of Joint Gap

---

The 3.175 mm and 5.08 mm thick samples have been welded at various joint gaps using Ti-6Al-4V filler wire with a nominal diameter of 1.14 mm. The parameters are shown in Table 6.1.

**Table 6.1: Key experiment / effect of joint gap**

Sample #	Thickness (mm)	Joint gap (mm)	Laser power (kW)	Welding speed (m/min)	Wire feed rate (m/min)	Defocusing distance (mm)
T 118	3.175	0.0	3	1.69	0.0	-1
T 167		0.1			0.53	
T 166		0.2			1.05	
T 164		0.3			1.58	
T 165		0.4			2.10	
T 168		0.5			2.63	
T 169		0.6			3.16	
T 137		5.08			0.0	
T 157	0.1		0.5			
T 158	0.2		1.0			
T 156	0.3		1.5			
T 159	0.4		2.0			
T 160	0.5		2.5			
T 161	0.6		3.0			

### 6.1 Weld Geometry

Figure 6.1 shows the overviews of the transverse sections obtained at various joint gaps for both thicknesses. All the joints are fully penetrated with the presence of two main defects, underfill and porosity.

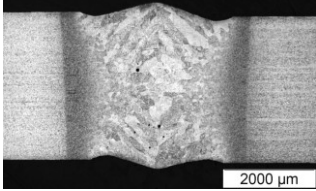
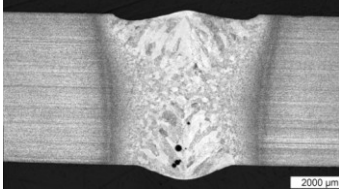
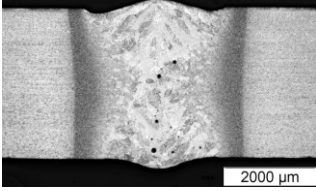
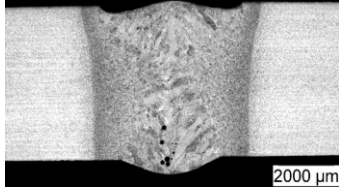
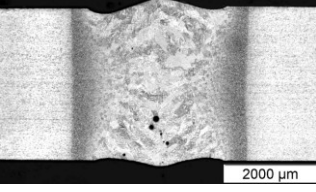
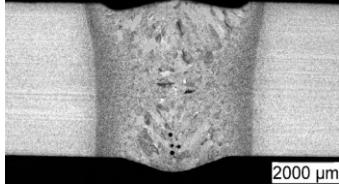
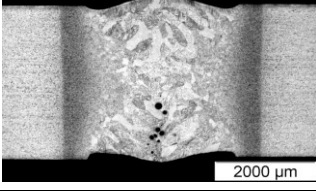
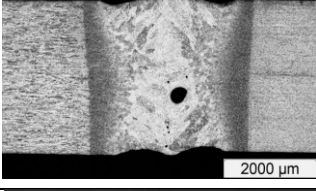
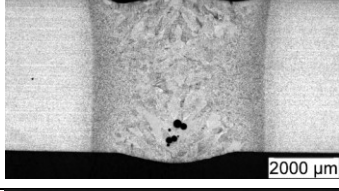
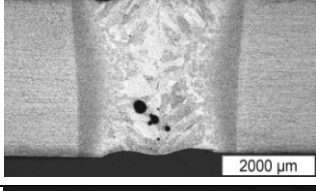
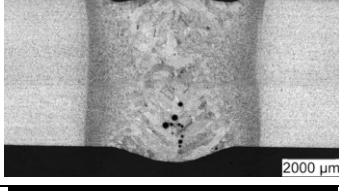
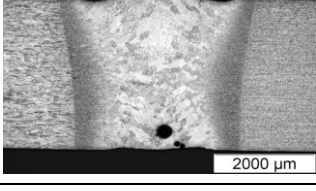
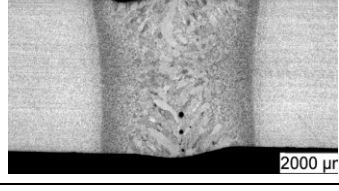
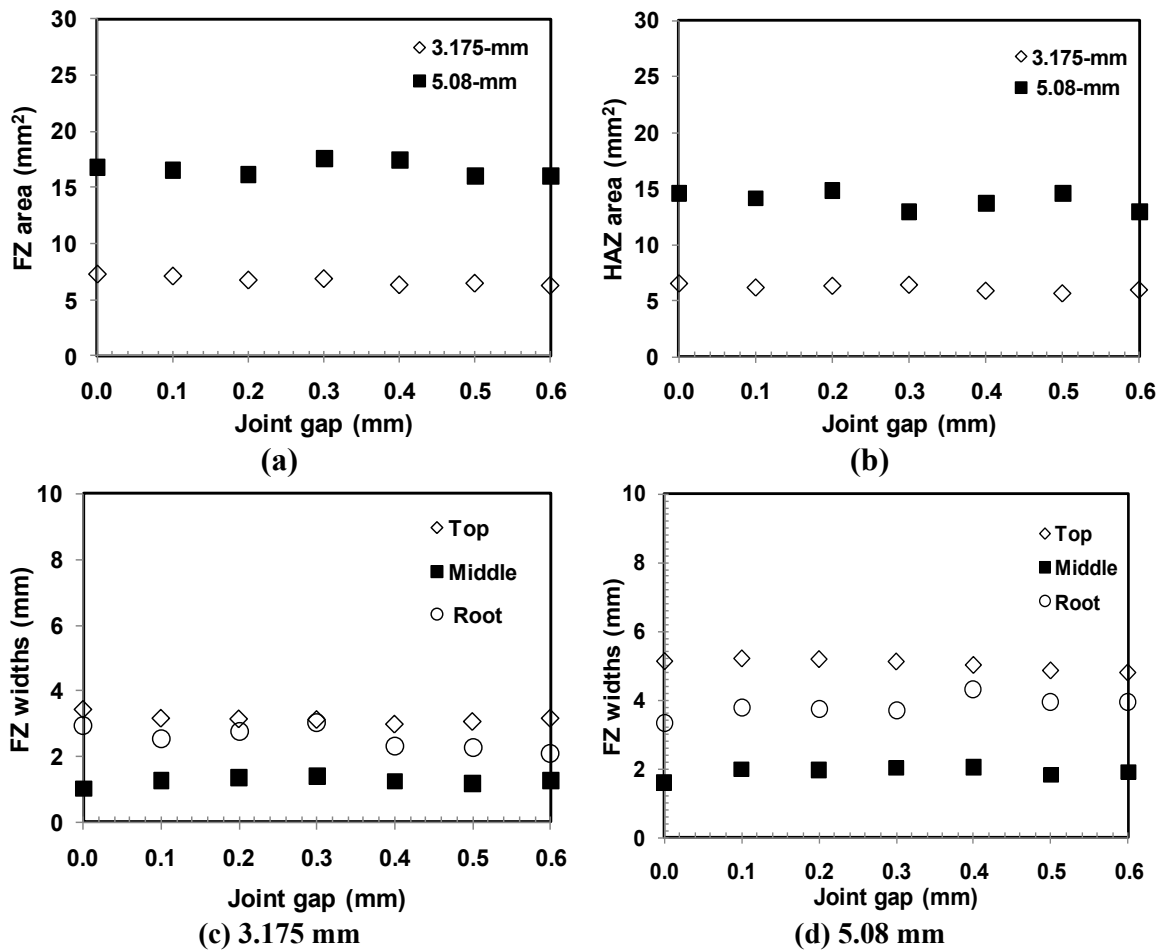
Joint gap (mm)	3.175 mm	5.08 mm
0.0		
0.1		
0.2		
0.3		
0.4		
0.5		
0.6		

Figure 6.1- Effect of joint gap on transverse sections for both thicknesses

Figure 6.2 shows the effect of joint gap on weld geometry for the two thicknesses. The FZ and HAZ areas, the FZ top and root widths have a general tendency to decrease to some extent with increasing joint gaps. This is related to the gap sizes of the joints. When welding is done with a larger joint gap, part of the laser beam energy will be lost through the gap. The amount of this lost laser energy will increase with increasing joint gap, resulting in less effective energy available for welding and smaller FZ and HAZ dimensions.



**Figure 6.2- Effect of joint gap on FZ and HAZ dimensions for both thicknesses**

Figure 6.3 shows the effect of joint gap on weld reinforcement. The total reinforcement area decreases with increasing joint gap for 3.175 mm sheets but no clear tendency for

5.08 mm welds. The reinforcement heights vary from 0 to 0.3 mm for 3.175 mm sheets and 0.15 to 0.5 mm for 5.08 mm welds indicating that the reinforcement heights are less than 10% of the plate thicknesses for all the joints.

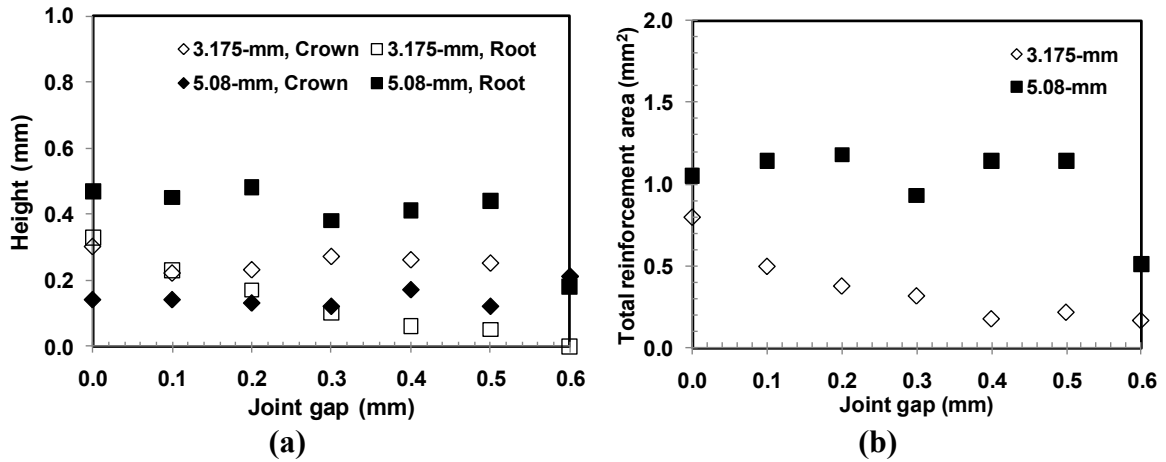
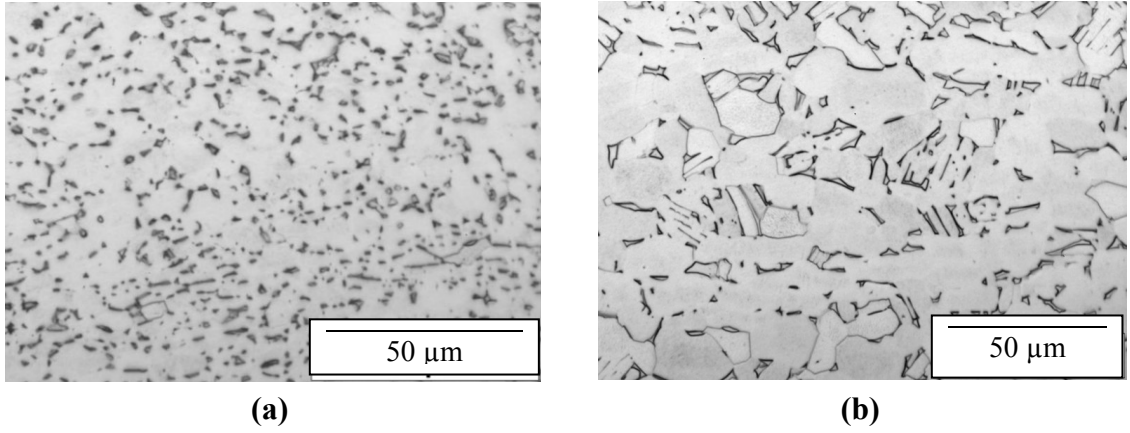


Figure 6.3- Effect of joint gap on weld reinforcements

## 6.2 Microstructure

Figure 6.4 shows typical microstructures of the base metal at joint gap of 0.3 mm. The base metal of 3.175 mm is composed of equiaxed  $\alpha$  with intergranular  $\beta$  (mill annealed condition) and the base metal for 5.08 mm thick sample is composed of equiaxed and acicular  $\alpha$  grains with intergranular  $\beta$ . According to the ASM handbook Volume 9 (Metallography and Microstructures), this is a microstructure similar to that forging solution treated for 1 h at 955°C followed by air cooling, and again aged for 2 h at 705°C. Figure 6.5 shows typical microstructures of the fusion zone for the two thicknesses consisting mainly of  $\alpha'$  martensite with small amount of  $\beta$  (not visible under optical microscope). In this study, the filler wire has the same composition as the base metal. No significant differences are observed in FZ microstructures at various joint gaps for both thicknesses. HAZ structures of both the thicknesses consist of mixed structure of both FZ and BM where the amount of  $\alpha'$  decreases from FZ to BM (Figure 6.6).



**Figure 6.4- Typical microstructures for the base metal of joint gap 0.4 mm (a) 3.175 mm and (b) 5.08 mm**

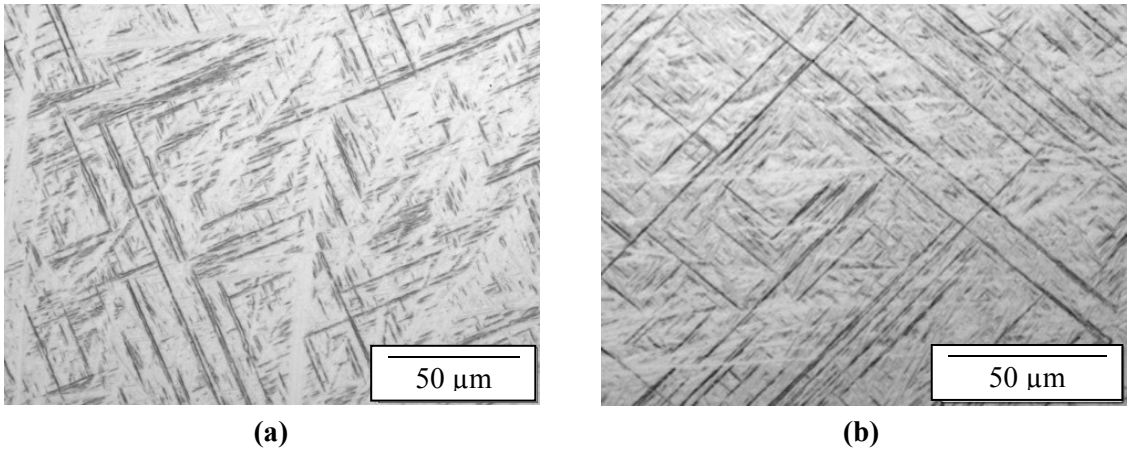


**Figure 6.5- Typical microstructures for the fusion zone of joint gap 0.4 mm (a) 3.175 mm and (b) 5.08 mm**

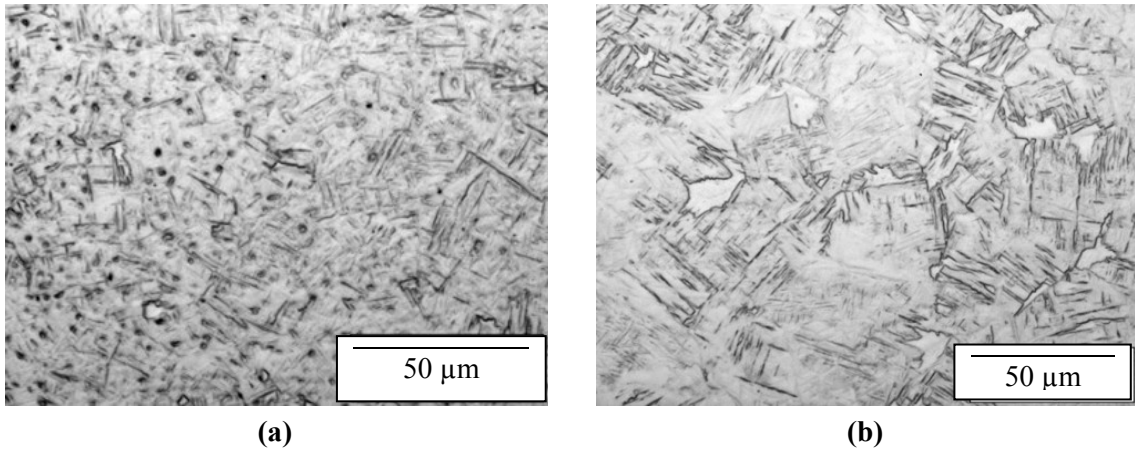


**Figure 6.6- Typical microstructures for the heat affected zone of joint gap 0.4 mm (a) 3.175 mm and (b) 5.08 mm**

## 6.3 Defects

### 6.3.1 Underfill

Underfill is one of the most common defects as observed in Figure 6.1. The effect of joint gap on underfill defects is shown in Figure 6.7. The maximum top underfill depth is obtained at 0 mm joint gap where no filler wire is used. As the joint gap increases up to 0.6 mm, the underfill depth decreases slightly for 5.08 mm thick samples. Therefore, the use of filler wire can reduce the underfill defect though this tendency is not so clear for 3.175 mm thick samples. This supports the results found by Cao *et al.* [48] where they identified the evaporation of vanadium as the main reason for underfill defect in case of zero joint gap and the use of filler wire can significantly reduce the loss of molten metal by reducing the evaporation rate.

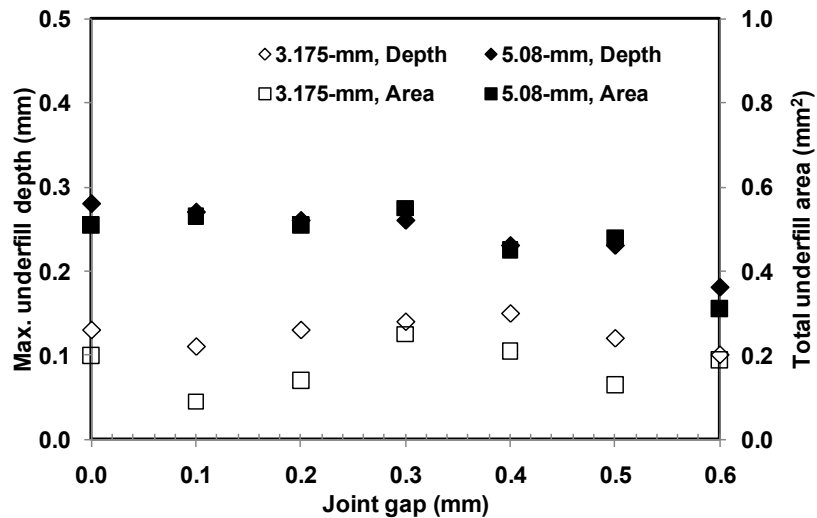
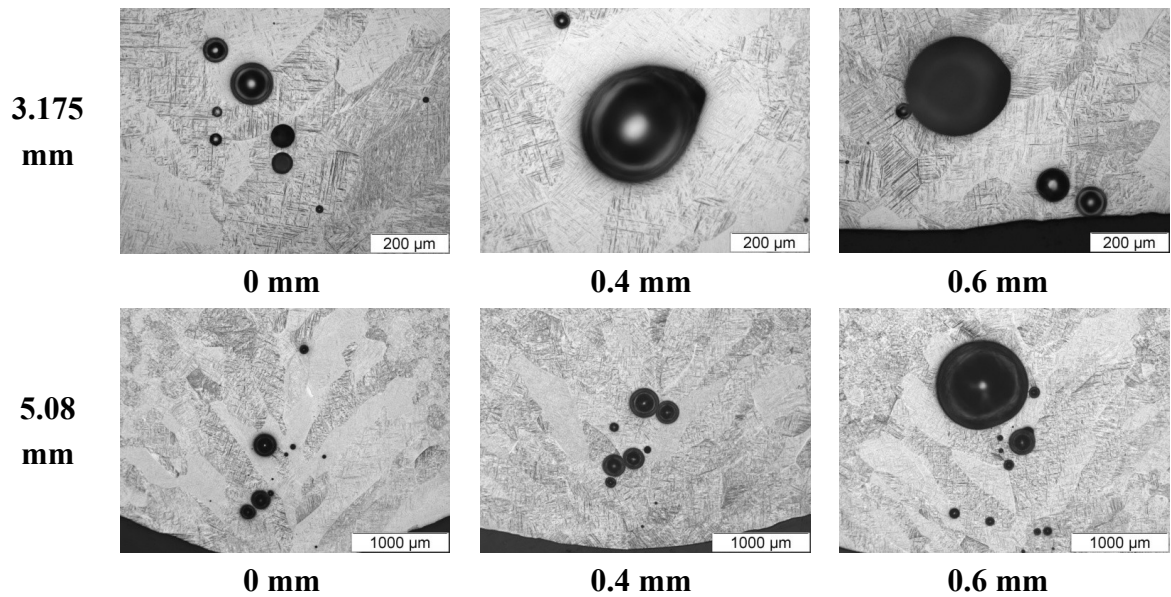


Figure 6.7- Effect of joint gap on underfill defect

### 6.3.2 Porosity

Porosity is another main defect frequently observed in the joints as shown in the transverse sections in Figure 6.1. Some examples of the porosity present in various joint gaps are shown in Figure 6.8. Most of the porosities have spherical shape indicating that they are most likely to be gas porosities. Also the porosities are mainly located in the lower part of the FZ indicating that the unstable keyhole is one of the reasons of porosity formation. Figure 6.9 shows the relationship between the joint gap and total porosity area. Both the porosity area and percentage of porosity area increase with increasing joint gap. The larger the joint gap, the more the filler wire is used. The surface of the filler wire absorbs moisture which can be a source of porosity. On the other hand, the joint gap itself is a source of porosity. Although the maximum percentage of porosity is 1.3%, it could deteriorate the strength of the weld especially when large porosities exist.



**Figure 6.8- Examples of porosity present in joints with various joint gaps for both thicknesses**

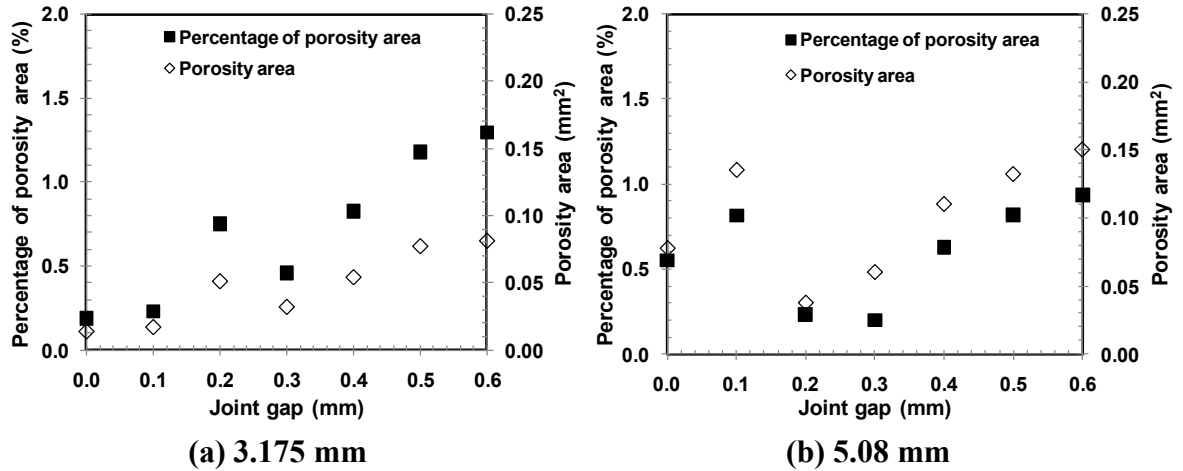


Figure 6.9- Effect of joint gap on porosity area and area percentage

#### 6.4 Micro-Indentation Hardness

A typical hardness profile for the 3.175 mm sheet welded at 3 kW laser power and 0.4 mm of joint gap is shown in Figure 6.10. The FZ shows the maximum and the BM shows the minimum hardness values. The average FZ hardness for 3.175 mm sample is  $361 \pm 4$  HV 300 gf and for 5.08 mm is  $354 \pm 5$  HV indicating 15.70 % and 13.46 % increase in the FZ hardness than BM. A slight increase of the FZ average hardness for the thinner samples is observed due to the higher cooling rate than the thicker samples. The effect of joint gap on FZ average hardness is shown in Figure 6.11. A slight decrease in FZ average hardness is observed for increasing joint gap. This may be associated with the decrease in net effective energy (section 6.1) with increasing joint gap. The dashed line on the graph indicates the average BM hardness.

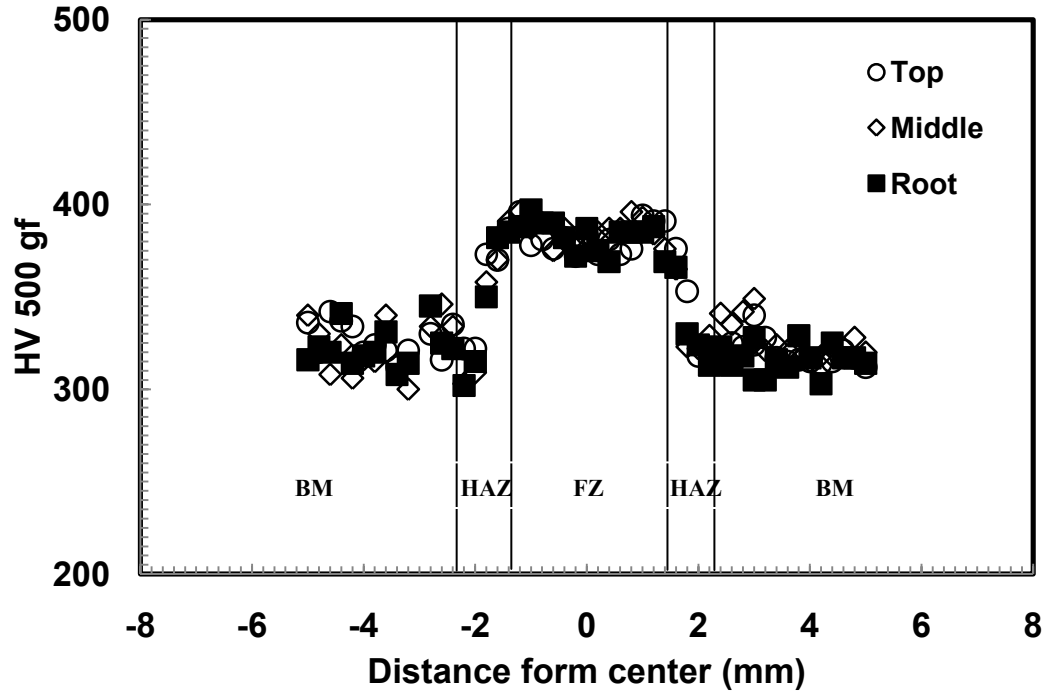


Figure 6.10- Typical micro-indentation hardness profile at 0.4 mm joint gap welded at 3 kW laser power and at a welding speed of 1.69 m/min

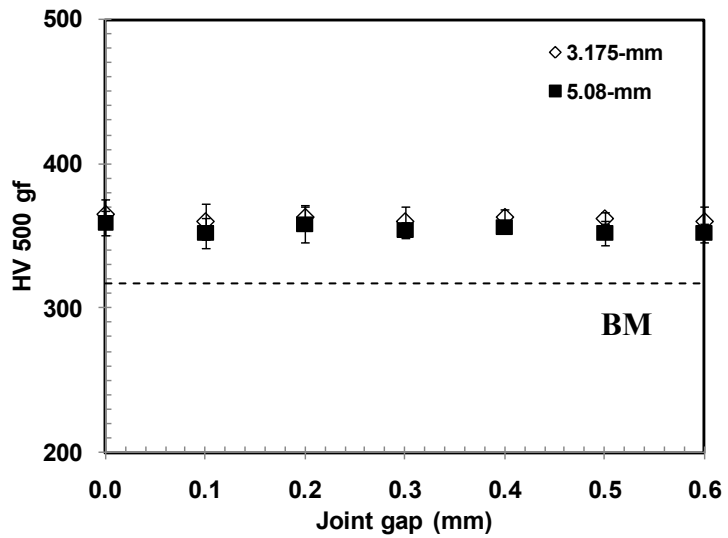


Figure 6.11- Effect of joint gap on FZ average hardness

## 6.5 Global Tensile Properties

Three samples have been prepared for each joint gap except four for zero joint gaps. Two of them are tested by DIC technique and the remaining by conventional MTS machine. Figure 6.12 shows the effect of joint gap on global tensile properties for both thicknesses. Dashed lines on the figure represent the corresponding tensile properties of the BM. Joint gaps seem not to have any significant influence on the global tensile properties for both thicknesses. All the 22 samples failed in the BM for 3.175 mm thickness indicating strong joint quality regardless of the presence of porosity and underfill defects as shown in Table 6.2.

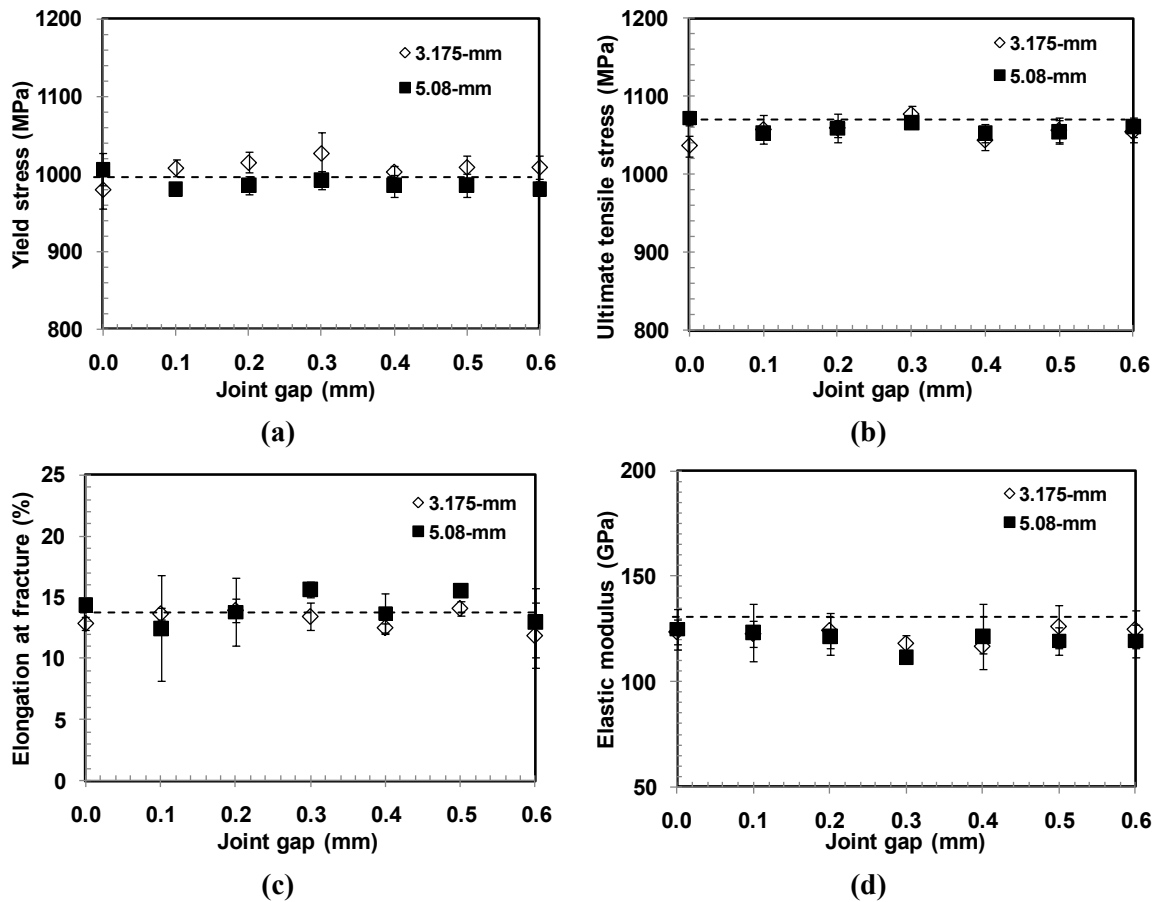


Figure 6.12- Effect of joint gap on global tensile properties

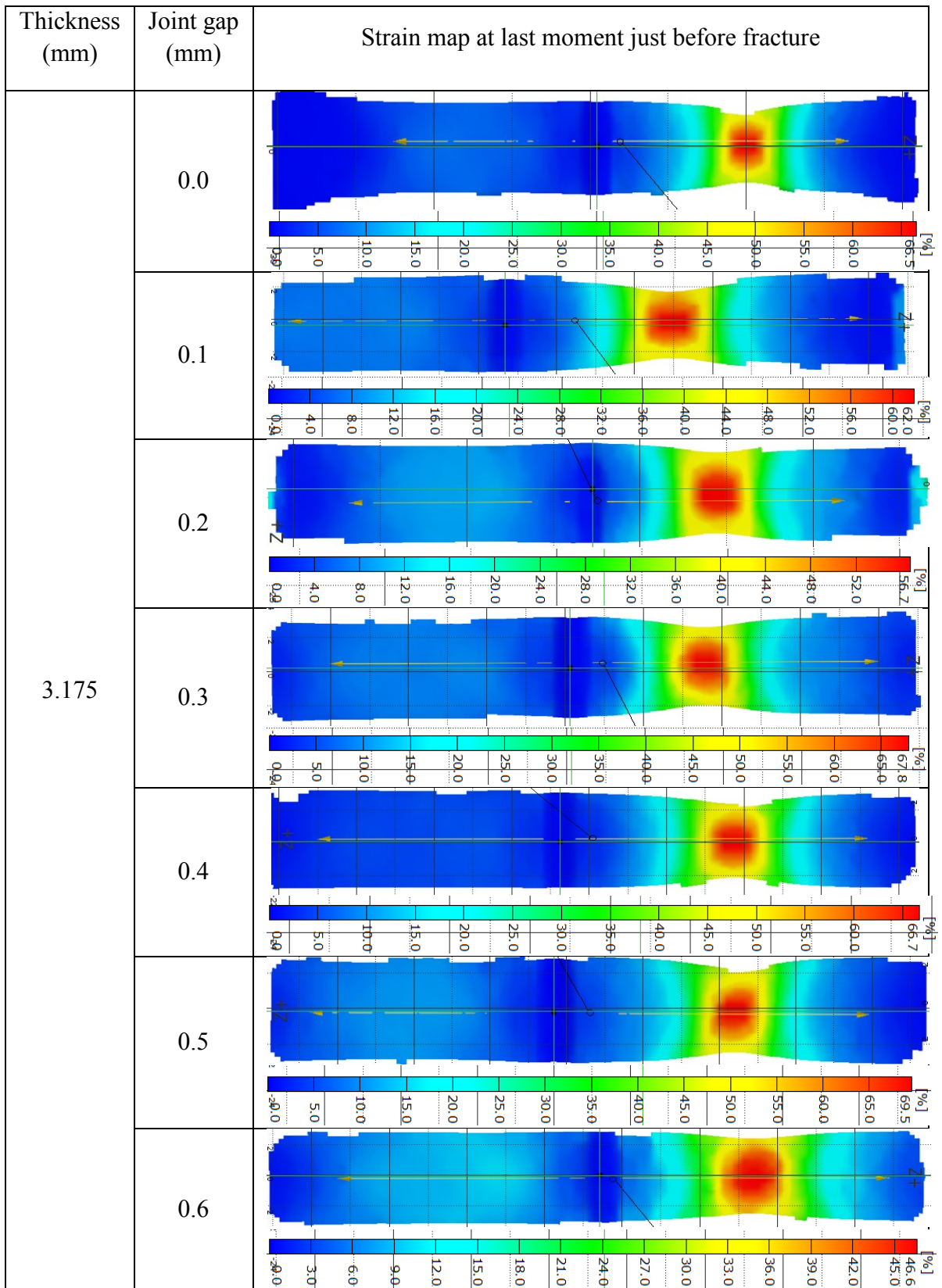
Failure locations for 5.08 mm thick samples are quite scattered. 17 samples have been failed in the BM among all of the 22 samples indicating that the quality of welds is still good in most cases. The average joint efficiency is 99.6% in terms of UTS ranging from a minimum of 97.6% to a maximum of 101.5%. All the zero joint gap samples failed in the BM indicating a strong joint quality. For 0.1 mm joint gap, one sample failed in the FZ is due to the high amount of porosity area as shown in Figure 6.9b. All the samples with joint gaps of 0.3 and 0.5 mm failed in the BM. Although the reasons behind the failures in the HAZ are not clear for the joint gap of 0.2, 0.4 and 0.6 mm, underfill defect is the initiator in case of failure for these samples.

**Table 6.2: Failure locations of all the samples of this part of study**

<b>Thickness (mm)</b>	<b>Joint gap (mm)</b>	<b>Failure locations (3-4 samples)</b>
3.175	0.0	4 BM
	0.1	3 BM
	0.2	3 BM
	0.3	3 BM
	0.4	3 BM
	0.5	3 BM
	0.6	3 BM
5.08	0.0	4 BM
	0.1	2 BM + 1 FZ
	0.2	2 BM + 1 HAZ
	0.3	3 BM
	0.4	2 BM + 1 HAZ
	0.5	3 BM
	0.6	2 HAZ + 1 BM

## 6.6. Local Tensile Properties

Figure 6.13 shows the digital images of the last moment just before failure. For 3.175 mm thick samples, all the images show that the maximum strain localization is in the BM where fractures took place. However, 5.08 mm thick sample with 0.6 mm joint gap is failed in the HAZ where the maximum strain localization is observed.



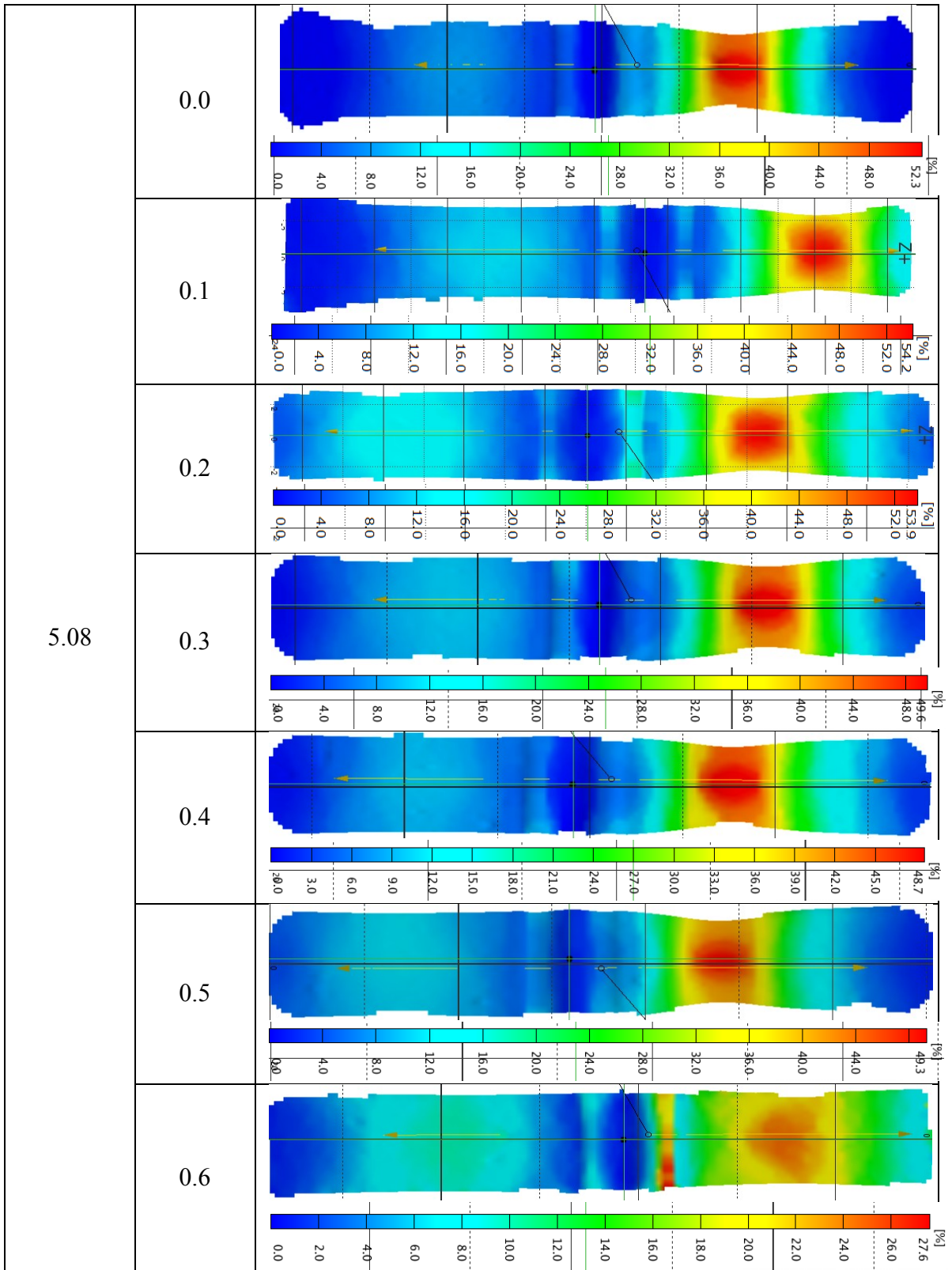
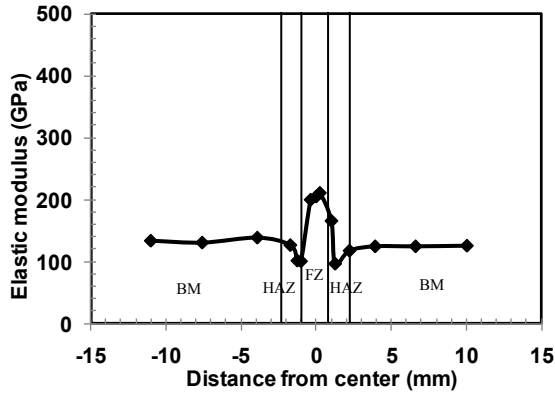


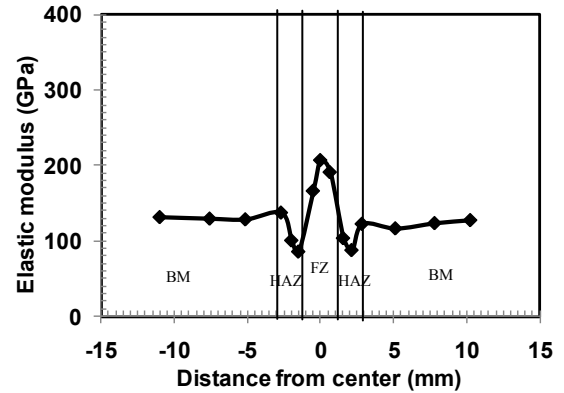
Figure 6.13- Digital images of the last moment just before failure

3.175 mm thickness (0.4 mm joint gap)

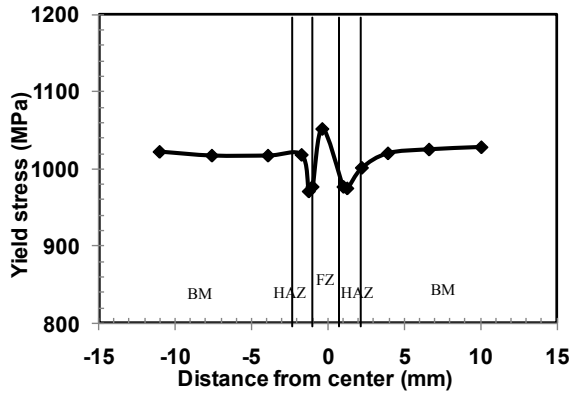
5.08 mm thickness (0.4 mm joint gap)



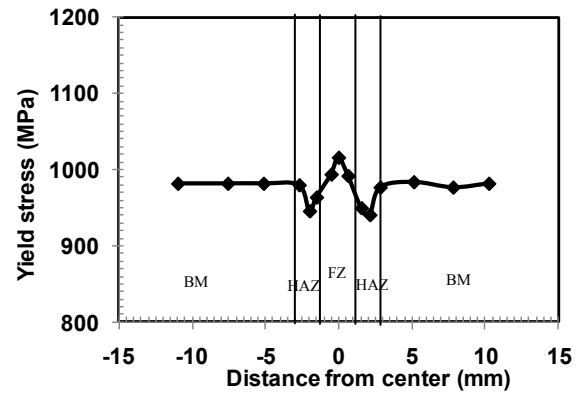
(a)



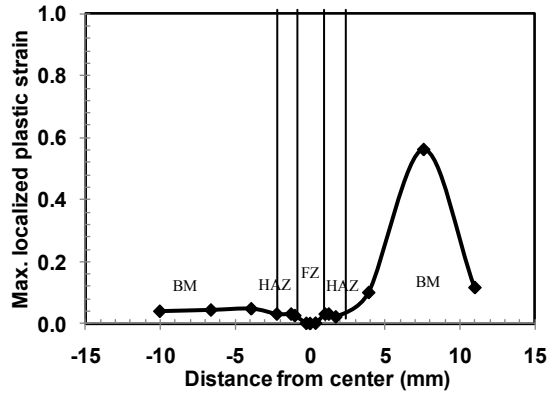
(b)



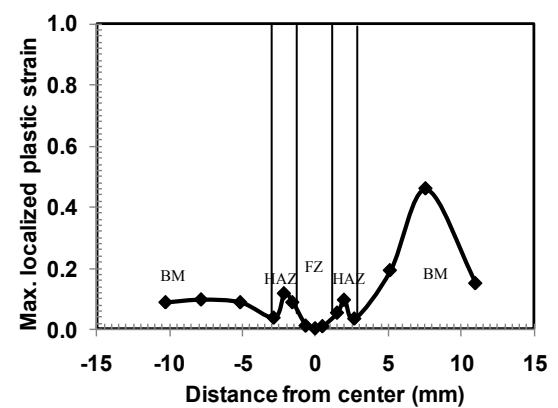
(c)



(d)



(e)



(f)

**Figure 6.14- Local tensile properties of 3.175 mm thickness (0.4 mm joint gap) and 5.08 mm thickness, (0.4 mm joint gap)**

Figure 6.14 shows the variations of local tensile properties in the gage lengths for two thicknesses at joint gaps of 0.4 mm. The tendencies of the local tensile behaviour are similar as described in the previous two sections. The FZ shows the maximum elastic

modulus and yield stress whereas the HAZ shows the minimum. Localized plastic strains are the maximum at the points of failure (BM for both cases).

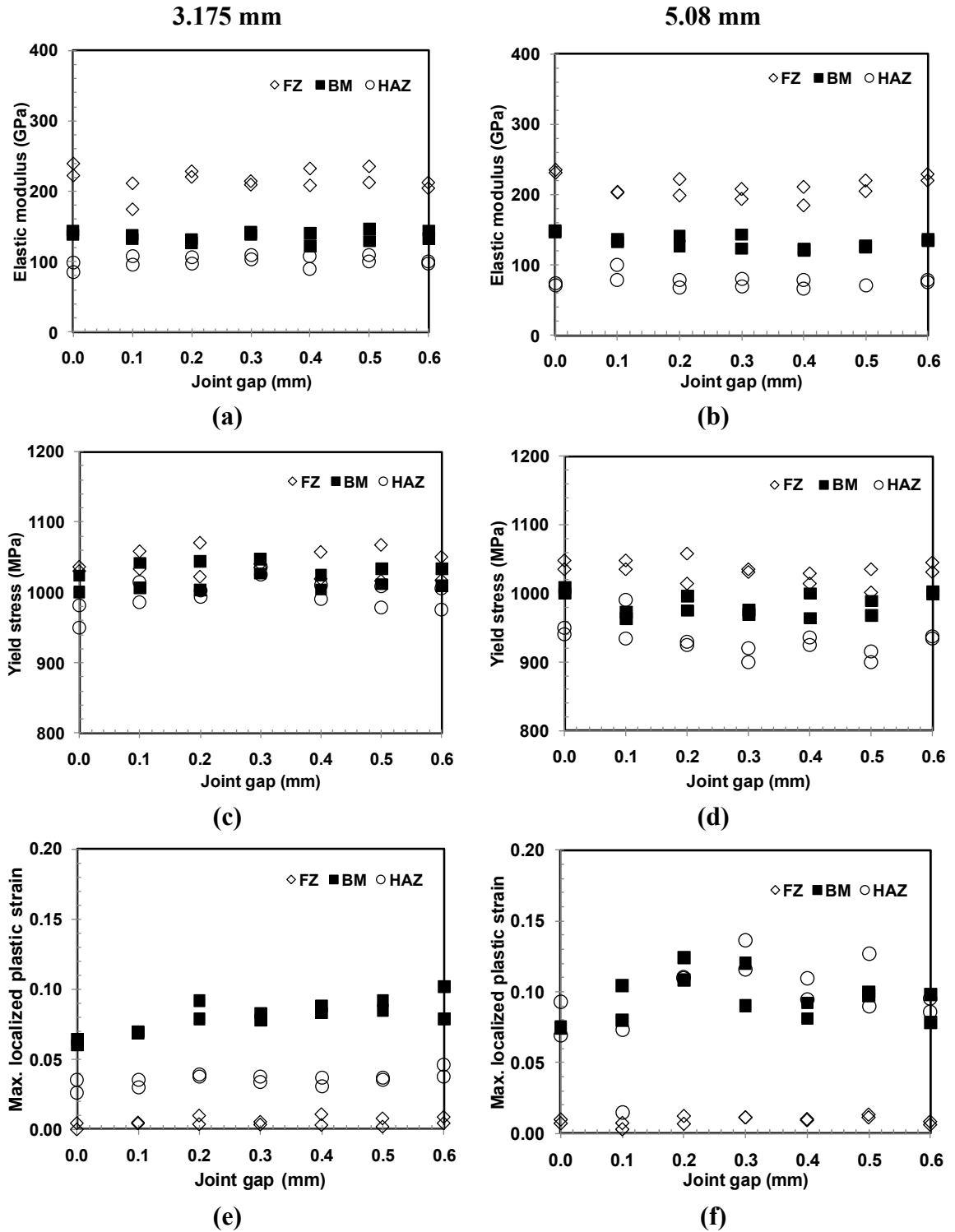
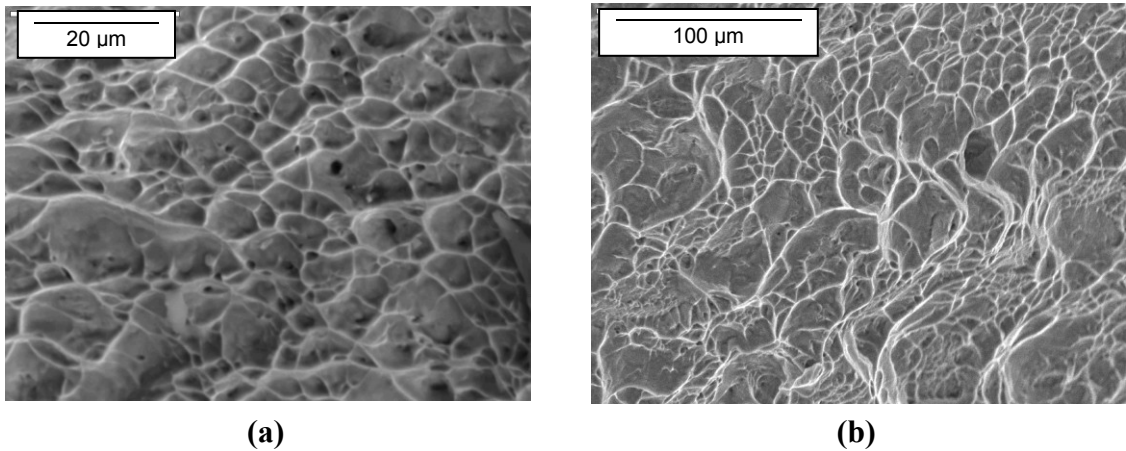


Figure 6.15- Local tensile properties of 3.175 mm and 5.08 mm thick samples

Figure 6.15 shows the effect of joint gap on the local tensile properties for 3.175 and 5.08 mm welds. FZ shows the maximum elastic modulus and yield stress and the minimum localized plastic strain at fracture. No significant difference is observed in the local tensile properties with the increase in joint gap for both thicknesses.

## 6.7 Fractography

Scanning electron microscope fractographic analysis reveals that the fractures are ductile dimple structure as shown in Figure 6.16.



**Figure 6.16: SEM fracture surface of (a) 3.175 mm, 0.3 mm joint gap (b) 5.08 mm, 0.2 mm joint gap**

## Chapter 7/ Effect of Post-Weld Heat Treatment

---

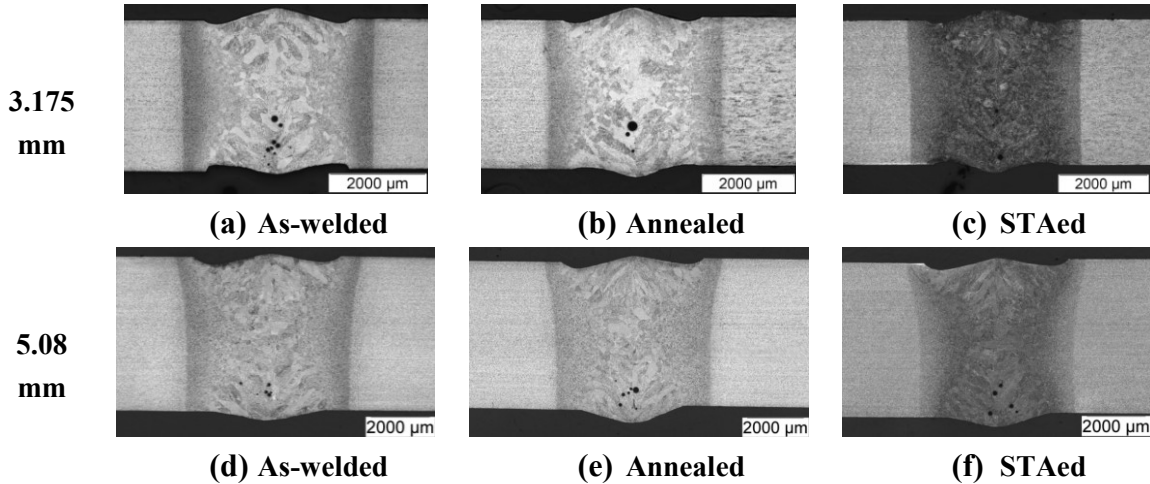
The 3.175 and 5.08 mm thick samples have been heat treated after welding and have been compared with the as-welded conditions. The parameters are shown in Table 7.1.

**Table 7.1: Key experiments / effect of post-weld heat treatment**

Sample #	Thickness (mm)	Laser power (kW)	Welding speed (m/min)	Joint gap (mm)	Wire feed rate (m/min)	Post-weld heat treatment
T 164	3.175	3.0	1.69	0.3	1.58	As-welded
T 172		3.0	1.69	0.3	1.58	Annealed
T 173		3.0	1.69	0.3	1.58	STAed
T 156	5.08	4.0	1.0	0.3	1.5	As-welded
T 162		4.0	1.0	0.3	1.5	Annealed
T 163		4.0	1.0	0.3	1.5	STAed

In this study, two post-weld heat treatment conditions (PWHT) have been investigated. One is annealing for stress relief and the other is full heat treatment i.e. solution heat treatment + aging (STAing). The stress relief annealing is carried out by heating the specimen to 538°C for 4 hours followed by argon quenching while the STAing heat treatment is carried out by heating the specimen to 913°C for 45 minutes followed by argon quenching and then aging at 538°C for 4 hours followed by argon quenching. The specimens chosen for these heat treatment processes are welded using 3 kW laser power at a speed of 1.69 m/min and a defocusing distance of -1 mm for the 3.175 mm thick samples and 4 kW laser power at a speed of 1.0 m/min for the 5.08 mm thick samples. The joint gap is 0.3 mm for both thicknesses and wire feed rate of 1.58 and 1.5 m/min for 3.175 and 5.08 mm, respectively. The samples are then compared with the as-welded condition. Figure 7.1 shows the transverse sections of the three different post-weld heat

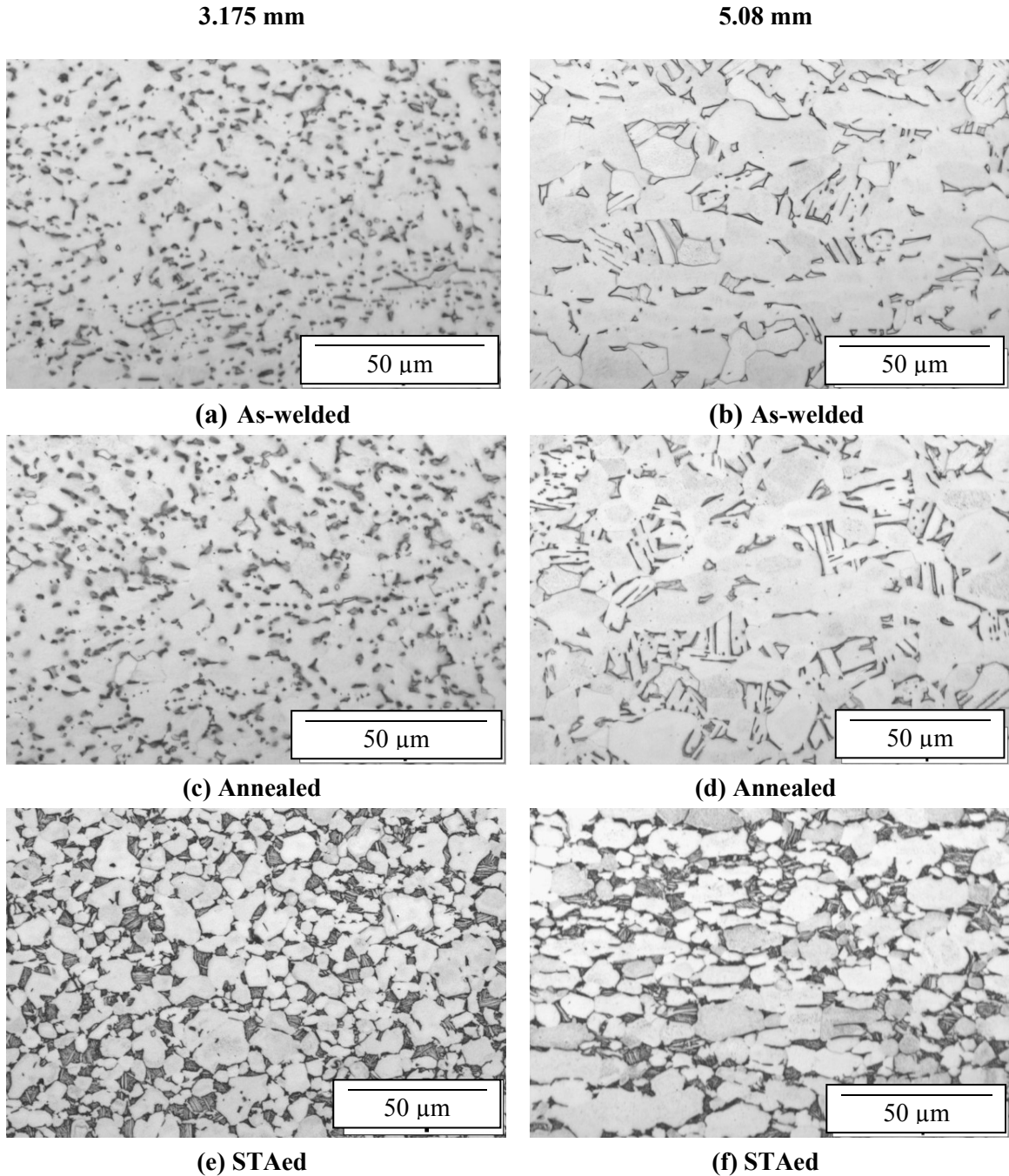
treatment conditions for the two thicknesses. No differences in the weld geometry and reinforcements have been found for the three PWHT conditions.



**Figure 7.1- Transverse sections in three different post-weld conditions**

## 7.1 Microstructure

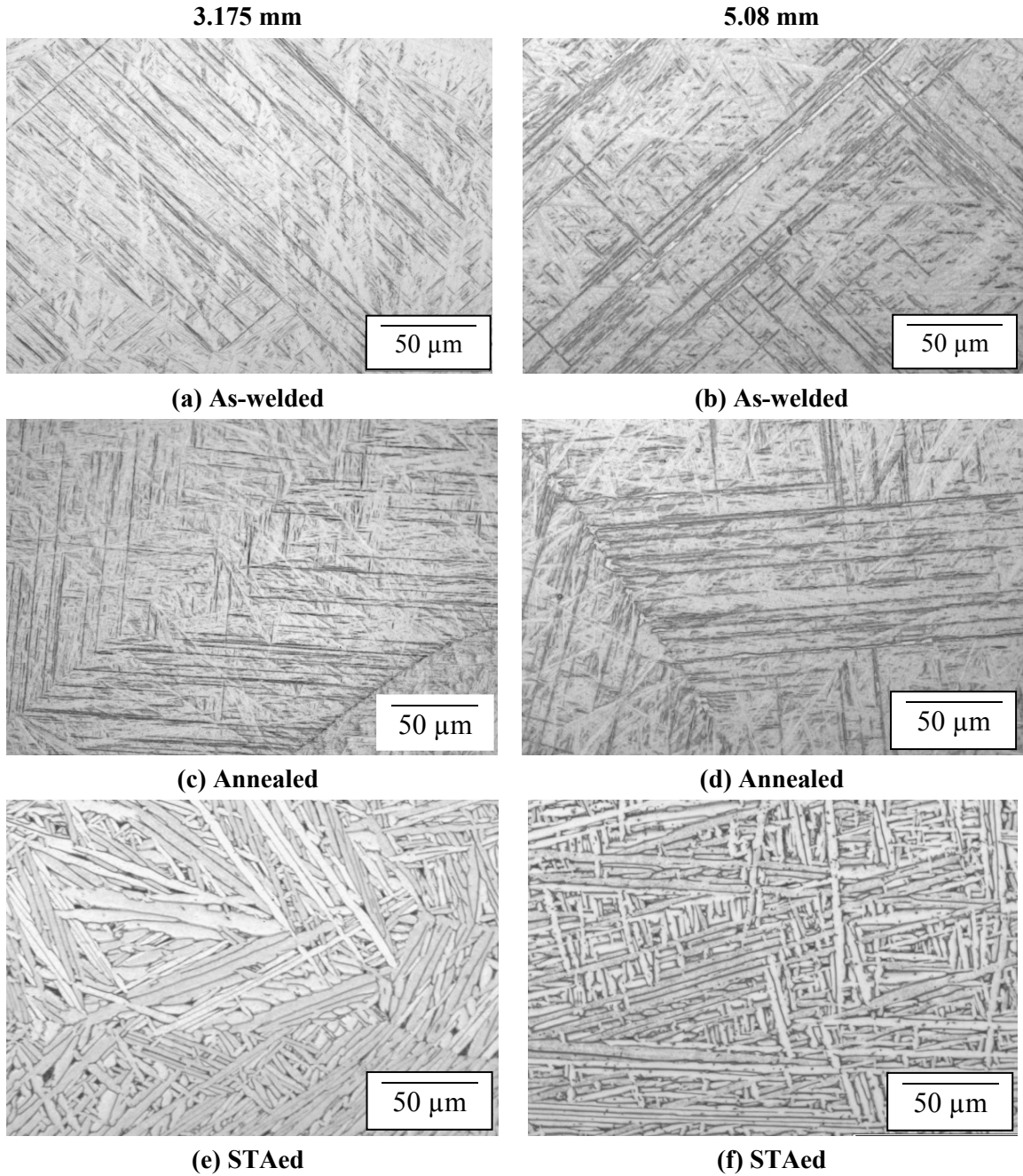
Figures 7.2 and 7.3 show three base metal microstructures for both thicknesses at three post-weld heat treatment conditions. The as-welded base metal microstructure (Figure 4.4.2a) consists of equiaxed  $\alpha$  with intergranular  $\beta$  for 3.175 mm sheet and equiaxed and acicular  $\alpha$  grains with intergranular  $\beta$  for 5.08 mm sheet (Figure 4.4.2b). After post-weld annealing treatment, little change in the base metal structure is observed under the optical microscope for both thicknesses (Figure 7.2c & d). However, heat treatment at high temperature (913°C) changes the BM microstructure. The base metal in STAed condition consists of primary  $\alpha$  in a matrix of transformed  $\beta$  containing acicular  $\alpha$  phases (Figure 7.2e & f).



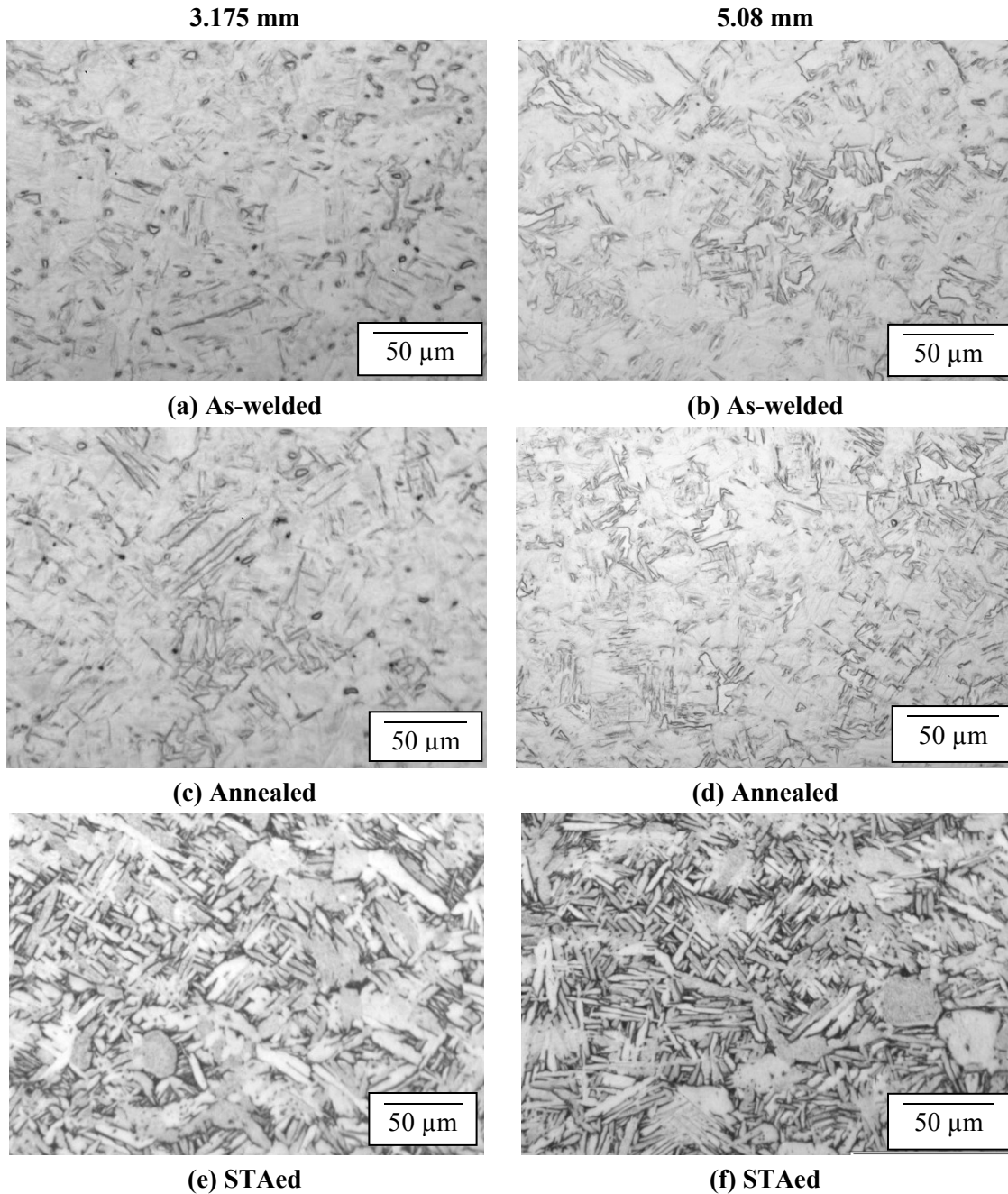
**Figure 7.2- BM microstructure at as-welded, annealed and STAed conditions for the two thicknesses**

Figure 7.3 shows the microstructures of the fusion zone in as-welded, annealed and STAed conditions. No significant difference in the FZ microstructures is observed in the as-welded and annealed conditions using the optical microscope. The fusion zones in both conditions consist of  $\alpha'$  martensite (Figure 7.3a, b, c, & d). However, the FZ

microstructure of the STAed condition mainly consists of  $\alpha$  platelets with interlamellar  $\beta$ -phase (Figure 7.3e & f).



**Figure 7.3- FZ microstructure at as-welded, annealed and STAed conditions for the two thicknesses**



**Figure 7.4- Middle HAZ microstructures in as-welded, annealed and STAed conditions for the two thicknesses**

The effect of post-weld heat treatment on HAZ microstructures is shown in Figure 7.4. It is observed that the HAZ microstructure is a mixture of BM and FZ structures. For the as-welded and annealed samples, the HAZ consists of primary  $\alpha$ ,  $\beta$  and martensitic  $\alpha'$ .

The amount of  $\alpha'$  decreases from the near HAZ to the far HAZ. The HAZ structure in the STAed condition is a mixture of both equiaxed and platelet-like  $\alpha$  and interlamellar  $\beta$ .

## 7.2 Micro-Indentation Hardness

Figure 7.5 shows three different hardness profiles for three post-weld heat treatment conditions of the two thicknesses. The annealed samples are observed to have similar hardness profiles to those in as-welded conditions. The change in microstructures in the STAed process has a significant influence on the hardness profile of the joint. The coarse interlamellar  $\alpha$ - $\beta$  structure has lower hardness value than  $\alpha'$  martensite and is very close to that of equiaxed  $\alpha$ - $\beta$  structure of the base metal. Therefore, the hardness profiles for the STAed conditions is almost constant throughout the joint.

Figure 7.6 shows the variations in average hardness for the three conditions. There is no significant change in BM and HAZ hardnesses for the as-welded and the annealed conditions but the FZ hardness in the annealed condition is slightly higher than that in the as-welded condition. Baeslack and Banas [89] and Thomas *et al.* [66] have explained the reason for this. Annealing heat treatment ages the FZ and the near HAZ martensite by the micro-precipitation of  $\alpha$ -phase from the small amount of the retained  $\beta$  in the FZ. These precipitates reduce the concentration of  $\beta$ -stabilizer in the supersaturated martensite until it approaches to the equilibrium  $\alpha$ . The  $\beta$ -phase is comparatively soft and ductile [83]. As the amount of the soft  $\beta$ -phase decreases in the annealed condition, the hardnesses of the FZ and the near HAZ increase. The FZ hardness is reduced after the STAed, slightly higher than that in the BM. Therefore, the hardness profile of the STAed condition is

almost constant over the entire joint area. The reason for this drop in FZ hardness is due to the change of the FZ microstructure after STAing.

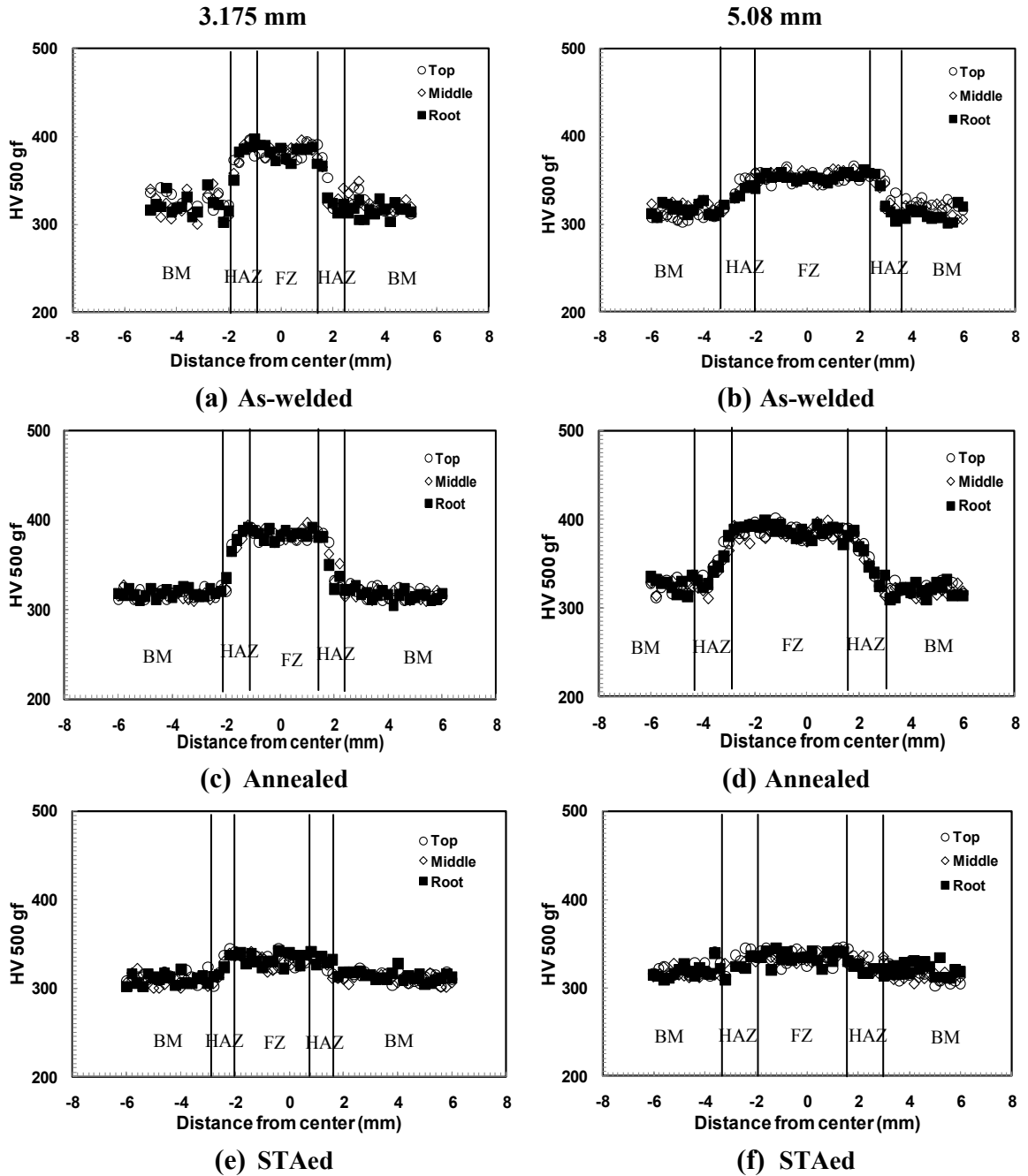
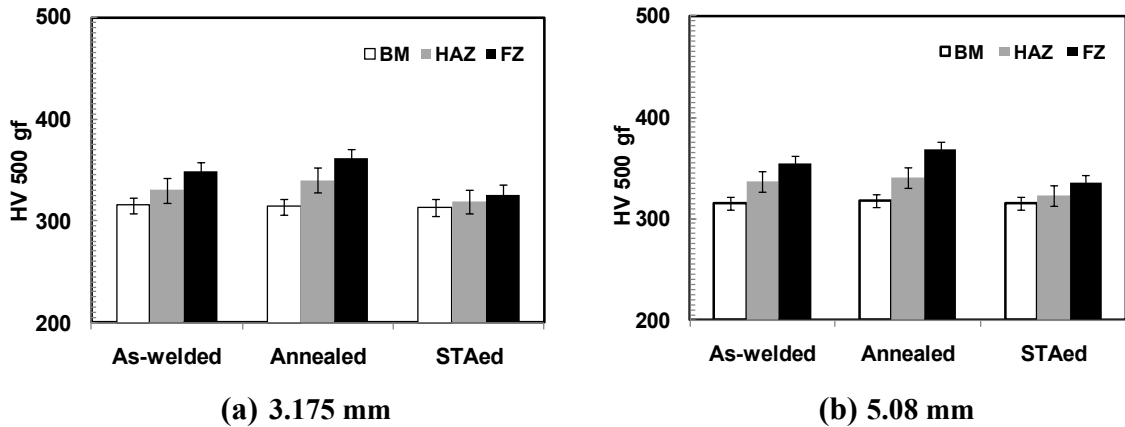


Figure 7.5- Three different hardness distributions for three post-weld conditions for the two thicknesses



**Figure 7.6- Average hardness of three different zones in three post-weld conditions for (a) 3.175 mm and (b) 5.08 mm thick samples**

### 7.3 Global Tensile Properties

Three tensile samples have been prepared for each joint except four for the STAed condition of 5.08 mm thick. Two of them are tested by DIC technique and the remaining by conventional MTS machine. The fusion zone of the as-welded and the annealed samples for both thicknesses remain stronger than BM, resulting in failure in the BM. However, the STAed samples mainly fracture in the fusion zone due to the presence of porosity as well as coarse interlamellar  $\alpha$ - $\beta$  structure for 3.175 mm thick samples. Crack initiates from the underfill and propagates through the FZ due to the presence of porosity for the thinner samples. Heating the samples at a temperature as high as 913°C may expand or accumulate the porosities of the FZ. The STAed samples of the 5.08 mm thickness failed in the heat affected zone due to the presence of the maximum underfill depth and area as well as the presence of weak interlamellar  $\alpha$ - $\beta$  structure in the HAZ.

**Table 7.2: Failure locations and average joint efficiency of all the samples of this part of study**

Thickness (mm)	PWHT	Failure locations (3-4 samples)	Joint efficiency (%)
3.175	As-welded	3 BM	100.5
	Annealed	3 BM	99.62
	STAed	3 FZ	95.38
5.08	As-welded	3 BM	100.4
	Annealed	3 BM	99.62
	STAed	4 HAZ	94.53

Global tensile properties (YS, UTS and El%) are similar for the as-welded and annealed samples for both thicknesses (Figure 7.7). However, a reduction in yield stress and ultimate tensile stress is observed for the STAed samples due to the transformation of the stronger  $\alpha'$  martensite to the relatively weak interlamellar  $\alpha$ - $\beta$  structure. Lower yield stress and ultimate tensile stress in the STAed condition of Ti-6Al-4V have been reported by Short [10] for gas tungsten arc welding. Elongation at fracture (%) also decreases for the STAed condition compared with the other two conditions. This is due to the weaker FZ, the strain localization starts in the underfill area rather than in the more ductile BM. Elastic modulus is almost constant for all the three conditions. The average joint efficiency is maximum for the as-welded condition and minimum for the STAed condition. The annealed condition has almost the same joint efficiency as the as-welded condition.

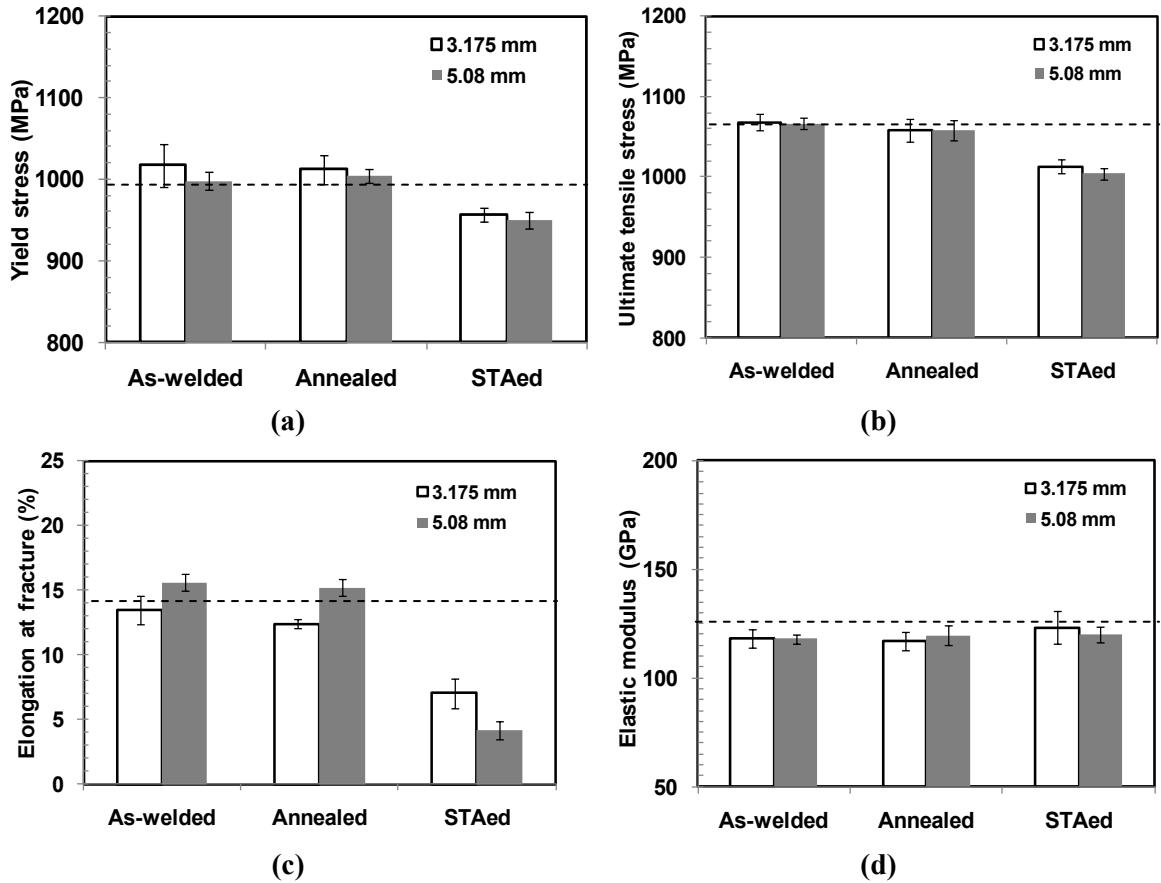


**Figure 7.7- Global tensile properties for three PWHT conditions of the two thicknesses**

## 7.4 Local Tensile Properties

Figure 7.8 shows the digital images of the last moment just before the failure. For both thicknesses the as-welded and the annealed samples show the maximum localized strains in BMs where fracture took place. For the STAed condition of the 3.175 mm thick sample the maximum localized strain is in the underfill region but the fracture is in the FZ, indicating that the fracture initiates from the underfill defect and propagates through the FZ where a cluster of porosities have made the FZ weaker and easier path for the crack to propagate. Whereas, the STAed condition of 5.08 mm thick samples show that

the maximum strain localization is located at the underfill region where the crack initiates and then it propagates through the HAZ.

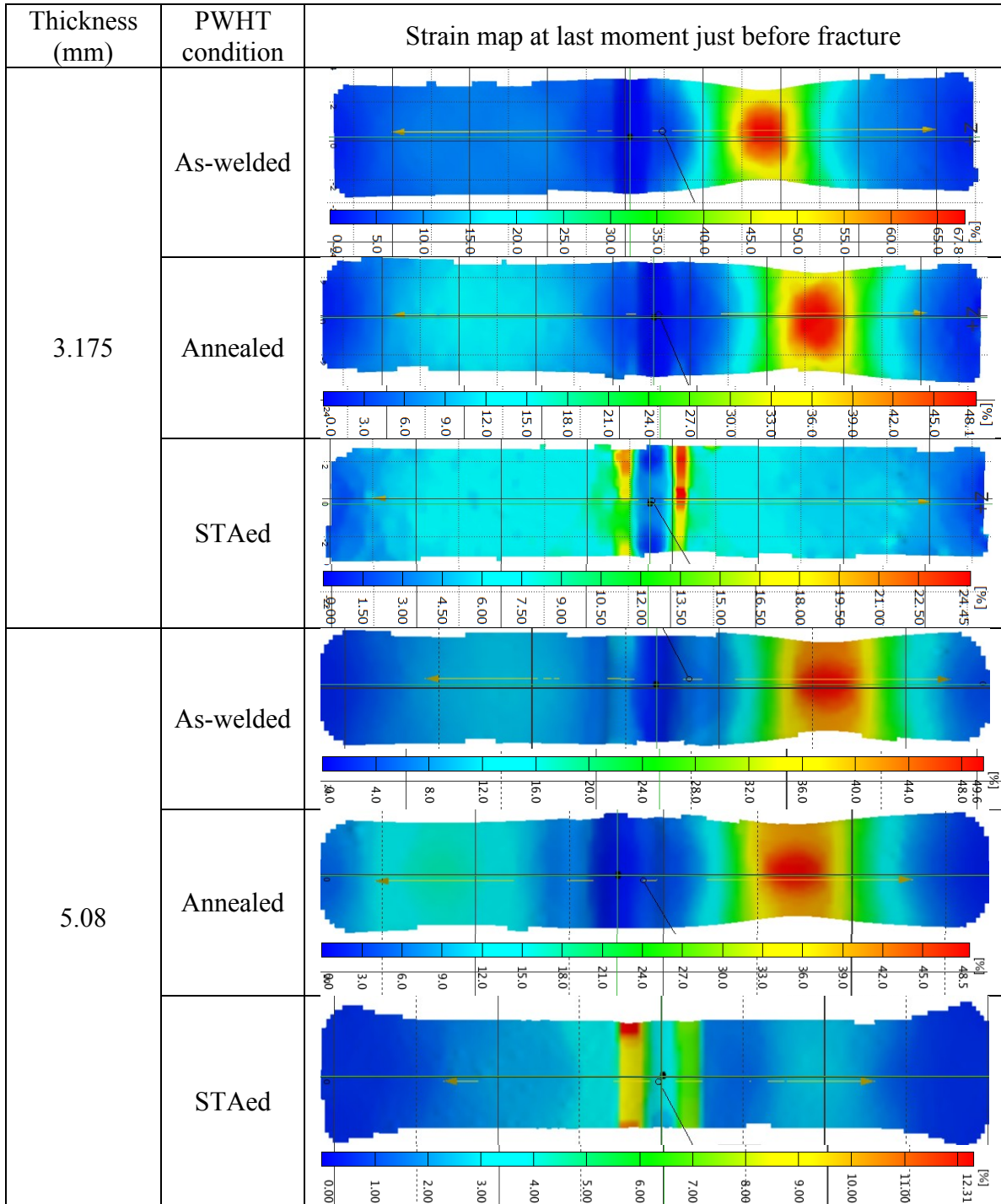


Figure 7.8: Digital images of the last stages before fracture of different PWHT for two thicknesses

Figures 7.9 to 7.11 show the local tensile properties of the three post-weld heat treatment conditions for the two thicknesses. All the three PWHT conditions show the same trend in case of elastic modulus for the two thicknesses (Figure 7.9). This indicates that the residual stress has little influence on the measurement of local properties considering an iso-stress condition. The as-welded and annealed conditions show the same trends in yield stress. The yield stresses of the fusion zones are almost similar to the base metal in the STAed conditions for the two thicknesses (Figure 7.10e & f). The yield stress of the heat affected zone in the STAed conditions drop down more than the other two conditions. These may be associated with the change in the FZ and HAZ microstructures after STAed. All the as-welded and annealed samples failed in the BM resulting in the maximum localized plastic strains at fracture in the BM (Figure 7.11a, b, c, & d). The localized plastic strains at fracture for the STAed samples show the maximum at the underfill regions where the crack is initiated (Figure 7.11e& f).

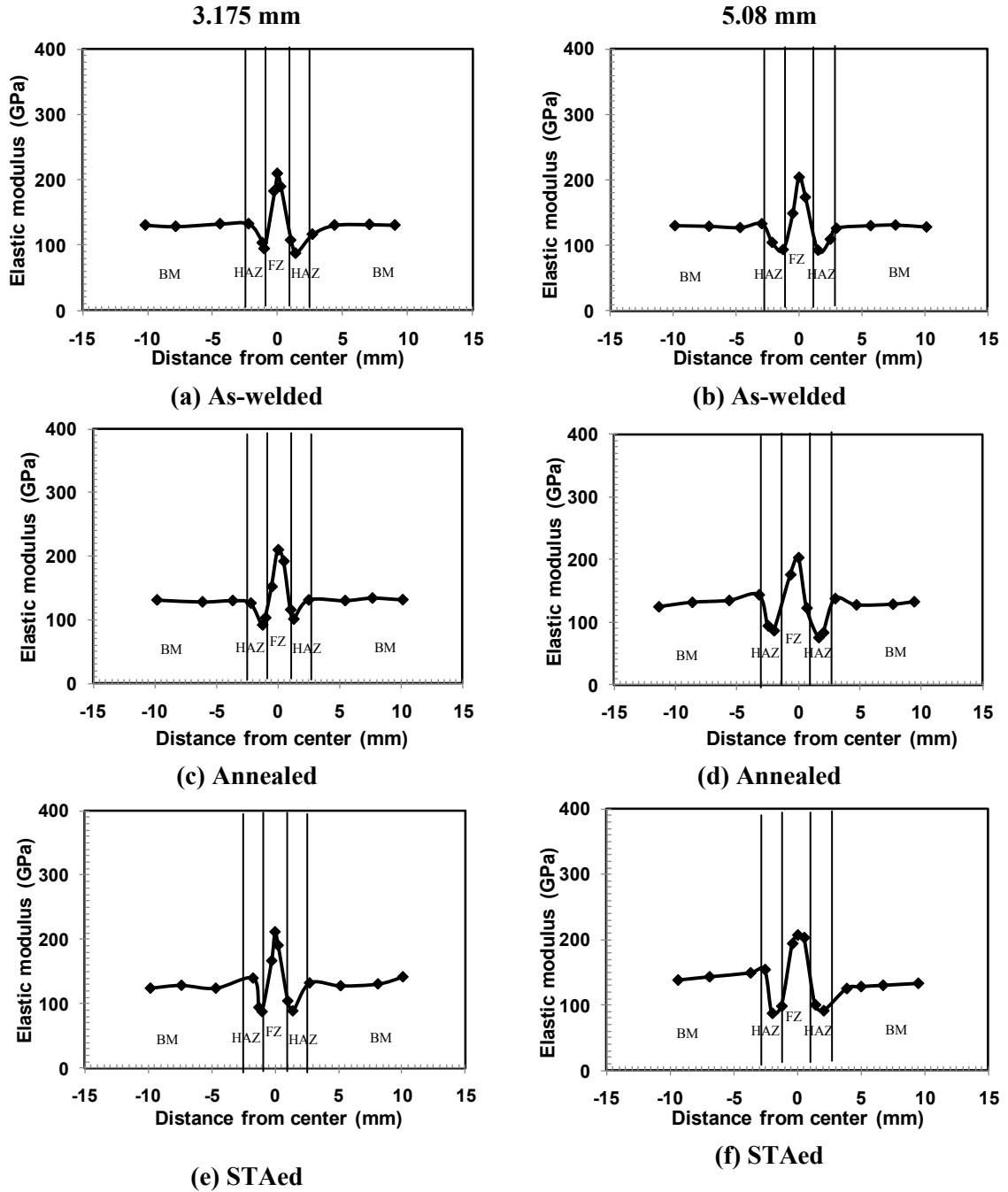


Figure 7.9- Local elastic modulus of 3 PWHT conditions for the two thicknesses

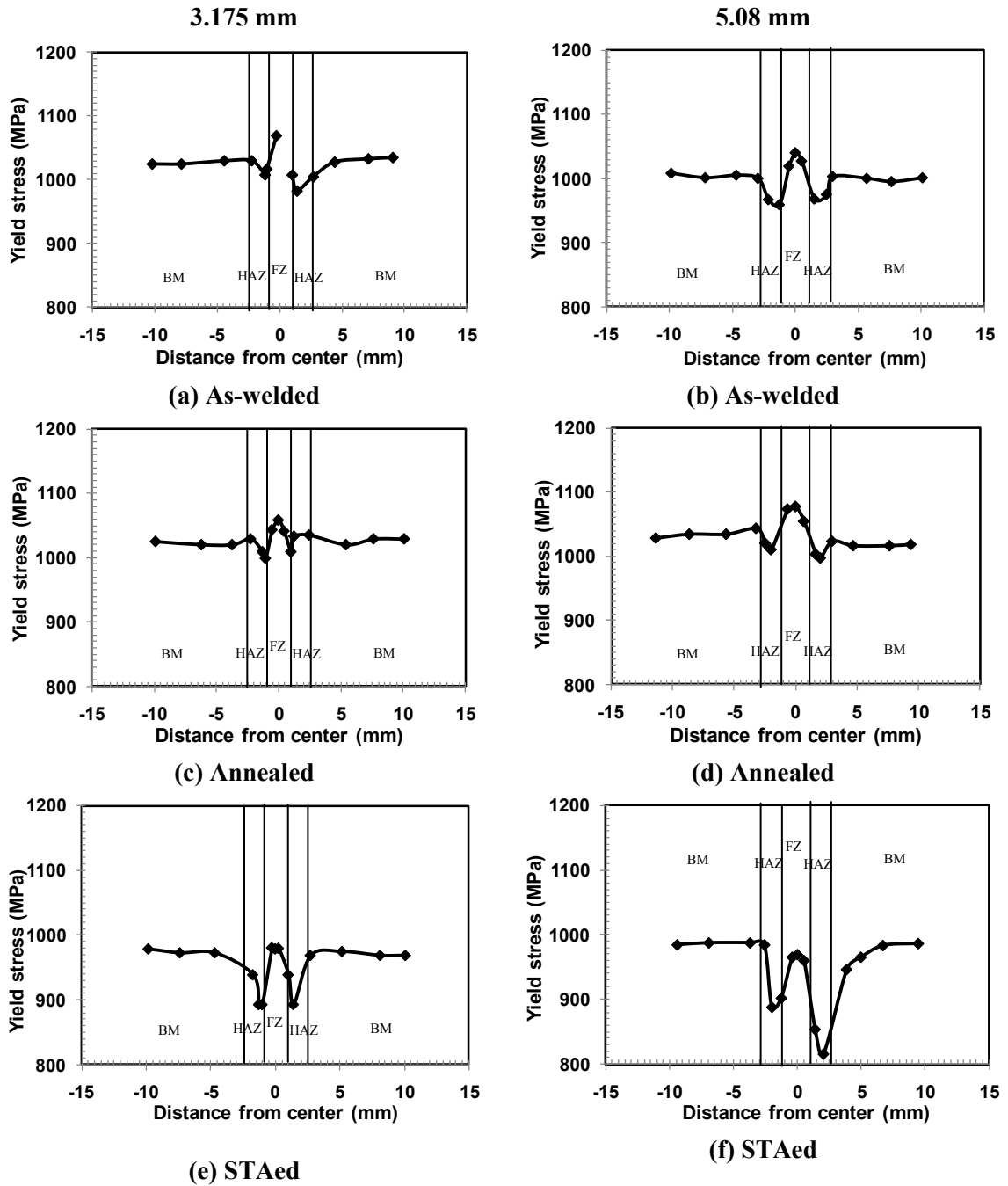
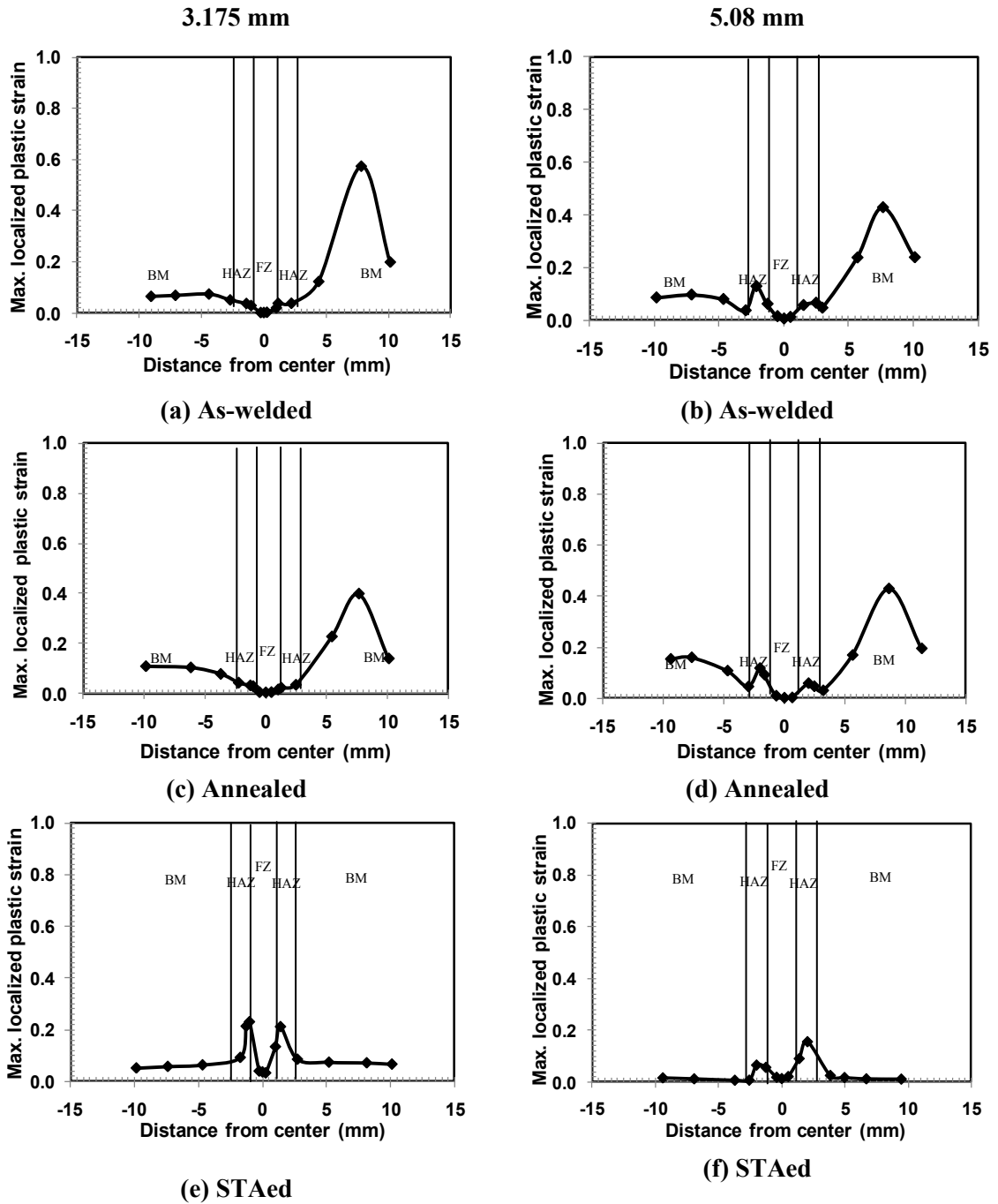


Figure 7.10- Local yield stress of 3 PWHT conditions for the two thicknesses



**Figure 7.11- Localized plastic strain at fracture of 3 PWHT conditions for the two thicknesses**

Figure 7.12 shows the local tensile properties of the individual zones for the three PWHT conditions and for the two thicknesses. Elastic modulus remains almost constant for different zones for all the three conditions. Yield stresses of the annealed fusion zones

show slight increase from the as-welded conditions. This may be associated with the increase in FZ hardness after annealing.

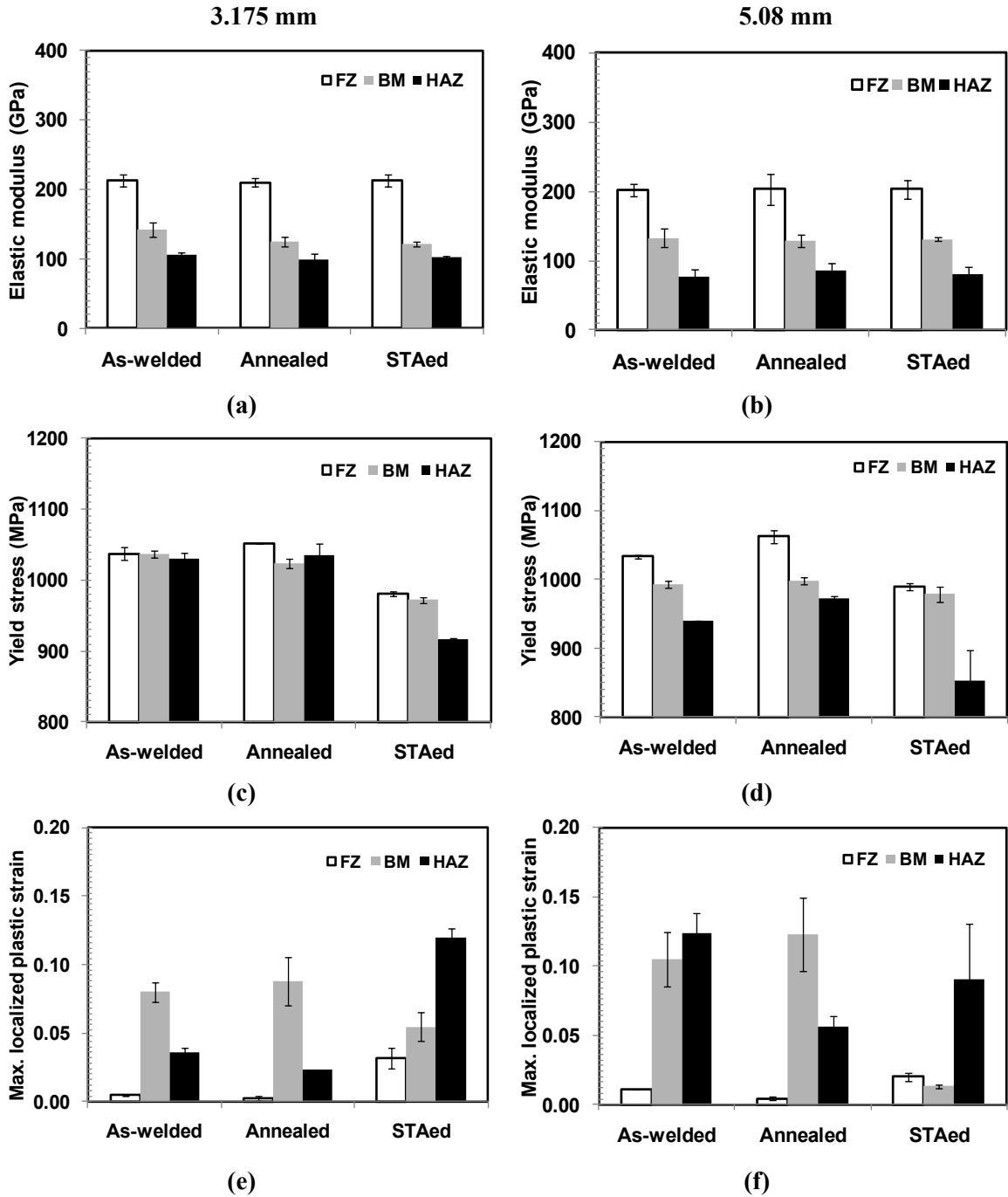
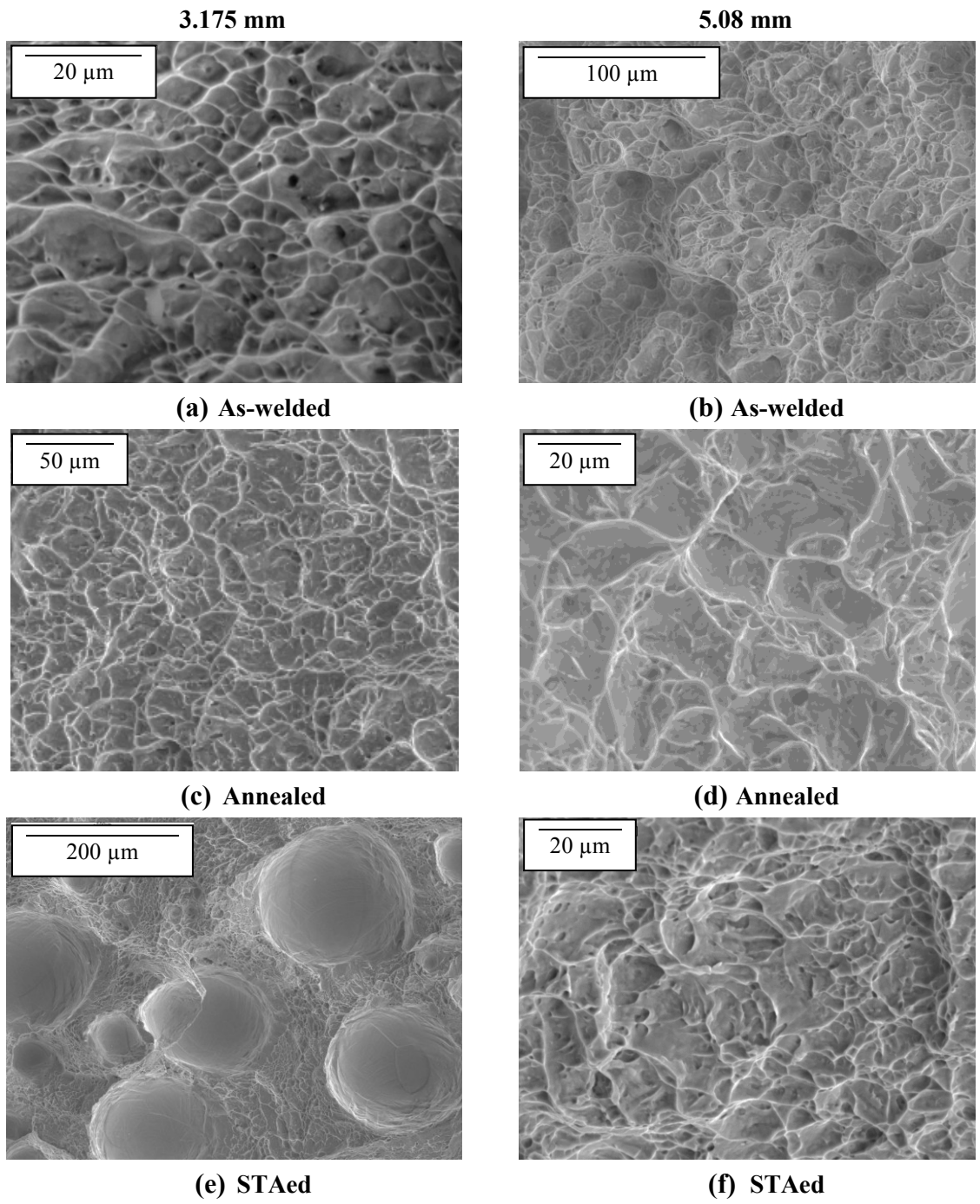


Figure 7.12- Local tensile properties for the two thicknesses

The yield stress of the HAZ also shows slight increase for the annealed conditions due to the same reason as stated for the FZ. The yield stress of the STAed conditions has the minimum in all the three different zones due to the change of microstructures. The localized plastic strains at fracture of the FZs are the maximum for the STAed conditions. This is due to the more ductile microstructure than martensite. Also the localized plastic strains at fracture of the FZs for the annealed condition show the minimum values due to the less amount of soft  $\beta$ -phase than in the as-welded conditions.

## **7.5 Fractography**

The SEM fractographic analysis reveals ductile dimple structures for all the conditions as shown in Figure 7.13. The STAed sample of 3.175 mm thickness shows the presence of porosities in the FZ (Figure 7.13e).



**Figure 7.13- SEM fracture surfaces of the two thicknesses**

## **Chapter 8/ Summary and Concluding Remarks**

---

The laser weldability of Ti-6Al-4V alloy has been studied for 3.175- and 5.08-mm thick sheets in butt joint configuration using a 4 kW continuous wave Nd:YAG laser. The main processing parameters investigated include welding speed, laser power, defocusing distance, joint gap and post-weld heat treatment. The study was carried out through analyzing the weld geometry, microstructure, defects, and mechanical properties.

### **8.1 Effect of Laser Power and Welding Speed on the Weldability of 3.175 mm Sheets**

The sheets have been welded autogenously using the following process parameters: laser power (2 - 4 kW), welding speed (0.75 - 7.5 m/min), heat input (32 – 160 J/mm), and defocusing -1 mm.

- Full penetrations can be obtained at either low laser power and low welding speed, or high laser power and high welding speed.
- Fusion zone and heat affected zone areas decrease with increasing welding speed.
- Underfill and porosity are the two main defects and no solidification cracks are seen in any joints.
- Porosity area decreases with increasing welding speed.

- Compared with the base metal, higher hardness in the fusion zone is due to the formation of  $\alpha'$  martensite. The hardness in the HAZ gradually decreases from the near HAZ to the far HAZ due to the decreased amount of  $\alpha'$  martensite.
- No significant influence of welding speed on global tensile properties is observed.
- Fusion zone shows the maximum elastic modulus and yield stress while the lowest values are obtained for the HAZ. All the samples failed in the base metal, at a position with the maximum strain localization. All the fracture surfaces show ductile dimple structure.

## **8.2 Effect of Welding Speed and Defocusing Distance on the Weldability of 5.08 mm Sheets**

The sheets have been welded autogenously using the following process parameters: laser power 4 kW, welding speed 0.75 – 2.0 m/min, and defocusing distances -1 and -2 mm.

- The two defocusing distances studied in this study have little influence on the geometry, reinforcement, defects and mechanical properties.
- Underfill area increases with increasing welding speed up to a certain limit and then decreases when the narrow root and lack of penetration defects appear.
- Porosity decreases with increasing welding speed but the sample with lack of penetration defect shows high amount of porosity.

- Porosity is the main reason for the failures in the fusion zone, mostly at the low welding speed. Failures in the HAZ are reasoned by the high underfill depth at intermediate speed.

### **8.3 Effect of Joint Gap on the Weldability of 3.175 and 5.08 mm Sheets**

The 3.175-mm thick sheets have been welded using the following process parameters: laser power 3 kW, welding speed 1.69 m/min, defocusing distances -1 mm, and joint gap 0.1 - 0.6 mm. For 5.08 mm thickness the process parameters are: laser power 4 kW, welding speed 1.0 m/min, defocusing distances -1 mm, and joint gap 0.1 - 0.6 mm.

- Full penetrations are obtained up to a joint gap of 0.6 mm for both thicknesses.
- Fusion zone and HAZ areas tend to decrease slightly with increasing joint gaps.
- Joint gap has little influence on the fusion zone and HAZ microstructures.
- The main defects are porosity and underfill and no welding cracks are seen.
- The use of filler wire can reduce the underfill defect.
- A slight decrease in the fusion zone average hardness has been observed with the increase in joint gap.
- The global tensile properties have no significant variations with joint gap.
- Fusion zone remains relatively stronger than base metal even with joint gap up to 0.6 mm for 3.175 mm thick joints.

## **8.4 Effect of Post-Weld Heat Treatment on the Weldability of 3.175 and 5.08 mm sheets**

Two post-weld heat treatment conditions have been investigated for both thicknesses; stress relief annealing and full heat treatment (STAing). The samples are then compared with the as-welded condition. The samples have been welded at a joint gap of 0.3 mm for both thicknesses.

- The fusion zone structure is transformed to platelet  $\alpha$  with interlamellar  $\beta$  structure in the STAed condition compared with acicular  $\alpha'$  martensite in the as-welded and the annealed conditions.
- Post-weld annealing treatment slightly increases the fusion zone and near HAZ hardnesses. The STAing treatment leads to lower hardness values in the HAZ and fusion zone than the as-welded and annealed conditions.
- Localized plastic strain at fracture in the annealed condition is lower in the fusion zone than that in the as-welded condition but the highest localized plastic strain at fracture is obtained in the STAed condition.
- Fusion zone yield stresses are found to be maximum in the annealed condition and minimum in the STAed condition.

## **8.5 Recommendations for Future Work**

- The thicker samples are needed to be further investigated using higher laser power, or using fiber laser and laser-arc hybrid welding processes.
- It is recommended to conduct the tensile test by machining the samples in to a flat surface.
- More variations in defocusing distances need to be studied to understand properly the effect of defocusing distance.
- It is necessary to study more mechanical properties such as fatigue, impact and creep.
- Further improvement is required to accurately determine the local tensile properties of the fusion zone and the HAZ.

## References

- 1 Lutjering, G. and Williams, J.C. *Titanium*. (Springer, 2007).
- 2 Leyens, C. and Peters, M., eds. *Titanium and Titanium Alloys. Fundamentals and Applications*. (WILEY-VCH Verlag GmbH & Co., Weinheim, 2003).
- 3 Akman, E., Demir, A., Canel, T. and Sinmazçelik, T. Laser welding of Ti6Al4V titanium alloys. *Journal of Materials Processing Technology*, 2009, 209(8), pp. 3705-3713.
- 4 Tsay, L., Shan, Y.P., Chao, Y.H. and Shu, W. The influence of porosity on the fatigue crack growth behavior of Ti-6Al-4V laser welds. *Journal of Materials Science*, 2006, 41(22), pp. 7498-7505.
- 5 Karimzadeh, F., Salehi, M., Saatchi, A. and Meratian, M. Effect of microplasma arc welding process parameters on grain growth and porosity distribution of thin sheet Ti6Al4V alloy weldment. *Materials and Manufacturing Processes*, 2005, 20(2), pp. 205 - 219.
- 6 Costa, A., Miranda, R., Quintino, L. and Yapp, D. Analysis of beam material interaction in welding of titanium with fiber lasers. *Materials and Manufacturing Processes*, 2007, 22(7), pp. 798-803.
- 7 Boyer, R. An overview on the use of titanium in the aerospace industry. *Materials science & engineering A*, 1996, 213(1-2), pp. 103-114.
- 8 Moiseyev, V.N. *Titanium Alloys: Russian Aircraft and Aerospace Applications*. (Taylor & Francis Group, NW, 2006).
- 9 Polmear, I.J. *Light Alloys: From Traditional Alloys to Nanocrystals*. (Elsevier 2006 ).
- 10 Short, A.B. Gas tungsten arc welding of  $\alpha+\beta$  titanium alloys: a review. *Materials Science and Technology*, 2009, 25(3), pp. 309-324.
- 11 Yunlian, Q., Ju, D., Quan, H. and Liying, Z. Electron beam welding, laser beam welding and gas tungsten arc welding of titanium sheet. *Materials Science and Engineering A*, 2000, 280(1), pp. 177-181.
- 12 Caiazzo, F., Curcio, F., Daurelio, G. and Memola Capece Minutolo, F. Ti-6Al-4V sheets lap and butt joints carried out by CO<sub>2</sub> laser: mechanical and morphological characterization. *Journal of Materials Processing Technology*, 2004, 149(1-3), pp. 546-552.
- 13 Kazzaz, A.H., Medraj, M., Cao, X., Jahazi, M. and Xiao, M. Effect of welding speed on Nd:YAG laser weldability of ZE41A-T5 magnesium sand casting. In Martin, J.P.,

- ed. *44th Annual Conference of Metallurgist of CIM*, pp. 137-149, (Calgary, AL, 2005).
- 14 Wanjara, P., Brochu, M. and Jahazi, M. Thin gauge titanium manufacturing using multiple-pass electron beam welding. *Materials and Manufacturing Processes*, 2006, 21 (5-6), pp. 439-451.
  - 15 Donachie, M.J. *Titanium: A Technical Guide*. (ASM International, Materials Park, OH, 1989).
  - 16 Joshi, V.A. *Titanium Alloys: An Atlas of Structures and Fracture Features*. (Taylor & Francis, NY, 2006).
  - 17 Barreda, J.L., Santamaría, F., Azpiroz, X., Irisarri, A.M. and Varona, J.M. Electron beam welded high thickness Ti6Al4V plates using filler metal of similar and different composition to the base plate. *Vacuum*, 2001, 62(2-3), pp. 143-150.
  - 18 Eylon, D., Postans, P.J., Fujishiro, S. and Froes, F.H. High-temperature titanium alloys - a review. *Journal of Metals*, 1984, 36(11), pp. 55-62.
  - 19 Wanjara, P., Brochu, M. and Jahazi, M. Ti-6Al-4V electron beam weld qualification using laser scanning confocal microscopy. *Materials Characterization*, 2005, 54(3), pp. 254-262.
  - 20 Ahmed, T. and Rack, H.J. Phase transformations during cooling in  $\alpha + \beta$  titanium alloys. *Materials Science & Engineering A*, 1998, 243 (1-2), pp. 206-211.
  - 21 Karimzadeh, F., Heidarbeigy, M. and Saatchi, A. Effect of heat treatment on corrosion behavior of Ti-6Al-4V alloy weldments. *Journal of Materials Processing Technology*, 2008, 206(1-3), pp. 388-394.
  - 22 Majumdar, J. and Manna, I. Laser processing of materials. *Sadhana*, 2003, 28(3 & 4), pp. 495-562.
  - 23 Hitz, B., Ewing, J.J. and Hecht, J. *Introduction to Laser Technology*. (The Institute of Electrical and Electronics Engineers, Inc, NY, 1991).
  - 24 Steen, W.M. *Laser Materials Processing*. (Springer-Verlag London Limited, London, 2003).
  - 25 Cao, X., Wallace, W., Poon, C. and Immarigeon, J.P. Research and progress in laser welding of wrought aluminum alloys I. laser welding processes. *Materials Manufacturing Process*, 2003, 18(1), pp. 1-22.

- 26 Casalino, G., Curcio, F. and Memola Capece Minutolo, F. Investigation on Ti-6Al-4V laser welding using statistical and Taguchi approaches. *Journal of Materials Processing Technology*, 2005, 167(2-3), pp. 422-428.
- 27 Ahmed, N., ed. *New Developments in Advanced Welding* (Woodhead Publishing Limited, Cambridge, UK, 2005).
- 28 Sun, Z. and Ion, J. Laser welding of dissimilar metal combinations. *Journal of Materials Science*, 1995, 30(17), pp. 4205-4214.
- 29 Lee, J.Y., Ko, S.H., Farson, D.F. and Yoo, C.D. Mechanism of keyhole formation and stability in stationary laser welding. *Journal of Physics D: Applied Physics*, 2002, 35(13), pp. 1570-1576.
- 30 Perret, O., Bizouard, M., Naudy, P., Pascal, G., Nore, D., Horde, Y. and Delaisse, Y. Characterization of the keyhole formed during pulsed Nd:YAG laser interaction with a Ti-6Al-4V metallic target. *Journal of Applied Physics*, 2001, 90(1), pp. 27-30.
- 31 Rai, R., Elmer, J.W., Palmer, T.A. and DebRoy, T. Heat transfer and fluid flow during keyhole mode laser welding of tantalum, Ti-6Al-4V, 304L stainless steel and vanadium. *Journal of Physics D: Applied Physics*, 2007, 40(18), pp. 5753-5766.
- 32 Ion, J.C. *Laser Processing of Engineering Materials; Principles, Procedure and Industrial Application*. (Elsevier Butterworth-Heinemann, 2005).
- 33 Aalderink, B.J., Lange, D.F.de, Aarts, R.G.K.M. and Meijer, J. Keyhole shapes during laser welding of thin metal sheets. *Journal of Physics D: Applied Physics*, 2007, 40(17), pp. 5388-5393.
- 34 Duley, W.W. *Laser Welding*. (Wiley-Interscience, NJ, 1998).
- 35 Mackwood, A.P. and Crafer, R.C. Thermal modelling of laser welding and related processes: a literature review. *Optics & Laser Technology*, 2005, 37(2), pp. 99-115.
- 36 Cieslak, M.J. Phase transformations in weldments: new materials and new perspectives. *3rd Int. Conf. on Trends in Welding Research*, pp. 229-241, (Gatlingburg, TN, 1992).
- 37 Handbook, A. *Welding, Brazing, and Soldering*. (ASM International, Materials Park, OH, 1993).
- 38 Mazumder, J. and Steen, W.M. Welding of Ti 6Al-4V by a continuous wave CO<sub>2</sub> laser. *Metal Construction*, 1980, 12(9), pp. 423-427.

- 39 Tsay, L.W. and Tsay, C.Y. The effect of microstructures on the fatigue crack growth in Ti-6Al-4V laser welds. *International Journal of Fatigue*, 1997, 19(10), pp. 713-720.
- 40 Zheng, S. Electron beam welding: process and industrial applications. *International Journal of Materials and Product Technology*, 1995, 10(3-4), pp. 208-221.
- 41 Balyts'kyi, O.I. and Mascalzi, G. Selection of materials for high-speed motor rotors. *Materials Science*, 2002, 38(2), pp.293-303.
- 42 Cao, X., Jahazi, M., Immarigeon, J.P. and Wallace, W. A review of laser welding techniques for magnesium alloys. *Journal of Materials Processing Technology*, 2006, 171(2), pp. 188-204.
- 43 Dawes, C. *Laser Welding*. (McGraw-Hill, Inc, NY, 1992).
- 44 Kim, T.H. Porosity formation in laser-beam materials processing. *Journal of Materials Science Letters*, 1991, 10(7), pp. 400-402.
- 45 Chung, B.G., Rhee, S. and Lee, C.H. The effect of shielding gas types on CO<sub>2</sub> laser tailored blank weldability of low carbon automotive galvanized steel. *Materials Science and Engineering A*, 1999, 272(2), pp. 357-362.
- 46 Tani, G., Ascari, A., Campana, G. and Fortunato, A. A study on shielding gas contamination in laser welding of non-ferrous alloys. *Applied Surface Science*, 2007, 254(4), pp. 904-907.
- 47 Cao, X. and Jahazi, M. Effect of welding speed on butt joint quality of Ti-6Al-4V alloy welded using a high-power Nd:YAG laser. *Optics and Lasers in Engineering*, 2009, 47(11), 1231-1241.
- 48 Cao, X., Debaecker, G., Poirier, E., Marya, S., Cuddy, J., Birur, A and P., W. Effect of Joint Gap on Nd: YAG Laser Welded Ti-6Al-4V. *ICALEO* (Laser Institute of America, 2009).
- 49 Mazumder, J. and Steen, W. Microstructure and mechanical properties of laser welded titanium 6Al-4V. *Metallurgical and Materials Transactions A*, 1982, 13(5), pp. 865-871.
- 50 Abderrazak, K., Ben Salem, W., Mhiri, H., Bournot, P. and Autric, M. Nd:YAG Laser welding of AZ91 magnesium alloy for aerospace industries. *Metallurgical and Materials Transactions B*, 2009, 40(1), pp. 54-61.
- 51 Dilthey, U., Fuest, D. and Scheller, W. Laser welding with filler wire. *Optical and Quantum Electronics*, 1995, 27(12), pp. 1181-1191.

- 52 Pastor, M., Zhao, H., Martukanitz, R.P. and Debroy, T. Porosity, underfill and magnesium loss during continuous wave Nd:YAG laser welding of thin plates of aluminum alloys 5182 and 5754. *Welding Journal*, 1999, 78(6), pp. 207s-216s.
- 53 Wang, S.H., Wei, M.D. and Tsay, L.W. Tensile properties of LBW welds in Ti-6Al-4V alloy at evaluated temperatures below 450°C. *Materials Letters*, 2003, 57(12), pp. 1815-1823.
- 54 Weston, J., Jones, A. and Wallach, R. Laser welding of aluminium alloys using different laser sources. *6th international conference on welding and melting by electron and laser beams*, p. 187, (Toulon, France, 1998).
- 55 Deyev, G. and Deyev, D. *Surface Phenomena in Fusion Welding Processes*. (Taylor & Francis, NW, 2006).
- 56 Khaled, Z. An investigation of pore cracking in titanium welds. *Journal of Materials Engineering and Performance*, 1994, 3(3), pp. 419-434.
- 57 Mohandas, T., Banerjee, D. and Kutumba Rao, V. Fusion zone microstructure and porosity in electron beam welds of an  $\alpha+\beta$  titanium alloy. *Metallurgical and Materials Transactions A*, 1999, 30(13), pp. 789-798.
- 58 Matsunawa, A., Kim, J. D., Seto, N., Mizutani, M. and Katayama, S. Dynamics of keyhole and molten pool in laser welding. *Journal of Laser Applications*, 1998, 10(6), pp. 247-254.
- 59 Pastor, M., Zhao, H. and Debroy, T. Pore Formation during continuous wave Nd:YAG laser welding of aluminum for automotive applications. *Revista de Metalurgia*, 2000, 36(2), pp. 108-117.
- 60 Cao, X., Wallace, W., Poon, C. and Immarigeon, J.P. Research in laser welding of wrought aluminum alloys. II. metallurgical microstructures, defects, and mechanical properties. *Materials and Manufacturing Processes*, 2003, 18(1), pp. 23-49.
- 61 Hunziker, O., Dye, D. and Reed, R.C. On the formation of a centreline grain boundary during fusion welding. *Acta Materialia*, 2000, 48(17), pp. 4191-4201.
- 62 Andrews, J.G., Atthey, D.R. and Byatt-Smith, J.G. Weld-pool sag. *Journal of Fluid Mechanics Digital Archive*, 1980, 100(04), pp. 785-800.
- 63 Hoobasar Rampaul *Pipe Welding Procedures*. (Industrial Press, NY, 2002).
- 64 Zhu, Z., Wu, W. and Chen, Q. Numerical simulation of molten droplet shape and electromagnetic pinch effect in short-circuit CO<sub>2</sub> welding. *Robotic Welding, Intelligence and Automation*, 2007, 362, pp. 135-144.

- 65 Baeslack, W.A. Observations of solidification cracking in titanium alloy weldments *Metallography*, 1980, 13(3), pp. 277-281.
- 66 Thomas, G., Ramachandra, V., Nair, M.J., Nagarajan, K.V. and Vasudevan, R. Effect of preweld and postweld heat treatment on the properties of GTA welds in Ti-6Al-4V sheet. *Welding Journal*, 1992, 71(1), pp. 15s-20s
- 67 Baeslack, W.A.I., Becker, D.W. and Froes, F.H. Advances in titanium alloy welding metallurgy. *Journal of Metals*, 1984, 36(5), pp. 46-58.
- 68 Thomas, G., Ramachandra, V., Ganeshan, R. and Vasudevan, R. Effect of pre- and post-weld heat treatments on the mechanical properties of electron beam welded Ti-6Al-4V alloy. *Journal of Materials Science*, 1993, 28(18), pp. 4892-4899.
- 69 Sun, Z., Pan, D. and Zhang, W. Correlation between Welding Parameters and Microstructures in TIG, Plasma, and Laser Welded Ti-6Al-4V. *6th Int. Conf, Trends in Welding Research*, pp. 760-767, (Pine Mountain, Georgia, USA, 2002).
- 70 Lockwood, W.D. and Reynolds, A.P. Simulation of the global response of a friction stir weld using local constitutive behavior. *Materials Science and Engineering A*, 2003, 339(1-2), pp. 35-42.
- 71 Lockwood, W.D., Tomaz, B. and Reynolds, A.P. Mechanical response of friction stir welded AA2024: experiment and modeling. *Materials Science and Engineering A*, 2002, 323(1-2), pp. 348-353.
- 72 Boyce, B., Reu, P. and Robino, C. The constitutive behavior of laser welds in 304L stainless steel determined by digital image correlation. *Metallurgical and Materials Transactions A*, 2006, 37(8), pp. 2481-2492.
- 73 Peters, W.H. and Ranson, W.F. Digital imaging techniques in experimental stress analysis *Optical Engineering*, 1982, 21(3), pp. 427-432.
- 74 Sutton, M.A., Wolters, W.J., Peters, W.H., Ranson, W.F. and McNeill, S.R. Determination of displacements using an improved digital correlation method. *Image and Vision Computing*, 1983, 1(3), pp. 133-139.
- 75 Chu, T., Ranson, W. and Sutton, M. Applications of digital-image-correlation techniques to experimental mechanics. *Experimental Mechanics*, 1985, 25(3), pp. 232-244.
- 76 Bruck, H., McNeill, S., Sutton, M. and Peters, W. Digital image correlation using Newton-Raphson method of partial differential correction. *Experimental Mechanics*, 1989, 29(3), pp. 261-267.

- 77 He, Z., Sutton, M., Ranson, W. and Peters, W. Two-dimensional fluid-velocity measurements by use of digital-speckle correlation techniques. *Experimental Mechanics*, 1984, 24(2), pp. 117-121.
- 78 Chu, T.C., Peters, W.H., Ranson, W.F. and Sutton, M.A. Application of digital image correlation methods to rigid body mechanics. *Proc.1982 Fall Meeting of SESA*, 1982, pp. 73-77.
- 79 Rastogi, P., Sutton, M., McNeill, S., Helm, J. and Chao, Y. Advances in two-dimensional and three-dimensional computer vision. *Photomechanics*, pp. 323-372 (Springer Berlin / Heidelberg, 2000).
- 80 Orteu, J.-J. 3-D computer vision in experimental mechanics. *Optics and Lasers in Engineering*, 2009, 47(3-4), pp. 282-291.
- 81 AWS. Specification for fusion welding for aerospace application. *D17.1* (American Welding Society, Ohio, USA, 2001).
- 82 Rao, K.P. and Janvir, B.K. Mechanical properties of electron beam weld metals of Ti-6Al-4V. *Prakt. Metallogr.*, 1992, 29(3), pp. 132-142.
- 83 Lee, Y., Peters, M. and Welsch, G. Elastic moduli and tensile and physical properties of heat-treated and quenched powder metallurgical Ti-6Al-4V alloy. *Metallurgical and Materials Transactions A*, 1991, 22(3), pp. 709-714.
- 84 Lee, Y.T. and Welsch, G. Young's modulus and damping of Ti-6Al-4V alloy as a function of heat treatment and oxygen concentration. *Materials Science and Engineering: A*, 1990, 128(1), pp. 77-89.
- 85 Fan, Z. On the Young's moduli of Ti-6Al-4V alloys. *Scripta Metallurgica et Materialia*, 29(11), 1993, pp. 1427-1432.
- 86 Boyer, H. E, Collings, E.W and Welsch, G. *Materials Properties Handbook: Titanium Alloys*. (ASM International, OH, 1994).
- 87 Khan, P. and Debroy, T. Alloying element vaporization and weld pool temperature during laser welding of AISI 202 stainless steel. *Metallurgical and Materials Transactions B*, 1984, 15(4), pp. 641-644.
- 88 Wojnowski, D., Oh, Y.K. and Indacochea, J.E. Metallurgical assessment of the softened HAZ region during multipass welding. *Journal of Manufacturing Science and Engineering*, 2000, 122(2), pp. 310-315.
- 89 Baeslack, W.A. and Banas, C.M. A comparative evaluation of laser and gas tungsten arc weldments in high-temperature titanium alloys *Welding Journal, Research Supplement*, 60 (7), 1981, pp. 121s-130s.